IONOSPHERIC MODIFICATION: ITS EFFETS ON RADAR AND SATELLITE COMMUNICATION SYSTEMS

G. F. VanBlaricum, et al

General Research Corporation

Prepared for:

Army Missile Command
Defense Advanced Research Projects Agency

October 1974

ARPA Order Number:	958, Amendment No. 5
Program Code Number:	4E20
Short Title of Work:	STO Supporting Studies: Signal Transmission Data Analysis
Name of Contractor:	General Research Corporation
Amount of Contract:	$36,829 (Task 18)
Contract Number:	DAAH01-73-C-0310
Effective Date of Contract:	31 May 1974
Contract Expiration Date:	31 December 1974
Project Engineer:	A. D. Stathacopoulos
Phone Number:	(805) 964-7724, Ext. 412

In addition to approval by the Project Leader and Department Head, General Research Corporation reports are subject to independent review by a staff member not connected with the project. This report was reviewed by P. J. Redmond.

The views and conclusions contained in this document are those of the authors and should not be interpreted as necessarily representing the official policies, either expressed or implied, of the Defense Advanced Research Projects Agency or the U.S. Government.

This research was supported by the Defense Advanced Research Projects Agency of the Department of Defense and was monitored by the U.S. Army Missile Command under Contract DAAH01-73-C-0310.

Further distribution of this document is limited to U.S. Government agencies. Requests for this document must be referred to Commander, U.S. Army Missile Command, Attn: AMSMI-RNS, Redstone Arsenal, Alabama 35809.

SECURITY CLASSIFICATION OF THIS PAGE (When Data Entered)

REPORT DOCUMENTATION PAGE

READ INSTRUCTIONS BEFORE COMPLETING FORM

1. REPORT NUMBER: RM-1911	2. GOVT ACCESSION NO.
3. RECIPIENT'S CATALOG NUMBER: AD-A008847	
4. TITLE (and Subtitle): Ionospheric Modification: Its Effects on Radar and Satellite Communication Systems	5. TYPE OF REPORT & PERIOD COVERED: Releasable Memorandum, 31 May - 30 September 1974
	6. PERFORMING ORG. REPORT NUMBER: RM-1911
7. AUTHOR(s): G. F. VanBlaricum, H. S. Ostrowsky	8. CONTRACT OR GRANT NUMBER(s): DAAH01-73-C-0310
9. PERFORMING ORGANIZATION NAME AND ADDRESS: General Research Corporation, P.O. Box 3587, Santa Barbara, CA 93105	10. PROGRAM ELEMENT, PROJECT, TASK AREA & WORK UNIT NUMBERS: ARPA Order No. 958, Amendment No. 5
11. CONTROLLING OFFICE NAME AND ADDRESS: Defense Advanced Research Projects Agency, 1400 Wilson Blvd., Arlington, VA 22209	12. REPORT DATE: October 1974
	13. NUMBER OF PAGES: ~~114~~ 112
14. MONITORING AGENCY NAME & ADDRESS (if different from Controlling Office): US Army Missile Command, Redstone Arsenal, Alabama 35809, Attn: AMSMI-RNS	15. SECURITY CLASS. (of this report): UNCLASSIFIED
	15a. DECLASSIFICATION/DOWNGRADING SCHEDULE: -

16. DISTRIBUTION STATEMENT (of this Report)

Further distribution of this document is limited to U.S. Government agencies. Requests for this document must be referred to Commander, U.S. Army Missile Command, Attn: AMSMI-RNS, Redstone Arsenal, Alabama 35809.

17. DISTRIBUTION STATEMENT (of the abstract entered in Block 20, if different from Report)

18. SUPPLEMENTARY NOTES

19. KEY WORDS (Continue on reverse side if necessary and identify by block number)

Scintillation
Ionospheric modification
Radar systems
Satellite communication systems

20. ABSTRACT (Continue on reverse side if necessary and identify by block number)

High-power RF radio transmissions have been used to create significant local disturbances of the temperature and electron density in the F-region of the ionosphere. This artificial modification of the ionosphere can create appreciable levels of amplitude and phase scintillation in radio signals passing through the disturbed region. A number of measurements of such scintillation were conducted by Aeronomy Corporation in an experimental program known as PRAIRIE SMOKE.

(Continued)

DD FORM 1 JAN 73 1473 EDITION OF 1 NOV 65 IS OBSOLETE

(Block 20 continued)

This report describes and reorganizes some of the PRAIRIE SMOKE experimental data and presents a brief overview of scintillation theory. The experimental data were used to develop a model for predicting scintillation effects along any particular line-of-sight through the disturbed region. That model is presented here and predictions made using it are compared to some of the experimental data.

Scintillation can degrade radar detection probability, radar tracking accuracy, and satellite-to-ground communication error rates. These degradation were computed parametrically as functions of the scintillation index. The results presented in this report can be used to determine the degradation produced by natural or nuclear-induced scintillations as well as scintillations produced by RF heating of the ionosphere.

ACKNOWLEDGMENT

The authors thank Dr. S. A. Bowhill, Dr. E. K. Walton, and Mr. D. R. Ward of Aeronomy Corporation for their cooperation in providing the data from Prairie Smoke, for their helpful discussions regarding the experimental program, and for their suggestions of the appropriate form for the scintillation model.

ABSTRACT

High-power RF radio transmissions have been used to create significant local disturbances of the temperature and electron density in the F-region of the ionosphere. This artificial modification of the ionosphere can create appreciable levels of amplitude and phase scintillation in radio signals passing through the disturbed region. A number of measurements of such scintillation were conducted by Aeronomy Corporation in an experimental program known as PRAIRIE SMOKE.

This report describes and reorganizes some of the PRAIRIE SMOKE experimental data and presents a brief overview of scintillation theory. The experimental data were used to develop a model for predicting scintillation effects along any particular line-of-sight through the disturbed region. That model is presented here and predictions made using it are compared to some of the experimental data.

Scintillation can degrade radar detection probability, radar tracking accuracy, and satellite-to-ground communication error rates. These degradations were computed parametrically as functions of the scintillation index. The results presented in this report can be used to determine the degradation produced by natural or nuclear-induced scintillations as well as scintillations produced by RF heating of the ionosphere.

CONTENTS

SECTION		PAGE
	ACKNOWLEDGMENT	i
	ABSTRACT	iii
1	INTRODUCTION AND SUMMARY	1
2	IONOSPHERIC MODIFICATION	5
	2.1 The Natural Ionosphere	5
	2.2 Modifying the Atmosphere	6
	2.3 Experimental Studies of the Modified Ionosphere	6
3	THEORY OF IONOSPHERIC SCINTILLATION	10
	3.1 The Ionosphere as a Phase Screen	10
	3.2 Statistics of the Diffracted Wave	15
	3.3 Phase and Angle Scintillation	19
	3.4 Natural Scintillation	20
4	SATELLITE TRANSMISSION EXPERIMENTS	24
	4.1 Strength of Scintillations	26
	4.2 Irregularity Size, Orientation, and Velocity	28
	4.3 Comparison of Experiments with Theory	29
5	A SCINTILLATION MODEL FOR THE MODIFIED IONOSPHERE	34
	5.1 A Modified Scintillation Formula	34
	5.2 Comparison with Briggs and Parkin Formula	40
	5.3 Parameters for the Model	43
	5.4 Comparison of the Modified Theory with Experiments	46
6	SCINTILLATION EFFECTS ON RADAR SYSTEMS	51
	6.1 The Amplitude Distribution Function	51
	6.2 Radar Detection Probability and Detection Range	57

CONTENTS (Cont.)

SECTION		PAGE
	6.3 Radar Tracking	63
7	SATELLITE COMMUNICATION SYSTEMS	86
APPENDIX	SCINTILLATION INDEXES AND STATISTICAL DISTRIBUTIONS	95
	REFERENCES	101

ILLUSTRATIONS

NO.		PAGE
2.1	Schematic of Ionospheric Modification	7
3.1	Diffraction by a Random Phase Screen	11
3.2	Dimensions of Field-Aligned Striations	13
3.3	Geometry of Ionospheric Slab in Briggs and Parkin Theory	14
3.4	Development of Scintillation with Viewing Distance from Phase Screen	18
3.5	Curves of Constant Scintillation Index S_4 on a Plot of $\lambda z/r_o^2$ vs ϕ_o . The broken lines correspond to the exact solution; the full lines to the approximations.	18
3.6	Average Natural Scintillation at 150 MHz for 40°N Geomagnetic Latitude	22
4.1	Measurement Sites for Satellite Transmission Experiment	25
4.2	Scintillation Observed in Geostationary Experiments, Scatter Plot	27
4.3	Structure Sizes Observed in PRAIRIE SMOKE II and IV	30
4.4	Variation of Peak Scintillation in Briggs and Parkin Formulation	33
4.5	Comparison of Measured Scintillations with Briggs and Parkin Model	33
5.1	Coordinate System for Modified Scintillation Model	35
5.2	1/e Contour of Electron Density Variance in Heated Region	38
5.3	Angle Variation of Scintillation Index Using Modified Theory	41
5.4	Effect of Varied 1/e Radius R	42
5.5	Effect of Northward Displacement y_m of Center of Heated Region	44

ILLUSTRATIONS (Cont.)

NO.		PAGE
5.6	Comparison of Model with Experimental Data, Satellite Pass 1	47
5.7	Comparison of Model with Experimental Data, Satellite Pass 2	48
5.8	Comparison of Model with Experimental Data, Satellite Pass 3	48
6.1	Maximum Striation Scale Size for Far-Field Approximations to be Valid	53
6.2	Scintillation Parameter β and RMS Phase Angle Fluctuation ϕ_o as Functions of Scintillation Index S_2	56
6.3	Radar Detection Probability Versus Scintillation Index, Non-Fluctuationg Target, $P_f = 10^{-4}$	60
6.4	Radar Detection Probability Versus Scintillation Index, Non-Fluctuating Target, $P_f = 10^{-8}$	61
6.5	Ratio of Detection Range to Vacuum Detection Range as Function of Scintillation Index, for Non-Fluctuating Target and $P_f = 10^{-4}$	64
6.6	Ratio of Detection Range to Vacuum Detection Range as Function of Scintillation Index, for Non-Fluctuating Target and $P_f = 10^{-6}$	65
6.7	Ratio of Detection Range to Vacuum Detection Range as Function of Scintillation Index, for Non-Fluctuating Target and $P_f = 10^{-8}$	66
6.8	Flow Chart for Monte-Carlo Tracking Simulations	71
6.9	RV Trajectory Relative to Radar	72
6.10	Tracking the RV Trajectory in the Presence of Artificially Induced Scintillations	75
6.11	Angle Error Sigmas Due to Scintillations and Radar Measurement Errors	77
6.12	Relative Mean Prediction Error as Function of Scintillation Index for Several Values of Scale Size Over Wavelength, Case 1: Scintillations First	78

ILLUSTRATIONS (Cont.)

NO.		PAGE
6.13	Relative Mean Prediction Error as Function of Scintillation Index for Several Values of Scale Size Over Wavelength, Case 2: Scintillations Last	79
6.14	Relative Mean Prediction Error as Function of Scintillation Index	80
6.15	Relative Mean Prediction Error as Function of Prediction Time After Track	81
6.16	Relative Mean Prediction Error as Function of Angle Error Direction	82
6.17	Relative Mean Prediction Error as a Function of Radar Parameter K	84
7.1	Probability of Element Error on One Link of a Binary DPSK Communication System	90
7.2	Probability of Element Error on One Link of a Binary DPSK Communication System	91
7.3	Degradation of Binary DPSK Communication Link as Function of Scintillation Index S_2	93
A.1	Scintillation Index S_4 as a Function of S_2 for Several Assumed Distributions of Amplitude	97
A.2	Fading Depth in dB	100

1 INTRODUCTION AND SUMMARY

Since about 1970 experimenters have been heating the F-region of the ionosphere with high-power, ground-based RF transmitters, creating local perturbations of up to 30 percent in the temperature and 1 percent in the electron density of the ionospheric plasma. These artificially produced disturbances are observable in modified optical emissions, in radar backscatter and forward-scatter, in ionograms, and in scintillations produced in radio signals traversing the disturbed region.[1] Although artificial modification of the ionosphere has been carried out in the past by release of chemicals from rockets and detonation of atomic bombs, RF heating of the ionosphere is, in contrast to these means, controllable, repeatable, and rapidly self-reversing.

The ionospheric modification experiments have been conducted using a transmitter constructed near Platteville, Colorado, by the Institute of Telecommunication Sciences of the US Department of Commerce. (A few experiments have also been run using the 300-meter antenna at Arecibo Observatory, Puerto Rico.) Project IVORY CORAL, sponsored by the Defense Advanced Research Projects Agency (DARPA), has encompassed a number of theoretical and laboratory studies conducted to develop an understanding of ionospheric modification, and a number of diagnostic field experiments (known as Project PRAIRIE SMOKE) were conducted with the Platteville transmitter during 1972-73. Studies of possible systems applications of ionospheric modification--for example, as a communications medium--and some feasibility demonstrations were also sponsored by DARPA as Project SMOOTH LEDGE.

The present study, a part of Project SMOOTH LEDGE, was undertaken to examine the possible systems implications of the scintillation produced in radio signals propagating through an artificially modified ionosphere. The objectives of this study were to:

- Describe and organize the scintillation data measured in the PRAIRIE SMOKE experiments

- Fit the measured data to a theoretical scintillation model which can then be used to predict further effects
- Relate the scintillation data to parameters which describe or determine the degradation of radar or communication system performance

As part of the PRAIRIE SMOKE experiments, Aeronomy Corporation measured the scintillations produced by the modified ionosphere in VHF signals transmitted from polar orbiting and geostationary satellites to ground receiving stations. Aeronomy Corporation used their data to diagnose the size and shape of the modified region and the ionization levels and correlation lengths which determine its small-scale structure. Much of their measured data, along with descriptions of their experimental configurations and the satellite systems employed, were made available to us.

The measured scintillations due to the artificially modified ionosphere were compared to the predictions of the Briggs and Parkin model for scintillation in the natural ionosphere.[2] Although a Briggs and Parkin model had been assumed in deriving many of the parameters describing the modified region, that model failed to predict the observed variation in scintillation with the angle between the geomagnetic field and the transmitter-to-receiver line-of-sight. The disagreement was soon attributed to the finite dimensions of the modified region as compared to the assumed infinite horizontal extent in the Briggs and Parkin model. When the model was refined to account for the finite region, good agreement between measurements and model predictions was obtained.

The principal effects of the artificially modified ionosphere on a radar forced to look through it are amplitude scintillations in the received signal and scintillations in angle of arrival of the signal.*

*Phase coherence in the signal may be degraded as well, but the effects should be negligibly small over the short duration of most radar pulses. Effects of phase coherence have not been treated explicitly in this study.

For an assumed Rice probability distribution of the amplitude fluctuations, the degradation in radar detection probability and in detection range were determined parametrically for a wide range of signal-to-noise ratios and scintillation indexes. The radar angle errors produced by various levels of scintillation were also developed. In order to assess the overall effect of the artifically modified ionosphere on radar tracking, a Monte Carlo computer simulation was used to determine the resultant errors in predicting the intercept point for a ballistic missile in two cases: first, when the radar viewed the missile through the modified ionosphere just as the missile appeared above the horizon, and, second, when the disturbed tracking occurred only at the end of the tracking interval. The resultant intercept point errors were computed for many choices of scintillation index and parameters of the modified region.

The degradation in the bit error rate in satellite-to-ground DPSK (differential phase-shift keying) and NFSK (non-coherent frequency-shift keying) digital communications was computed for the assumed Rice distribution of amplitude fluctuations as a function of the scintillation index.

Most of the parametric results derived for radar detection and tracking and for satellite communication depend only upon the intensity of the scintillation and not its source, so that the results could be applied to natural scintillation or to nuclear-weapon-induced scintillations as well as to those produced by ionospheric heating.

Briefly summarized, the principal conclusions of the study are:

- RF heating of the ionosphere can produce scintillations about twice as great as those observed in the normal daytime ionosphere in the middle latitudes. The largest amplitude scintillation measured in PRAIRIE SMOKE at 150 MHz was about 10 dB peak-to-peak; most values were much less.

- The enhanced scintillation is produced only along lines of sight through the heated region, which, for the Platteville heater, subtends at most about a 20-degree cone angle at ground receiving sites. The largest scintillations occur when the line-of-sight is parallel to the geomagnetic field.
- Amplitude and phase scintillations can degrade radar detection and tracking and satellite communication error rates. However, possible intentional degradations produced by ionospheric modification can be largely discounted because:
  1. The scintillations are produced only in a small angular sector of the sky.
  2. Scintillation scales with frequency at a rate between f^{-1} and f^{-2}. Systems operating at UHF and above should experience only a small fraction of the scintillation measured in the experiments at 150 MHz.
  3. The margin usually engineered into systems to account for severe natural scintillation may offset the worst effects of artificially produced scintillation. At any rate, the largest natural scintillations are likely to be several times worse than those produced by RF heating. (For example, 8 dB fading has been observed on satellite communication channels at 6 GHz.)

Section 2 of this report describes the natural ionosphere and ionospheric modification. Section 3 summarizes a simple theory of ionospheric scintillation and describes the extent of natural scintillation. Section 4 describes the satellite transmission experiments in PRAIRIE SMOKE and compares the measured data with values derived from the simple scintillation model; Sec. 5 presents the refined scintillation model.

The degradation of radar detection and tracking is discussed in Sec. 6 and the degradation of satellite communication is discussed in Sec. 7.

2 IONOSPHERIC MODIFICATION

2.1 THE NATURAL IONOSPHERE

The ionosphere is the portion of the earth's upper atmosphere in which enough of the constituent gases are ionized to affect the propagation of radio waves. For practical purposes the ionosphere extends from about 50 km altitude out to several earth radii. It is conventionally divided into three regions: D (50 to 90 km), E (90 to 130 km), and F (above 130 km). In addition, the E- and F-regions are divided into layers, of which the F_2 layer, at about 300 km, is the most important from the point-of-view of radio propagation.

At 300 km altitude, 1 cubic meter of the ionosphere contains about 10^{14} to 10^{15} neutral particles (CIRA 1965 model atmosphere) and about 10^{11} to 10^{12} electrons and an equal number of positive ions, chiefly O^+. Because of their much smaller masses, the electrons are more mobile than the positive ions and hence determine most of the electrical properties of the ionosphere. The electrons oscillate weakly at the plasma frequency, which is proportional to the square root of the electron density, and reflect or absorb radio waves at that frequency or lower. The highest plasma frequency in the ionosphere is called the critical frequency of the F-layer; it typically ranges from 5 to 10 MHz.

Because of the earth's magnetic field, the ionosphere is birefringent with two modes of propagation which travel at different velocities and which refract differently. The modes are usually denoted "O," for ordinary, and "X," for extraordinary. The O-mode has approximately right-circular polarization and tends to deviate normal to the magnetic field; the X-mode is approximately left-circular and tends to deviate parallel to the magnetic field. In practice, the O-mode and the X-mode have different critical frequencies, denoted f_o and f_x. Since there are critical frequencies associated with all of the ionospheric layers, these frequencies in the F_2 layer are usually labeled f_oF_2 and f_xF_2.

2.2 MODIFYING THE ATMOSPHERE

Local perturbations of the ionosphere are being created by delivering large amounts of energy into the F_2 layer from a high power RF transmitter operating near the critical frequency. The transmitter, located at Platteville, Colorado (40.18°N, 104.73°W), has a peak power of about 2 MW. The antenna, designed to operate over 5 to 10 MHz, is a ring array with about a 15-degree half-power beamwidth that can be driven to generate right-circular (∿O-mode) and left-circular (∿X-mode) polarized waves. The transmitter and antenna yield a power-aperture product of about 10^{10} W·m^2 (the 300-meter antenna at Arecibo Observatory, Puerto Rico, has also been employed in ionospheric modification experiments).[1]

A detailed discussion of the physical processes involved in ionospheric heating is beyond the scope of this paper (for such a discussion, the reader is referred to Ref. 3). However, a very simplified description is as follows:

Near the altitude where the plasma frequency approximates the transmitted frequency, the electrons are driven into oscillation and convert some of the RF energy into random thermal motion as they collide with ions and neutral particles. Because of this increased thermal motion, the ambient electron temperature is increased. Heat is conducted away from the altitude of absorption by electrons diffusing along the geomagnetic field lines. Because of instabilities the diffusion process results in a striated structure of temperature irregularities extended along the field lines. This diffusion also modifies the electron density in the heated region, resulting in local variations in the mean electron density. The local variation in the electron density is important in determining the diffraction and backscattering properties of the heated region. A schematic view of ionospheric heating is shown in Fig. 2.1.

2.3 EXPERIMENTAL STUDIES OF THE MODIFIED IONOSPHERE

Most of the experimental techniques used to study the normal ionosphere can be employed to measure the properties of the modified

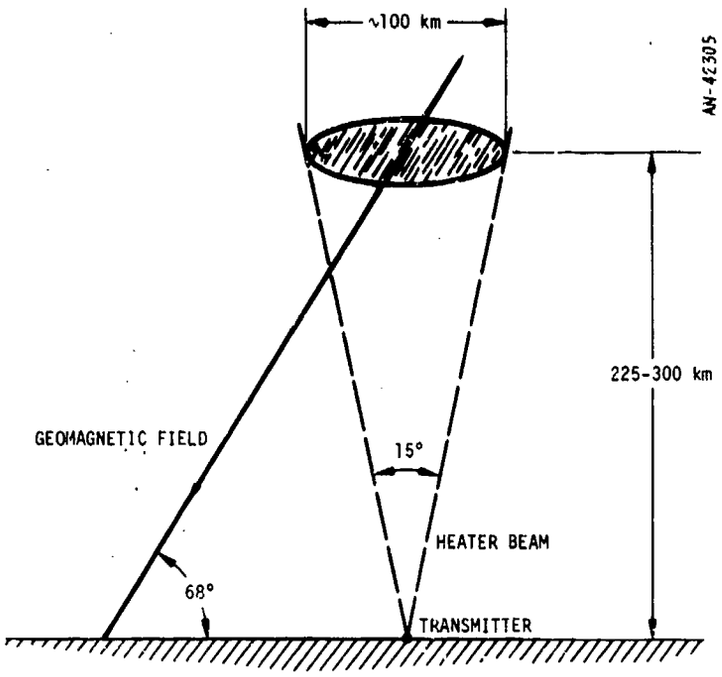

Figure 2.1. Schematic of Ionospheric Modification

ionosphere. One of the principal tools used in ionospheric studies is the ionosonde, a kind of swept-frequency radar used to produce plots--called ionograms--of the height of radio reflection as a function of frequency and to determine, among other properties, the critical frequencies of each layer. Ionograms taken of the normal ionosphere usually show well-defined narrow traces of reflection height in the F-region, indicating that reflections occur at one height for each frequency. Ionograms of the heated region, however, show the occurrence of "spread-F," a widening of the trace indicating scattering from irregularities over a considerable thickness of the ionosphere.[4] Spread-F occurs naturally, but usually only at night (at Boulder), and is usually accompanied by increased scintillation. The heating of the ionosphere creates spread-F irregularities even in daytime shortly after the transmitter is turned on.

Modifications in the ionosphere have been observed in optical emissions.[7,8] Emissions at 630 nm are normally produced in the dissociative

recombination of electrons and O_2^+ ions, a reaction which proceeds more slowly as the temperature is raised. Biondi, et al.,[7] measured a decrease in 630-nm emissions in the heated ionosphere corresponding to about a 35-percent increase in the temperature. Evans, et al.,[8] reported an enhancement in the 1.27-μm emission of molecular oxygen believed also to be due to the increased temperature in the heated region.

Measurements of radar backscatter were used to determine the radar cross section of the heated region, the frequency dependence of that cross section, and to investigate the aspect sensitivity of the backscatter. If the irregularities (or striations) in the heated region are highly elongated and aligned with the geomagnetic field, reflections would be expected to be very sensitive to aspect angle. A radio wave incident on the irregularities making a small angle θ to the normal plane to the field line would be scattered in a cone at angle $-\theta$ to the field normal. A simple analogy is the scattering of a flashlight beam by a bundle of parallel glass rods. The predicted aspect sensitivity--confirming the field alignment of the irregularities--was observed by bistatic measurements from sites about 350 km (magnetic) south of Platteville and by RAM radar measurements from White Sands Missile Range somewhat further south.

A fourth type of experiment measured the scintillation statistics of satellite radio signals passing through the heated region to receiving stations on the ground. The experiments were carried out by Aeronomy Corporation during PRAIRIE SMOKE I-V using both geostationary and polar-orbiting satellites transmitting in the VHF and UHF bands. Ground receiving sites were chosen to view the satellites along lines-of-sight passing through the heated region. In viewing the geostationary satellite, the line-of-sight remained fixed, but in viewing the orbiting satellite the line-of-sight swept through the heated region in a few minutes as the satellite made a north-to-south (or south-to-north) orbital pass. For most of the orbital experiments the receiving stations were placed near the down-field point (about 120 km (magnetic) north of Platteville) so

that the line-of-sight through the heated region would be as nearly parallel to the magnetic field as possible.

The satellite transmission experiments provided considerable information on the size and structure of the heated region and its scattering properties, including:

- Field alignment of irregularities
- Dimensions and orientation of correlation ellipsoids for large and small irregularities
- Drift velocity of irregularities
- Altitude and horizontal dependence of signal fluctuations
- Intensity, time scale, and frequency dependence of signal fluctuations

Since ionospheric scintillation induced by ionospheric modification is the principal focus of this paper, the results of the satellite experiments are very important tc our conclusions. Most of the results of the satellite transmission experiments require interpretation in terms of the theory of ionospheric scintillation. In order to make those interpretations most readily understandable, we defer further discussion of the satellite experiments to Sec. 4 and present some of the most important aspects of scintillation theory in Sec. 3.

3 THEORY OF IONOSPHERIC SCINTILLATION

Shortly after the existence of radio stars and galaxies was discovered, fluctuations in the amplitude of the received signals were observed. By studying the correlation between fluctuations observed at separated antennas it was determined that the signal scintillations are primarily produced in the ionosphere, and principally in the F-region where the ionization is strongest. The advent of artificial earth satellites in 1957 led to increased interest in ionospheric scintillation, both to understand possible degradation of communication signals as well as to employ satellites as tools in developing an understanding of the structure and propagation properties of the ionosphere.

Scintillations induced in radio waves passing through the ionosphere have been studied theoretically for about twenty-five years.[2,7-11] Most of the results of interest to the present problem are drawn from Refs. 2, 10, and 11.

3.1 THE IONOSPHERE AS A PHASE SCREEN

A common approach in these papers is to equate the effect of the ionosphere to that of a thin screen which modulates the phase or amplitude of the wave passing through it. (Bowhill[10] worked with an amplitude-modulating screen, but had shown earlier the equivalence between shallow amplitude and phase screens. We shall consider only phase screens here.) The statistics of the phase screen are described by a two-dimensional stationary covariance function. Bowhill considered only shallow screens whose RMS phase variation was less than 1 radian; Mercier[11] considered large phase variations; and Briggs and Parkin[2] extended some of Mercier's results to the non-isotropic phase screen.

The complex amplitude of a signal propagating in the positive z-direction emerging from the random phase screen at the plane $z = 0$ (see Fig. 3.1) is

$$A(x,y,0) = A_o \exp\left(j\phi(x,y)\right)$$

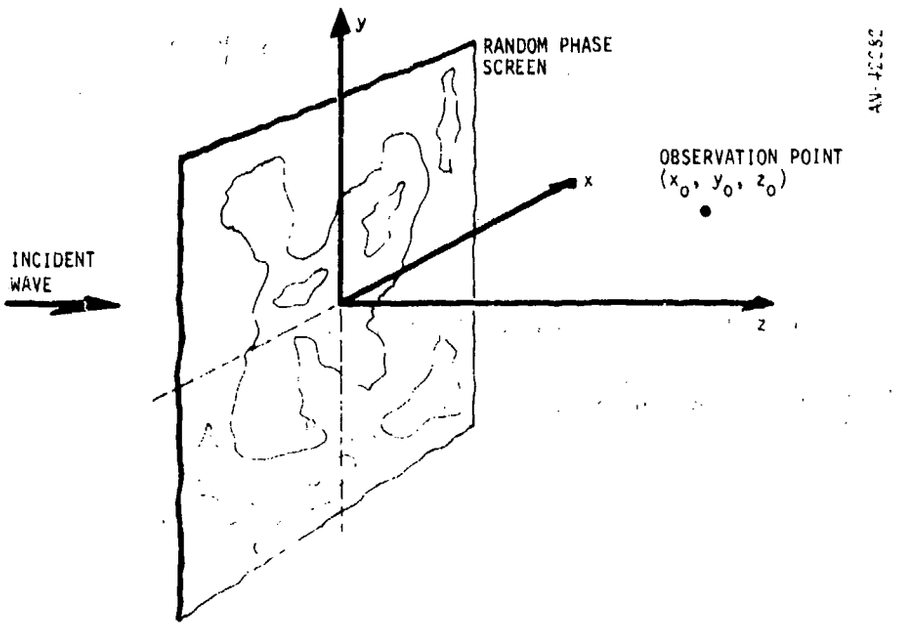

Figure 3.1. Diffraction by a Random Phase Screen

---

where $\phi(x,y)$ is a real stationary random function with covariance $\phi_o^2 \rho_\phi(x_i - x_j, y_i - y_j) = E\left[\phi(x_i,y_i)\phi(x_j,y_j)\right]$, where $E[\cdot]$ denotes expected value or ensemble average. The incident wave is assumed to be plane at the phase screen. An observer in a plane removed from the phase screen observes the amplitude $R = (AA^*)^{1/2}$ of the diffracted and refracted wave, where $A(x,y,z)$ is the complex amplitude. Our concern is with the statistics of R and its covariance function in the observation plane.

3.1.1 The Phase Screen--Briggs and Parkin Theory

Because of the ionization in the F-region of the ionosphere, the refractive index deviates from unity and the total phase change of a wave propagating through the region differs from the phase change accumulated over an equal path in free space. At frequencies well above the plasma frequency of the medium, typically of the order of 5 MHz, the refractive index is given approximately by

$$\mu \simeq 1 - \lambda^2 r_e N/(2\pi)$$

where λ is the wavelength, r_e is the classical electron radius $\left(= e^2/(4\pi\varepsilon_o mc^2) \simeq 2.82 \times 10^{-15}\ \text{m}\right)$, and N is the electron density. The deviation of the refractive index from the mean value due to local variations in the electron density is given by $\Delta\mu = -\lambda^2 r_e \Delta N/(2\pi)$, where ΔN is the deviation of N from its mean value. Then the phase change in traveling a distance L in the medium, relative to the phase change in traveling an equal distance in a uniform medium with the same mean electron density, is

$$\phi = \frac{2\pi}{\lambda} \int_0^L \Delta\mu \, d\ell = -r_e \lambda \int_0^L \Delta N \, d\ell$$

Briggs and Parkin[2] derived expressions for the RMS phase fluctuations in a wave passing through a slab in which the electron density variation consists of a large number of striations elongated along the direction of the geomagnetic field. The correlation of the electron density in the medium was taken to be

$$\rho_N(r,s) = \exp\left[-r^2/r_o^2 - s^2/(\alpha r_o)^2\right]$$

where r and s are cylindrical coordinates such that s is measured along the magnetic field and r is measured perpendicular to it (see Fig. 3.2); r_o is a characteristic dimension of the medium which is very important in the ensuing discussion.

For a wave incident at angle i upon a slab of thickness Δh, the path length through the slab is $L = \Delta h \sec i$ (see Fig. 3.3). Briggs and Parkin derived the mean square phase variation for the wave to be

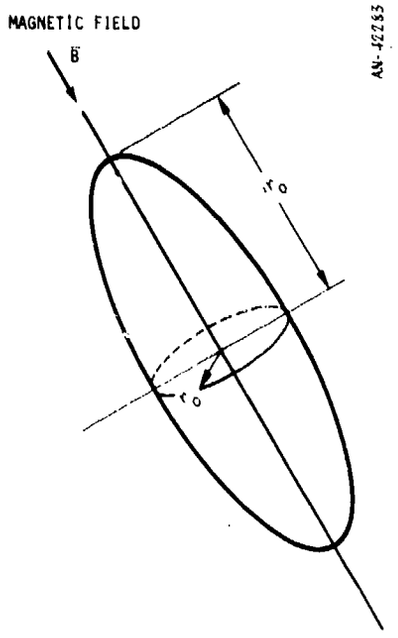

Figure 3.2. Dimensions of Field-Aligned Striations

$$\phi_o^2 = E(\phi^2) = \frac{\pi^{1/2} r_e^2 \lambda^2 E(\Delta N^2) \Delta h \alpha r_o \sec i}{(\alpha^2 \sin^2 \psi + \cos^2 \psi)^{1/2}} \tag{3.1}$$

where ψ is the angle between the magnetic field vector $\bar{B}$ and the normal to the incident wave. The correlation function for the phase fluctuation in the wave emerging from the slab is

$$\rho_\phi(u,v) = \exp\left[-u^2/r_o^2 - v^2/(\beta r_o)^2\right] \tag{3.2}$$

where

$$\beta = (\alpha^2 \sin^2\psi + \cos^2\psi)^{1/2} \tag{3.3}$$

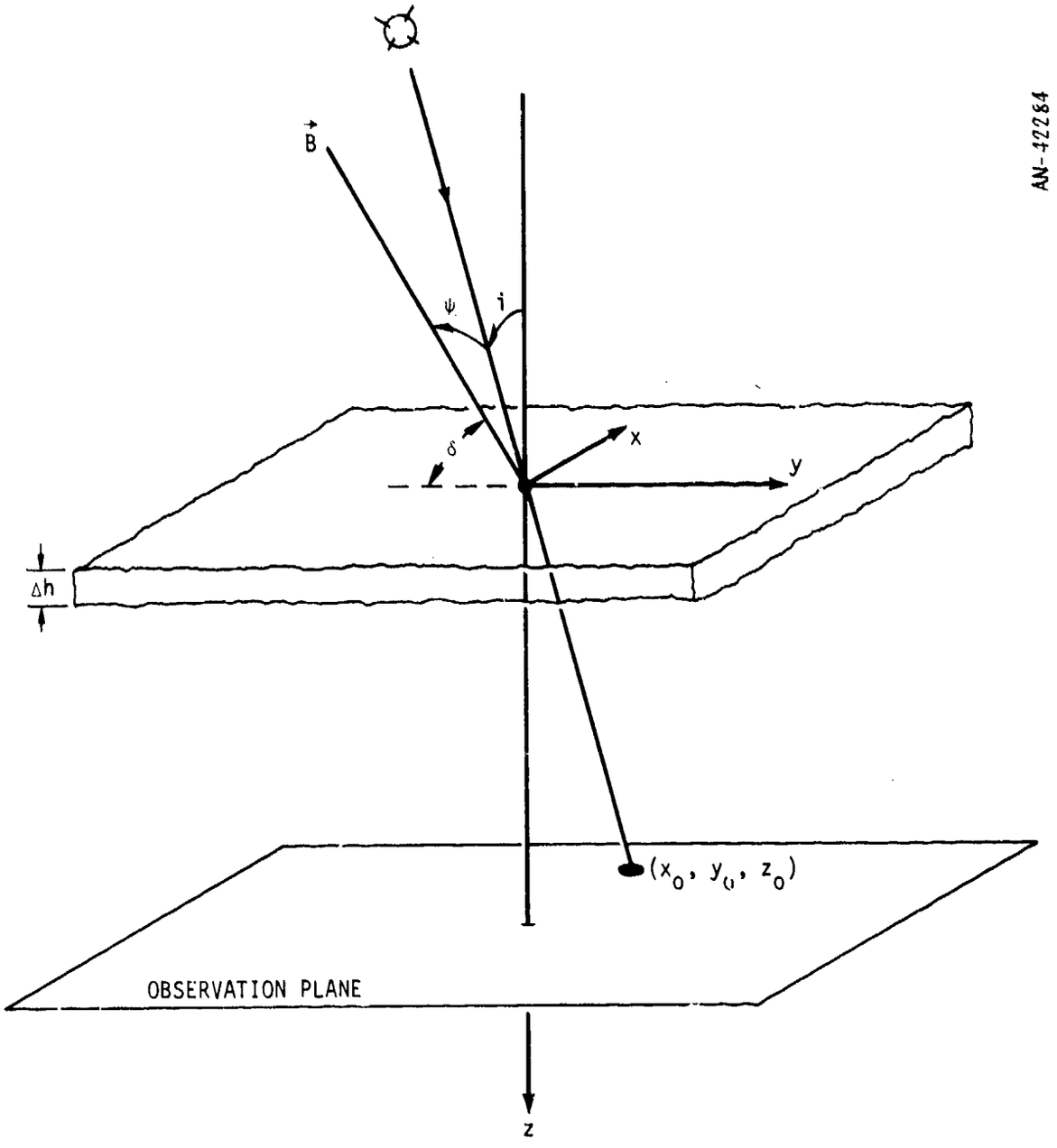

Figure 3.3. Geometry of Ionospheric Slab in Briggs and Parkin Theory[2]

3.2 STATISTICS OF THE DIFFRACTED WAVE

As the wave propagates away from the phase screen, the diffracted components of the wave begin to interfere constructively and destructively with the undiffracted or "specular" components so that the amplitude of the signal scintillates. In this section we are concerned with the following issues:

- What are the statistical properties of the amplitude and phase scintillations of the observed wave?
- How do the statistics vary with the distance z_o between the phase plane and the observer plane?
- How are the scintillations correlated in the observer plane and how does the correlation relate to the correlation in the phase plane?

The measurements in the observer plane are usually either of $R = (AA^*)^{1/2}$ or R^2. As measures of scintillation depth we use the normalized standard deviation of these quantities defined as

$$S_2 = \left[E(R^2) - \left(E(R)\right)^2\right]^{1/2} / E(R)$$

and

$$S_4 = \left[E(R^4) - \left(E(R^2)\right)^2\right]^{1/2} / E(R^2)$$

These scintillation indexes are both used throughout this report; S_4 is generally used in the theoretical developments while S_2 is generally used in discussions of measurements. For practical purposes, the two indexes are related to each other as $S_2 \simeq 0.5S_4$. The exact relationship depends upon the statistical distribution of R. This relationship for some representative distributions and some alternative scintillation indexes are discussed in the appendix.

For the case of very large $z_o (z_o \to \infty)$, Mercier[11] derives the following results:

$$E(R^2) = A_o A_o^* \qquad \text{(true for all } z_o\text{)} \tag{3.4}$$

$$E(R^4) = A_o A_o^* \left[2 - \exp\left(-2\phi_o^2\right)\right] \tag{3.5}$$

$$S_4^2 = 1 - \exp\left(-2\phi_o^2\right) \tag{3.6}$$

$$\rho_{R^2}(u,v) = \frac{\exp\left[2\phi_o^2 \rho_\phi(u,v)\right] - 1}{\exp\left(2\phi_o^2\right) - 1} \tag{3.7}$$

Mercier shows that, as z_o becomes large, all of the even-order moments of R coincide with the even-order moments of the Rice distribution, which is the distribution of the amplitude of a constant signal plus in-phase and quadrature Gaussian noise. Mercier then asserts that R indeed has a Rice distribution. The many small signal components scattered from irregularities in the phase screen appear to add together randomly and independently (and thus becoming normal by the Central Limit Theorem), while the unscattered component of the field represents the constant term to which the normal random components are added to yield a Rice distribution. Some of the other possible distributions for R are discussed in the appendix.

In the general case, the expression for $E(R^4)$, and consequently S_4, as a function of ϕ_o and z_o is a complicated expression which is amenable to numerical evaluation only for $\phi_o^2 \leq 10$. However, in certain circumstances approximate expressions can be developed.

For small ϕ_o Mercier developed the approximation

$$S_4^2 = 2\phi_o^2\left(1 + \pi^2 r_o^4/4\lambda^2 z_o^2\right)^{-1} \tag{3.8}$$

which is valid for all z_o. As z_o approaches infinity we have

$$S_4 \simeq \sqrt{2}\phi_o \tag{3.9}$$

while for $z_o << r_o^2/\lambda$ we have

$$S_4 \simeq 2\sqrt{2}\left(\lambda z_o/r_o^2\right)\phi_o/\pi \tag{3.10}$$

For $\phi_o > 1$, however, a peak occurs in S_4 in the vicinity of $\lambda z_o/r_o^2 = \pi/\sqrt{3}\phi_o$ as a result of a focusing effect which is not predicted by the approximate expressions. This focusing can be visualized as the result of the irregularities refracting rays which converge together into one zone. In the focusing zone, the scintillation index S_4 can exceed 1. This result seems odd in comparison to a Rayleigh distribution, in which all of the power is in the fluctuation, but for which $S_4 = 1$. However, in the focusing zone the in-phase and quadrature terms are not independent so that the fluctuations are more likely to add in phase with the specular component and give a larger amplitude. As z_o becomes larger, the components become more random and the scintillation index approaches 1.

Figure 3.4 illustrates the behavior of S_4 with z_o for selected values of ϕ_o. The focusing effect yielding $S_4 > 1$ is evident for $\phi_o > 1$. This curve was computed from the approximate expressions given by Singleton,[12] who used some results from geometric optics. Figure 3.5, taken from Singleton, illustrates contours of constant scintillation index S_4. Region I is the "near zone" where $S_4 \simeq \phi_o z_o$; Region II is the "far zone" where $S_4 \simeq \sqrt{1 - \exp\left(-2\phi_o^2\right)}$; Region III is a "saturation zone" where $S_4 \simeq 1$; and Region IV is the "focusing zone" where $\lambda z_o/r_o^2 \simeq \pi/\sqrt{3}\phi_o$ and where $S_4 > 1$.

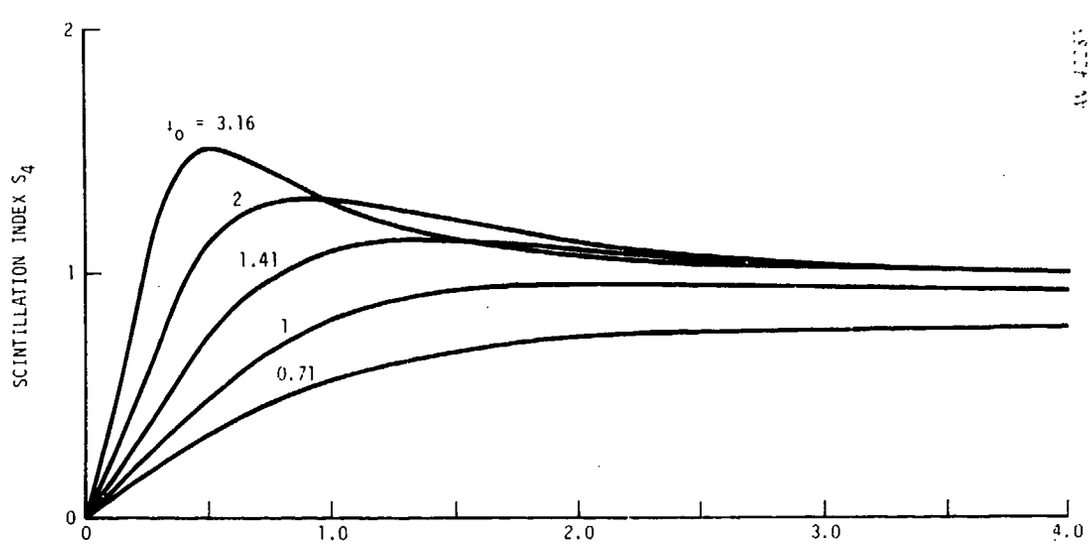

Figure 3.4. Development of Scintillation with Viewing Distance from Phase Screen

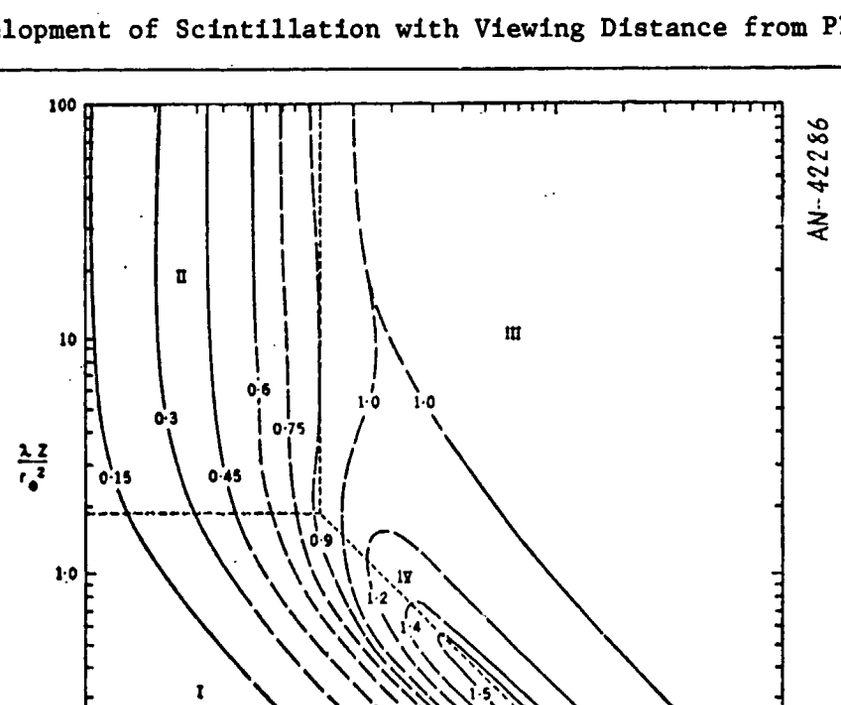

Source: Ref. 12

Figure 3.5. Curves of Constant Scintillation Index S_4 on a Plot of $\lambda z/r_o^2$ vs ϕ_o . The broken lines correspond to the exact solution; the full lines to the approximations.

The calculations have assumed an isotropic screen; that is, $\beta = 1$ in Eq. 3.2 so that contours of equal correlation in the phase screen are circles. In general, Briggs and Parkin's theory admits $\beta > 1$, or elliptical contours of equal correlation. For this case Briggs and Parkin replace the approximation of Eq. 3.8 by

$$S_4 = \sqrt{2}\phi_o\left[1 - (\cos u_1 \cos u_2)^{1/2} \cos \frac{1}{2}(u_1 + u_2)\right]^{1/2} \qquad (3.11)$$

where $\tan u_1 = 2\lambda z_o/\pi r_o^2$ and $\tan u_2 = 2\lambda z_o/\pi\beta^2 r_o^2$. The effect of the anisotropy is to slow the rate at which S_4 approaches its limiting value as the observer moves away from the screen.

It has also been assumed that the source is infinitely far from the screen. Corrections for a source at a distance z_s from the screen can be made by replacing z_o in the preceding expressions by

$$z_o' = z_o z_s/(z_o - z_s) \qquad (3.12)$$

This result was derived by Bowhill.[10]

3.3 PHASE AND ANGLE SCINTILLATION

In addition to the amplitude scintillations in the diffracted wave, there are phase and angle-of-arrival scintillations as well. Actually, the angle-of-arrival scintillation is a consequence of the rate of change of signal phase with observer position. The deviation in angle of arrival is given by

$$\theta = (\lambda/2\pi)\frac{d\phi}{dx} \qquad (3.13)$$

where $\phi(x)$ is the phase deviation from mean at the point of observation. If the covariance function for the phase deviations is given by

$\phi(x) = E[\phi(a + x)\phi(a)]$, where $\phi(x)$ is assumed to be stationary, then the variance of angle of arrival is given by

$$E(\theta^2) = (-\lambda^2/4\pi^2) \frac{d^2\phi}{dx^2} \qquad (3.14)$$

provided the second derivative exists at $x = 0$. In the general two-dimensional case the orthogonal components of the angle variation can be obtained in the obvious way.

Immediately beyond the phase screen, all of the power in the fluctuations is concentrated solely in the phase variations since the amplitude variations develop only as the wave propagates beyond the screen. Bowhill[10] shows that for the <u>shallow</u> phase screen, as the observation plane is far from the phase screen:

- Correlation between phase in observation plane and phase at screen → 0
- Correlation between amplitude and phase in the observation plane → 0
- For the stationary Gaussian covariance of phase at the screen, $E[\phi(x,y,z_o)\phi(x + u,y + v,z_o)] \rightarrow 0.5E[\ (x,y,0)\phi(x + u,y + v,0)]$; that is, the mean square phase variation in the observation screen tends to one-half that in the phase screen and the covariance function take the same form.

Mercier's[11] expression (3.7) for the autocorrelation function of amplitude for the shallow phase screen shows that it also takes the same form as the autocorrelation function of phase at the screen.

3.4 NATURAL SCINTILLATION

Estimates of the natural scintillation enable us to view in proper perspective the scintillation induced by the modified ionosphere. Fremouw and Rino[13] of Stanford Research Institute have recently presented a model

for the average natural F-layer scintillation at VHF/UHF which supplies parameters for the Briggs and Parkin model. The model assumes constant values for the parameters:

α = axial ratio = 10

Δh = layer thickness = 100 km

z_o = height of layer = 350 km

For the parameters r_o (= transverse scale size) and ΔN (= RMS fluctuation), formulas are given which depend upon geomagnetic latitude λ_g in degrees, local time of day in hours t, day of the year D, and sunspot number R. The scale size r_o is assumed to depend on latitude only, assuming the value 300 meters near the equator and 900 meters in latitudes from about 15 to 60 degrees. In the middle latitudes ΔN depends upon only latitude and time according to

$$\Delta N = (6 \times 10^8)(1 + 0.4 \cos \pi t/12) \exp\left[-(\lambda_g - 32.5)^2/100\right] \qquad (3.15)$$

where ΔN is in units of electrons per cubic meter.

For the geomagnetic latitude of Boulder (about 40 degrees), we have calculated the expected average scintillation index S_4 as a function of scan angle i off vertical in a magnetic north-south plane using the values from the Fremouw and Rino model, the Briggs and Parkin model for ϕ_o^2, and expression (3.11) for the scintillation index. The wavelength is 2 meters, and the source is assumed to be infinitely far away. Since the dip angle is about 68 degrees near Boulder, the angle ψ to the magnetic field goes to zero at $i = -22$ degrees. The average scintillation index S_4 is plotted in Fig. 3.6 for local times of midnight, noon, and 6 a.m. and p.m. Recall that the scintillation S_4 is about twice the index S_2 reported by Bowhill.[10]

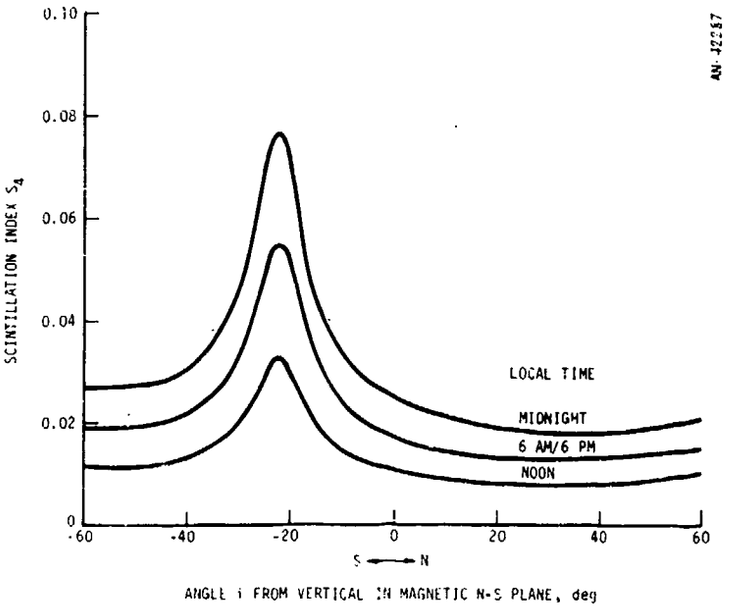

Figure 3.6. Average Natural Scintillation at 150 MHz for 40°N Geomagnetic Latitude

---

In geomagnetic equatorial regions the Fremouw and Rino model gives

$$\Delta N = (5.5 \times 10^9)(1 + 0.05R)\left|1 - 0.4 \cos \pi(D + 10)/91.25\right| \cdot \left\{\exp\left[-(t/4)^2\right] + \exp\left[-(t - 23.5)^2/3.5^2\right]\right\} \cdot \left\{\exp\left[-(\lambda_g/12)^2\right]\right\} \qquad (3.16)$$

This expression assumes its largest values at the equator ($\lambda_g = 0$), at night, around the autumnal and vernal equinoxes ($D \simeq 80$ and 266), and increases with sunspot number ($R \simeq 100$ corresponding roughly to a sunspot maximum). For $t = 0$, $D = 80$, $R = 50$, and $\lambda_g = 0$, we obtain $\Delta N \simeq 2.7 \times 10^{10}$. In comparison, the model's peak value for Boulder is about 4.8×10^8, or about 50 times smaller.

For vertical incidence at the geomagnetic equator, the Briggs and Parkin equation for ϕ_o using the values from the Fremouw and Rino model at 150 MHz (λ = 2 meters) yields $\phi_o \approx 1.1$. Since a ground observer is in the far zone, the scintillations are fully developed and one would expect $S_4 \approx 1$. Under the same conditions at noon, however, $\phi_o \approx 10^{-4}$ so that the scintillations would be negligibly small.

Large natural scintillations in communication satellite signals at 4 and 6 GHz are observed occasionally in equatorial regions. These were reported by Craft and Westerlund[14] and by Taur.[15] The scintillations sometimes exceed 6 to 8 dB peak-to-peak, or, equivalently, $S_4 \geq 0.25$. Taur reports that these scintillations occur less than 1 percent of the time, that their occurrence coincides very closely with sunset in the F-region, about 2000 local time, and that they occur most frequently around the equinoxes.

Models of average VHF scintillation do not predict these strong scintillations at much higher frequencies. For example, the Fremouw and Rino model, under conditions which give $\phi_o \approx 1.1$ at 150 MHz with resultant strong fading, would predict $\phi_o \approx 0.03$ at 6 GHz. Because of the small wavelength at 6 GHz and the large structure sizes, the ground observer would be in the near zone and resultant scintillation index S_4 would be about 0.005. The much stronger scintillations observed occasionally at SHF imply that the electron density fluctuations are probably much larger than predicted by the model and that the structure sizes are small enough to bring a ground observer into the focusing zone or far field.

4 SATELLITE TRANSMISSION EXPERIMENTS

The satellite transmission experiments in PRAIRIE SMOKE I-V were conducted and reported by Aeronomy Corporation.[16-22] Transmissions from a geostationary satellite and from a number of polar-orbiting satellites were recorded at ground receiving stations located so that the line-of-sight penetrated the heated region of the ionosphere. The geostationary satellite was ATS-5, transmitting at its telemetry frequency (136.47 MHz). The orbital satellites were US Navy navigation satellites in circular polar orbits at about 1025 km altitude. These navigation satellites transmit at about 150 and 400 MHz. In PRAIRIE SMOKE III some measurements were made of pulsed signals at 30 and 50 MHz from the Lockheed satellite STP-71-2, a part of the ERIS experiment.

Two mobile receiving stations were equipped with VHF converters, HF receivers with linear detectors, and magnetic tape and strip chart recorders. One receiving station, installed in a travel trailer, was used mainly in the geostationary experiments since it was less easily moved. The other station, installed in a Winnebago vehicle shell, was easily moved and was used in the orbital experiments.

Usually, three antennas feeding separate receivers were deployed in a triangular pattern, with maximum separation up to 300 meters. The amplitude of the signal in each receiver channel was recorded on a strip chart or magnetic tape or both. Data on magnetic tape was later digitized for computer processing.

The geostationary experiments were conducted from receiving sites located near Newcastle, Lance Creek, and Lusk in Eastern Wyoming (see map, Fig. 4.1). These sites were chosen to view the ATS-5 satellite through the heated region above the transmitter near Platteville. The elevation angle to the satellite from these sites is about 40 degrees, so that the lines of sight made about a 30-degree angle with the magnetic field in the heated region.

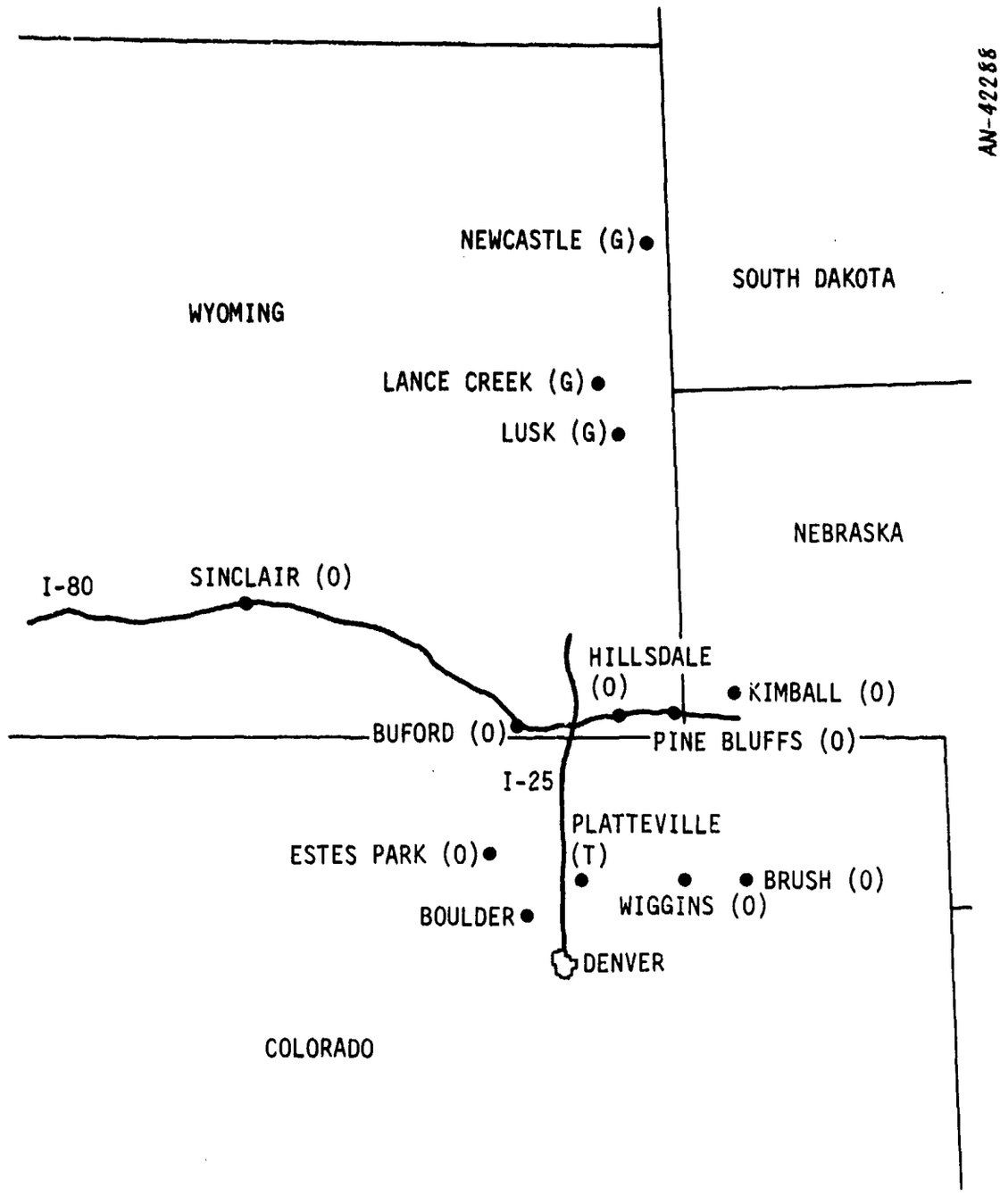

Figure 4.1. Measurement Sites for Satellite Transmission Experiment (G = geostationary, O = orbital, T = heater transmitter site)

The orbital experiments were conducted at a number of sites in Wyoming, Colorado, and Nebraska (see map, Fig. 4.1). The sites were chosen so that the line-of-sight to the satellite would sweep through the heated region during the satellite pass. Many of the measurements were made near the downfield point from the heated region--near Hillsdale, Wyoming--so that the line-of-sight to the satellite could make the smallest possible angle to the magnetic field. However, because of the earth's rotation, the roughly north-south ground track of the satellite varied from pass to pass to the east or west of the ideal track which would yield a magnetic field angle going to zero as the line-of-sight passed through the heated region. Consequently, the smallest field angle reported is about 3 degrees, but each satellite pass produced a range of field angles of interest.

4.1 STRENGTH OF SCINTILLATIONS

Quite a broad range of fading intensity was measured in the geostationary and orbital experiments. Scintillations were generally weaker for the geostationary experiments since the line-of-sight was well away from alignment with the magnetic field, but occasional strong scintillations were observed in the evening. Figure 4.2 shows a scatter plot of scintillation index S_2 observed in the geostationary experiments. There is considerable variation in the observed values due to changes in heater frequency and power on separate occasions. The strong scintillations occurring in the evening are probably due at least in part to the natural changes in the ionosphere after sunset. In one series of measurements, the natural daytime scintillation was estimated to be about 0.01 with about a 9-second period. After heating the scintillation index was in the range 0.04 to 0.10 and the fading had about a 6-second period.

Some of the orbital experiments yielded values of S_2 in the range 0.2 to 0.3 for viewing angles near the magnetic field lines. The orbital measurements will be discussed in more detail in a later section in which we compare the experimental results to the theoretical predictions.

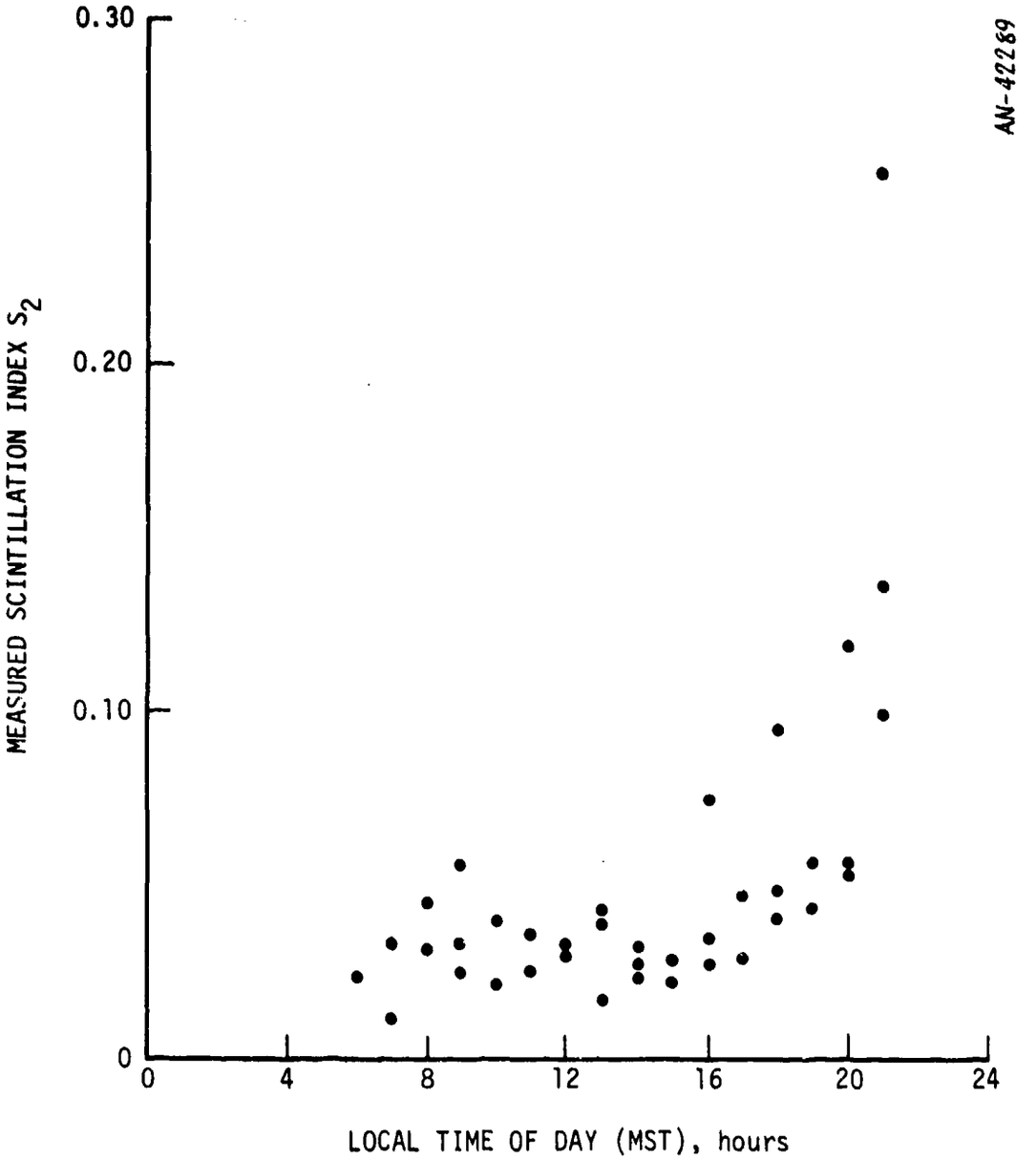

Figure 4.2. Scintillation Observed in Geostationary Experiments, Scatter Plot

Some variation of scintillation intensity on heater power and heater frequency was observed; however, the dependence is not very well determined. For f_H (the heater frequency) greater than $1.02f_oF_2$ (the critical frequency), very little modification is produced; for $0.95f_oF_2 \leq f_H \leq 1.02f_oF_2$, the results are quite variable, with occasionally very strong scintillation produced; and for $0.75f_oF_2 \leq f_H \leq 0.95f_oF_2$, the heating effect is approximately constant. The dependence on power was very difficult to assess, but the scintillation tends to increase with increased heater power.

4.2 IRREGULARITY SIZE, ORIENTATION, AND VELOCITY

With records of signals received at the displaced antennas it was possible to estimate the size, shape, and velocity of the irregularities in the heated region. Since the signal source on the geostationary satellite is fixed, the fluctuations in the recorded signals were principally due to the drift of irregularities in the ionosphere relative to the line-of-sight. By measuring the average time between signal peaks at each site, one can estimate the ratio of the structure size to its velocity. (For example, a 10-second fade period could be caused by a 10-meter structure drifting at 1 meter per second or by a 1-kilometer structure drifting at 100 meters per second.) Since the signals received at the displaced antennas were almost perfectly correlated except for a time shift, it was possible to estimate the drift velocity as the ratio of the antenna separation to the time shift between records. The structure size could then be deduced by multiplying the size-to-velocity ratio by the estimated velocity. Finally, by assuming a two-dimensional Gaussian correlation function for the phase deviation in the ionosphere, one can then relate the deduced structure size to the dimensions of the correlation ellipse.

In contrast to the geostationary measurements, the fluctuations in the received signal for the orbital satellites were due mainly to the motion of the line-of-sight relative to the irregularities as the satellite moved along its orbit at about 7200 m/s. The natural structure drift

rate of about 50 m/s was negligible in comparison. Since the satellite orbit was known very precisely, the rate of motion of the line-of-sight through the heated region could be computed and the size and orientation of the irregularities deduced from the measured period of the fluctuations. Since the line-of-sight changed from pass to pass, and since the measurement sites were moved from near the downfield point to several other sites, line-of-sight sections of the heated region from several different aspect angles were observed. Consequently, the size and field alignment of the irregularities and the size and shape of the whole region could be estimated. A histogram of the structure sizes observed in PRAIRIE SMOKE II and IV is shown in Fig. 4.3.

The conclusions regarding irregularity size and velocity are summarized below:

- About 80 percent of the time, the transverse structure size r_o lay in the range 75 to 300 meters, averaging about 100 meters.
- Some fine structure of the order of 10 meters was observed, confirming some results obtained in radar backscatter measurements.
- Drift velocity is of the order of 20 to 50 m/s in an east-west direction.
- The irregularities are elongated along the magnetic field line, having a slight banana shape tilting slightly more vertical at the top and more horizontal at the bottom.

4.3 COMPARISON OF EXPERIMENTS WITH THEORY

In order to compare the experimental results to the theoretical predictions, it is convenient to recast the Briggs and Parkin formula (Eq. 3.1) into a slightly different form. The plasma frequency f_N is related to the electron density by $f_N^2 = Nc^2 r_e/\pi$, where N is the electron density, c is the speed of light, and r_e is the classical electron

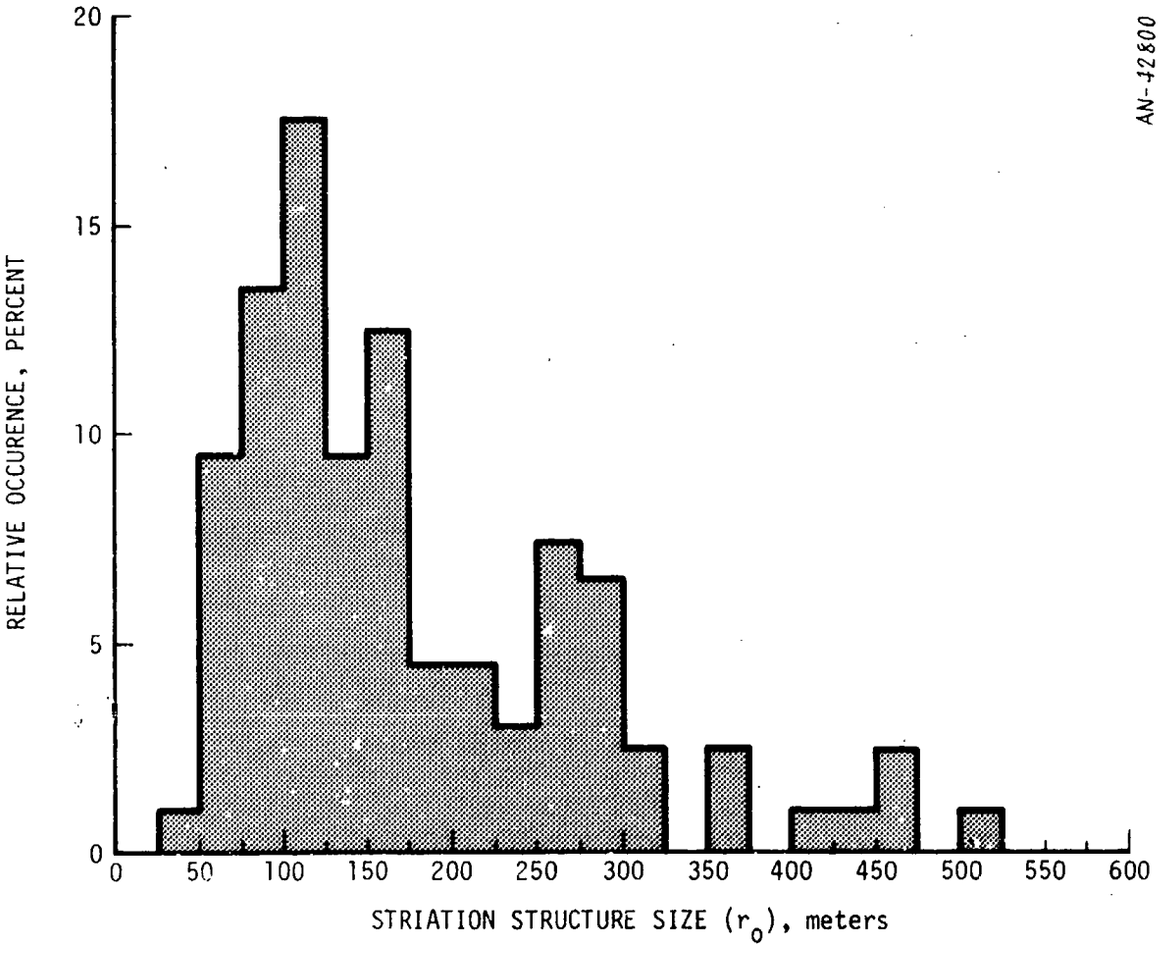

Figure 4.3. Structure Sizes Observed in PRAIRIE SMOKE II and IV

radius. If we equate the critical frequency f_oF_2 to the plasma frequency at maximum electron density N_m and recall that $c = f\lambda$, we obtain by substitution into 3.1 the result

$$\phi_o^2 = \frac{\pi^{5/2}}{\lambda^2}\left(\frac{f_oF_2}{f}\right)^4 \frac{E(\Delta N^2)\Delta h \alpha r_o \sec i}{N_m^2(\alpha^2 \sin^2\psi + \cos^2\psi)^{1/2}} \tag{4.1}$$

This form is more convenient in that the absolute value of RMS electron density deviation can be regarded more simply as a fraction of the maximum electron density.

In order to get a feeling for the numbers in Eq. 4.1, let us substitute the following values:

$\lambda = 2$m
$f = 150$ MHz
$f_oF_2 = 7.5$ MHz
$\Delta h = 100$ km
$\alpha = 10$
$r_o = 100$ m

Then

$$\phi_o^2 \simeq \frac{2.73 \times 10^3 \, E\left[(\Delta N/N_m)^2\right] \sec i}{(100 \sin^2\psi + \cos^2\psi)^{1/2}} \tag{4.2}$$

For viewing along the field line, $\psi = 0$ and $i \simeq 22$ degrees, so that $\phi_o^2 \simeq 2.94 \times 10^3 E[(\Delta N/N_m)^2]$; for vertical viewing, $\psi = 22$ degrees and $i = 0$ so that $\phi_o^2 \simeq 7.07 \times 10^2 E[(\Delta N/N_m)^2]$. The fractional deviation in electron density to achieve scintillation index $S_4 = 0.25$ is about 3.3×10^{-3} for viewing along the field and 6.6×10^{-3} for vertical viewing. Both of these correspond to $\phi_o \simeq S_4/\sqrt{2}$ for viewing in the far field.

About the only means to compare the predictions of Briggs and Parkin theory with the experimental measurements is in the variation of scintillation index with the angle ψ between the line-of-sight and the magnetic field. Since only ψ and the zenith angle vary with line-of-sight in the Briggs and Parkin formula, and since in the far field the scintillation index is directly proportional to ϕ_o, we have

$$S_4 \propto \sec^{1/2} i \left(\sin^2 \psi + \frac{1}{\alpha^2} \cos^2 \psi \right)^{-1/4} \tag{4.3}$$

Also, since the variation of $\sec^{1/2} i$ within about 10 degrees of the field line is less than 10 percent, we can neglect its effect and have instead

$$S_4 \propto \left(\sin^2 \psi + \frac{1}{\alpha^2} \cos^2 \psi \right)^{-1/4} \tag{4.4}$$

Clearly this function has a peak at $\psi = 0$ for the axial ratio $\alpha > 1$. The rate of falloff from this peak depends upon α, being very slow for small α and approaching falloff as $\csc^{1/2} \psi$ for large values of α. Figure 4.4 illustrates this variation.

For several of the orbital satellite experiments the scintillation index S_2 was plotted as a function of both time and field angle ψ. Results from one such experiment are replotted in Fig. 4.5. Because of the offset of the satellite tracks from the heated region the field angle ψ was never smaller than about 3 degrees. The heavy dashed lines across Fig. 4.5 represents falloff with ψ as $\csc^{1/2} \psi$. Although that is the fastest rate of falloff from the peak--corresponding to an infinite axial ratio--the measured falloff is somewhat faster. The Briggs and Parkin prediction does not fit the measured variation with angle very well.

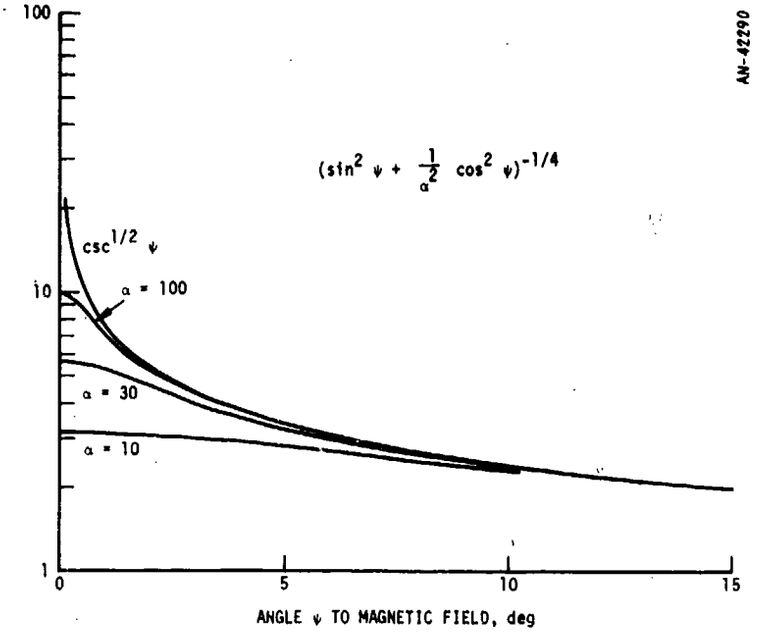

Figure 4.4. Variation of Peak Scintillation in Briggs and Parkin Formulation

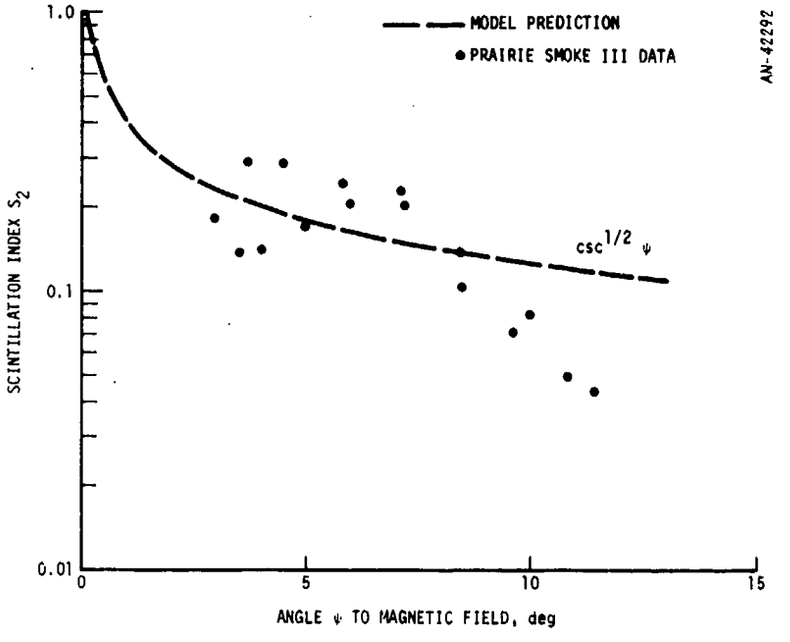

Figure 4.5. Comparison of Measured Scintillations with Briggs and Parkin Model

5 A SCINTILLATION MODEL FOR THE MODIFIED IONOSPHERE

One of the assumptions of the Briggs and Parkin scintillation model is that the layer of the ionosphere producing the scintillation is horizontally infinite with stationary statistics. However, the heated region of the ionosphere has a horizontal extent comparable to the diameter of the heater beam--about 80 km at half power at 300 km altitude. Also, since the degree of modification depends on the intensity of the heater beam, we should expect maximum effect at the center of the heated region with a decline in both horizontal and vertical directions away from the center.

A consequence of the finite size and shape of the heated region is that the phase deviation along a line-of-sight should depend not only on the zenith angle i and the field angle ψ according to the Briggs and Parkin formula, but also on how close the line-of-sight passes to the center of the heated region. To account for this additional variation, we have modified the Briggs and Parkin scintillation model to account for both horizontal and vertical variation of electron density fluctuations in the heated region. (This development follows the suggestions outlined by Drs. S.A. Bowhill and E.K. Walton of Aeronomy Corporation in a private communication.)

5.1 A MODIFIED SCINTILLATION FORMULA

Suppose that the variance $E(\Delta N^2)$ of the electron density fluctuations in the slab of ionosphere is given by

$$E(\Delta N^2) = f(x,y,z) \quad ; \quad z_{min} \leq z \leq z_{max} \tag{5.1}$$

where the characteristic dimensions of its variation are assumed to be large relative to the dimensions r_o and αr_o of the striations. The geometry is indicated in Fig. 5.1, with an observer at the origin of the coordinate system viewing a source along a line-with-direction cosines $(x_S/r_S, y_S/r_S, z_S/r_S)$ where $r_S^2 = x_S^2 + y_S^2 + z_S^2$. The magnetic field $\overline{B}$

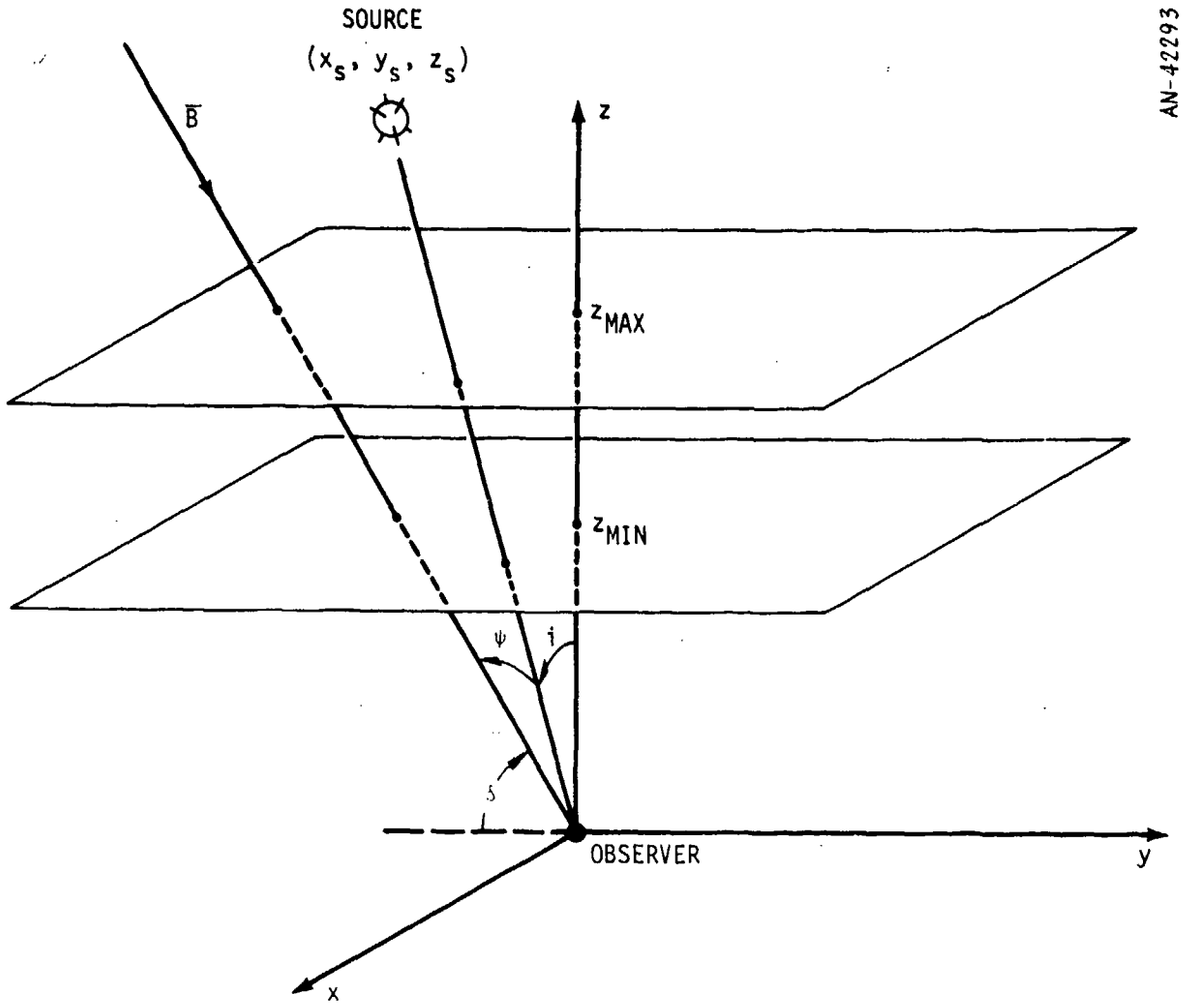

Figure 5.1. Coordinate System for Modified Scintillation Model

has a dip angle δ and lies in the yz-plane, so that the y-axis points toward magnetic north. The line-of-sight to the source makes an angle ψ to the magnetic field and a zenith angle $i = \cos^{-1}(z_S/r_S)$ to the vertical.

At each point along the line-of-sight, parameterized by altitude h as $(x,y,z) = (hx_S/z_S,\ hy_S/z_S,\ h)$ we assume that there exists a horizontal slab of incremental thickness dh (corresponding to the Δh in Briggs and Parkin's expression) contributing an incremental random phase shift $d\phi$. We assume that the mean square variation in the electron density in the slab is given by the value $E(\Delta N^2) = f(x,y,z) = f(hx_S/z_S,\ hy_S/z_S,\ h)$ appropriate for the point at which the line-of-sight pierces the slab. Then to obtain the total mean square phase variation contributed along the line-of-sight we integrate to obtain

$$\phi_o^2 = E(\phi^2) = \pi^{1/2} r_e^2 \lambda^2 \alpha r_o \beta^{-1} \sec i \int_{z_{min}}^{z_{max}} f(hx_S/z_S,\ hy_S/z_S,\ h)\, dh \qquad (5.2)$$

This reduces exactly to the Briggs and Parkin formula (3.1) for the case f = constant and $\Delta h = z_{max} - z_{min}$.

We shall assume that the correlation function in the horizontal plane for the emerging wave is the stationary expression

$$\rho_\phi(\xi,\eta) = \exp\left(-\xi^2/r_o^2 - \eta^2/(\beta r_o)^2\right)$$

as before, ignoring the horizontal variation in $f(x,y,z)$.

Let us assume for the function f the form

$$f(x,y,z) = K \exp\left\{-(z - z_m)^2/H^2 + \left[(x - x_m)^2 + (y - y_m - z \operatorname{ctn} \delta)^2\right]\Big/ R^2 \right\}$$

$$; \quad z_{min} \leq z \leq z_{max} \qquad (5.3)$$

This peculiar-appearing form attempts to match the falloff in electron density variance due to the effects of the ionospheric heater beamshape. Because the heater beam is circular, f has circular symmetry in each horizontal plane z = constant . However, because the "blobs" of electron density become extended along the magnetic field, the locus of centers of symmetry for various values of z is a line parallel to the magnetic field. At each altitude z , the center of symmetry is displaced (x_m, y_m) from the point of intersection of the magnetic field line passing through the origin with the constant altitude plane. The scale distance for 1/e falloff in each horizontal plane is R ; the scale distance for vertical 1/e falloff is H . The contour of constant variance--say 1/e--is an ellipsoid with circular horizontal sections. Figure 5.2 illustrates the 1/e ellipsoid for $H << R$ in the observer's coordinate system. In general the ellipsoid could be chopped off at the ends by the $z = z_{max}$ or $z = z_{min}$ planes. For the case $H \to \infty$ the ellipsoid degenerates to a cylinder having a circular horizontal cross section, skewed along the field lines and truncated by the $z = z_{min}$ and $z = z_{max}$ planes.

Given the form (5.3) for $f(x,y,z)$, the integral in Eq. (5.2) can be evaluated. The result is

$$\phi_o^2 \quad \cong .5\pi r_e^2 \lambda^2 \alpha r_o \beta^{-1} (\sec i) K A^{-1/2} \exp(-C + B^2/4A)$$

$$\times \left\{ \operatorname{erf}\left[A^{1/2}(z_{max} + B/2A)\right] - \operatorname{erf}\left[A^{1/2}(z_{min} + B/2a)\right] \right\}$$

(5.4)

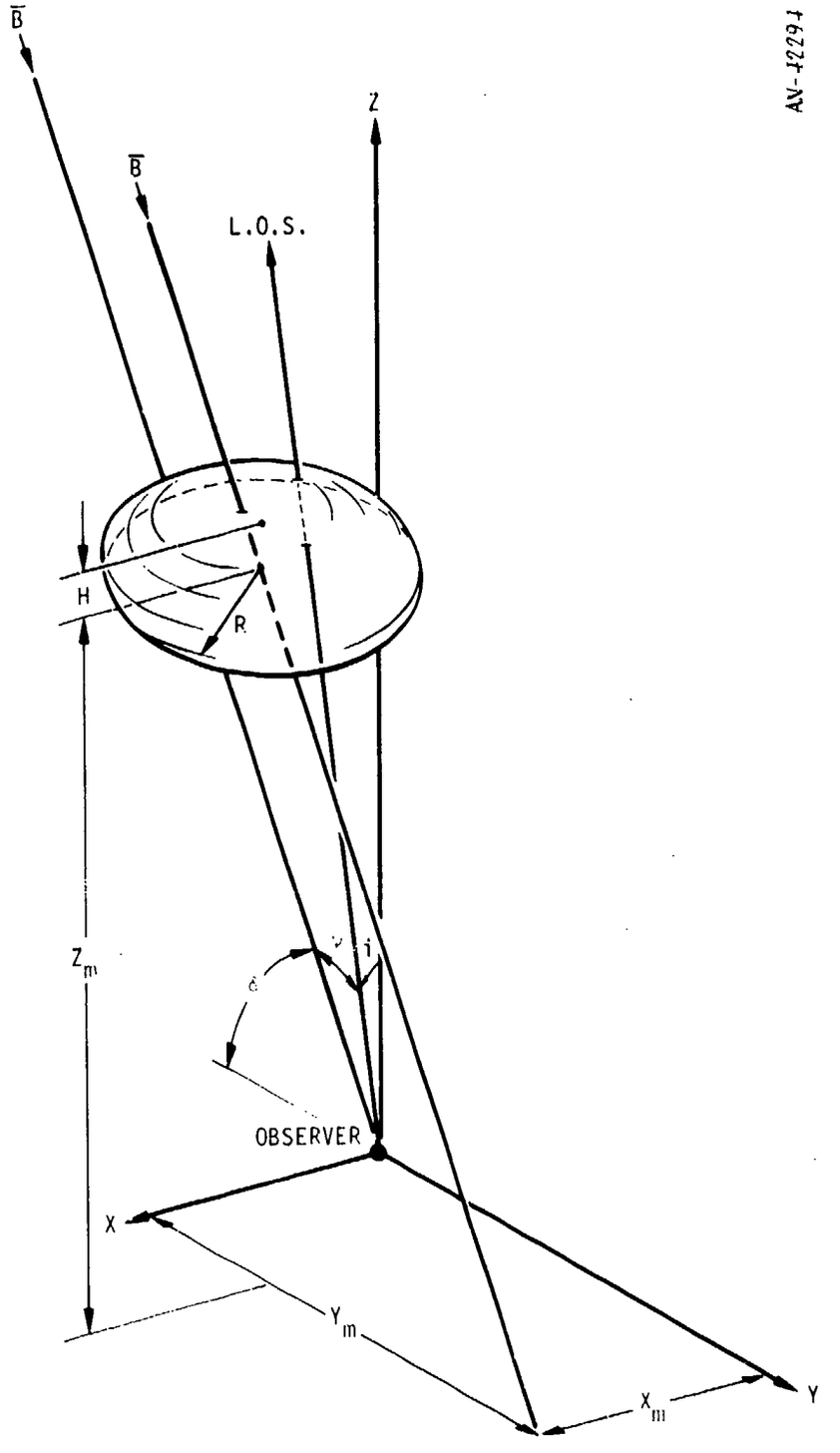

AV-4229-1

Figure 5.2. 1/e Contour of Electron Density Variance in Heated Region

where

$$A = \left[x_S^2 + (y_S + z_S \operatorname{ctn}\delta)^2\right] / \left(z_S^2 R^2\right) + 1/H^2 \tag{5.5}$$

$$B = -2\left\{\left[x_m x_S + y_m (y_S + z_S \operatorname{ctn}\delta)\right] / \left(z_S^2 R^2\right) + z_m / H^2\right\} \tag{5.6}$$

$$C = \left(x_m^2 + y_m^2\right)/R^2 + z_m^2/H^2 \tag{5.7}$$

This expression can be shown to reduce to the Briggs and Parkin formula in the case $R \to \infty$ and $H \to \infty$, or equivalently, as the horizontal and vertical variation is eliminated.

Equation 5.4 can be recast using the relation $(f_o F_2)^2 = N_m e^2 r_e / \pi$ as before to yield

$$\phi_o^2 = \frac{\pi^3}{2\lambda^2} (f_o F_2 / f)^4 \alpha r_o \beta^{-1} (\sec i) \left[E\left(\Delta N_{max}^2\right)/N_m^2\right]$$

$$\times A^{-1/2} \exp(-C + B^2/4A)$$

$$\times \left\{\operatorname{erf}\left[A^{1/2}(z_{max} + B/2A)\right] - \operatorname{erf}\left[A^{1/2}(z_{min} + B/2A)\right]\right\} \tag{5.8}$$

where $E\left(\Delta N_{max}^2\right)$ is equal to K in Eq. 5.4 or to the peak mean square deviation at the center of the heated region.

It is frequently convenient to estimate the maximum phase deviation that could be introduced along a line-of-sight through the disturbed region. That maximum occurs for a line-of-sight parallel to the magnetic

field line directly through the center of the region. In that case we have

$$x_m = y_m = 0$$

$$x_S = 0$$

$$y_S = -z_S \operatorname{ctn} \delta$$

$$\psi = 0$$

$$\beta = \alpha$$

$$A = 1/H^2$$

$$B = -2z_m/H^2$$

$$C = z_m^2/H^2$$

If we assume $z_{max} \to \infty$ and $z_{min} \to -\infty$, we have:

$$\phi_o^2 = \frac{\pi^3}{\lambda^2}\left(\frac{f_o F_2}{f}\right)^4 r_o H(\sec i) E\left(\frac{\Delta N_{max}^2}{N_m^2}\right) \qquad (5.9)$$

5.2 COMPARISON WITH BRIGGS AND PARKIN FORMULA

Some example cases were computed to compare the scintillation predicted by the modified theory with that predicted by the Briggs and Parkin formula. Figure 5.3 illustrates the angular dependence in the magnetic N-S plane for three cases: $R = \infty$, $H = \infty$ (no variation, Briggs and Parkin case); $R = 50$ km, $H = \infty$ (no vertical variation); $R = H = 50$ km (both horizontal and vertical variation). The center of the heated region was assumed to lie directly up the magnetic field line from the observer (that is, $x_m = y_m = 0$). The falloff with angle for the finite region is clearly much more rapid than for the Briggs and Parkin case. Also, the peak scintillation index is smaller when vertical variation in the electron density fluctuation is included. Figure 5.4 illustrates the varied rate of falloff from the peak for various values of the 1/e radius R;

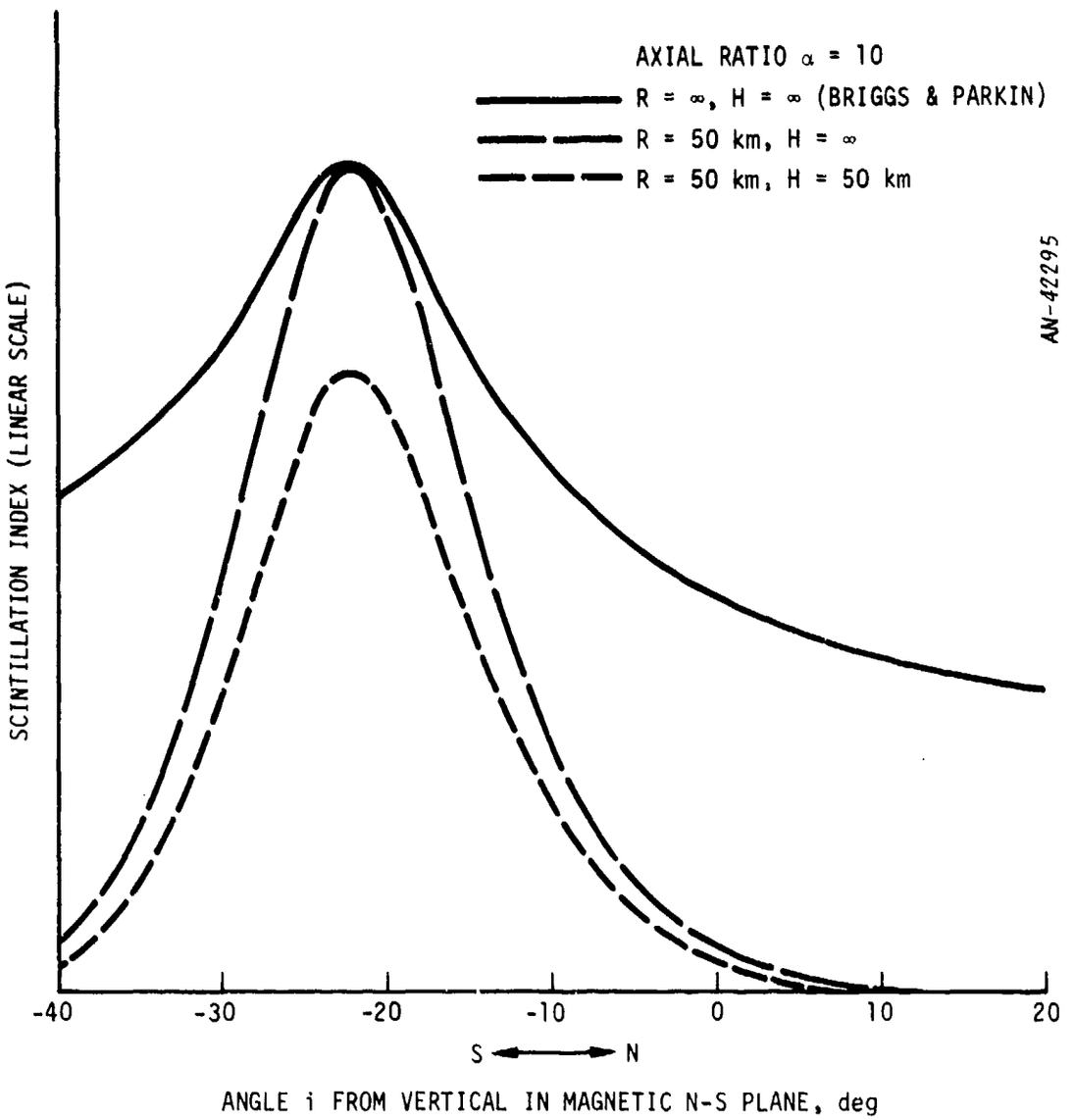

Figure 5.3. Angle Variation of Scintillation Index Using Modified Theory

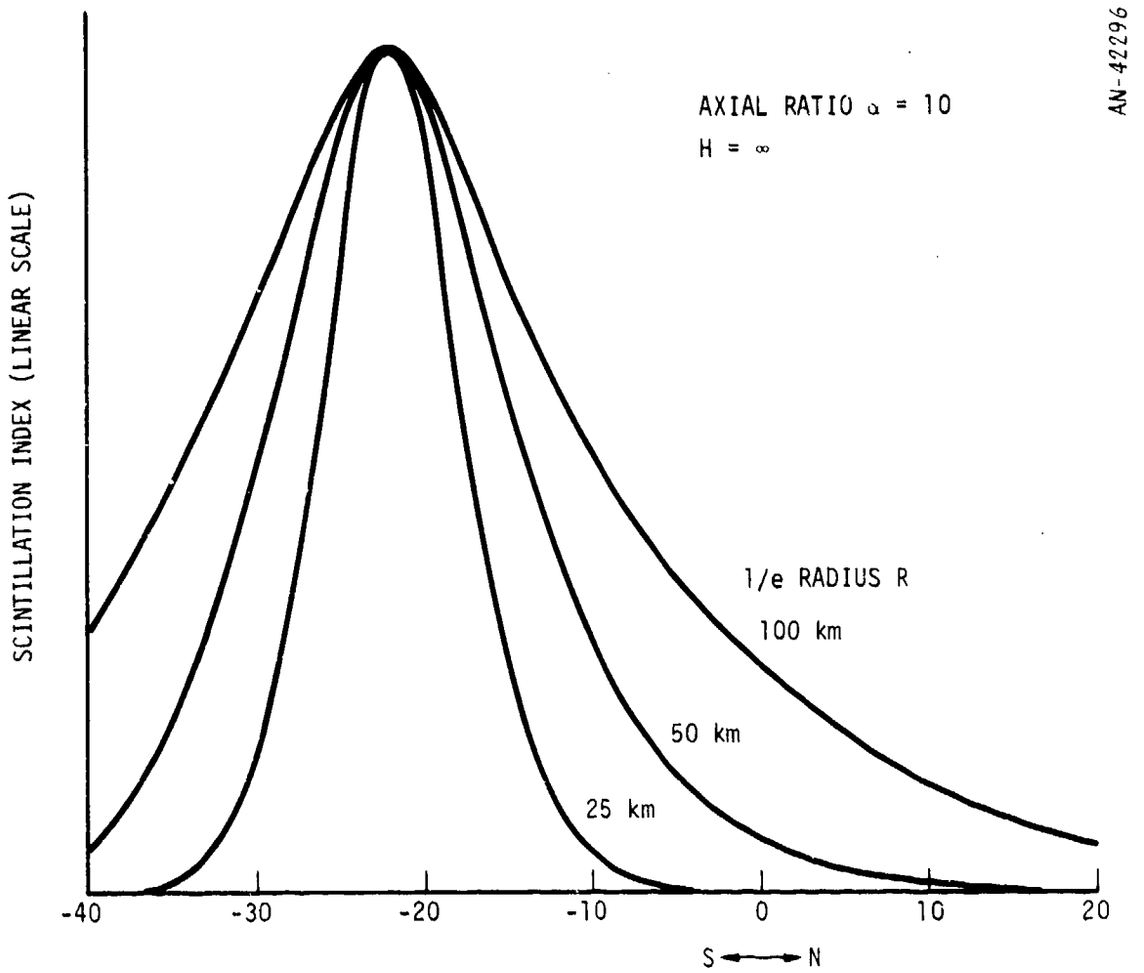

Figure 5.4. Effect of Varied 1/e Radius R

the vertical variation is suppressed ($H = \infty$) since it mainly affects the peak value and not the shape of the curve.

The effect of moving the center of the heated region away from the direct upfield point is illustrated in Fig. 5.5. The peak scintillation index is depressed and the peak occurs at a higher angle for northward shift y_m. A shift of y_m kilometers means that the observer would have to move northward y_m kilometers to view the center of the heated region directly along a magnetic field line.

5.3 PARAMETERS FOR THE MODEL

Now that we have a model (Eq. 5.8) for computing the phase variance along any line-of-sight as well as rules for relating that variance to the scintillation index (Eq. 3.11), we lack only means for determining the appropriate parameter values to use in the model.

The Aeronomy Corporation experiments have provided estimated values for the scale size r_o and axial ratio α. Figure 4.3 illustrates the observed range of values for r_o, with the most frequently observed value being about 100 meters. This is considerably smaller than the range from 300 to 900 meters for the transverse scale size in the natural ionosphere. The axial ratio α is about 10 for either the artificially modified ionosphere or the natural ionosphere.

The signal frequency f and the corresponding wavelength λ are presumed to be known. The critical frequency varies continually, usually in the range 5 to 10 MHz. For simple calculations, we can assume that $f_oF_2 \simeq 7.5$ MHz.

The remaining parameters of the model describe the variance in electron density in the region, the size and shape of the region, and its location relative to the observer.

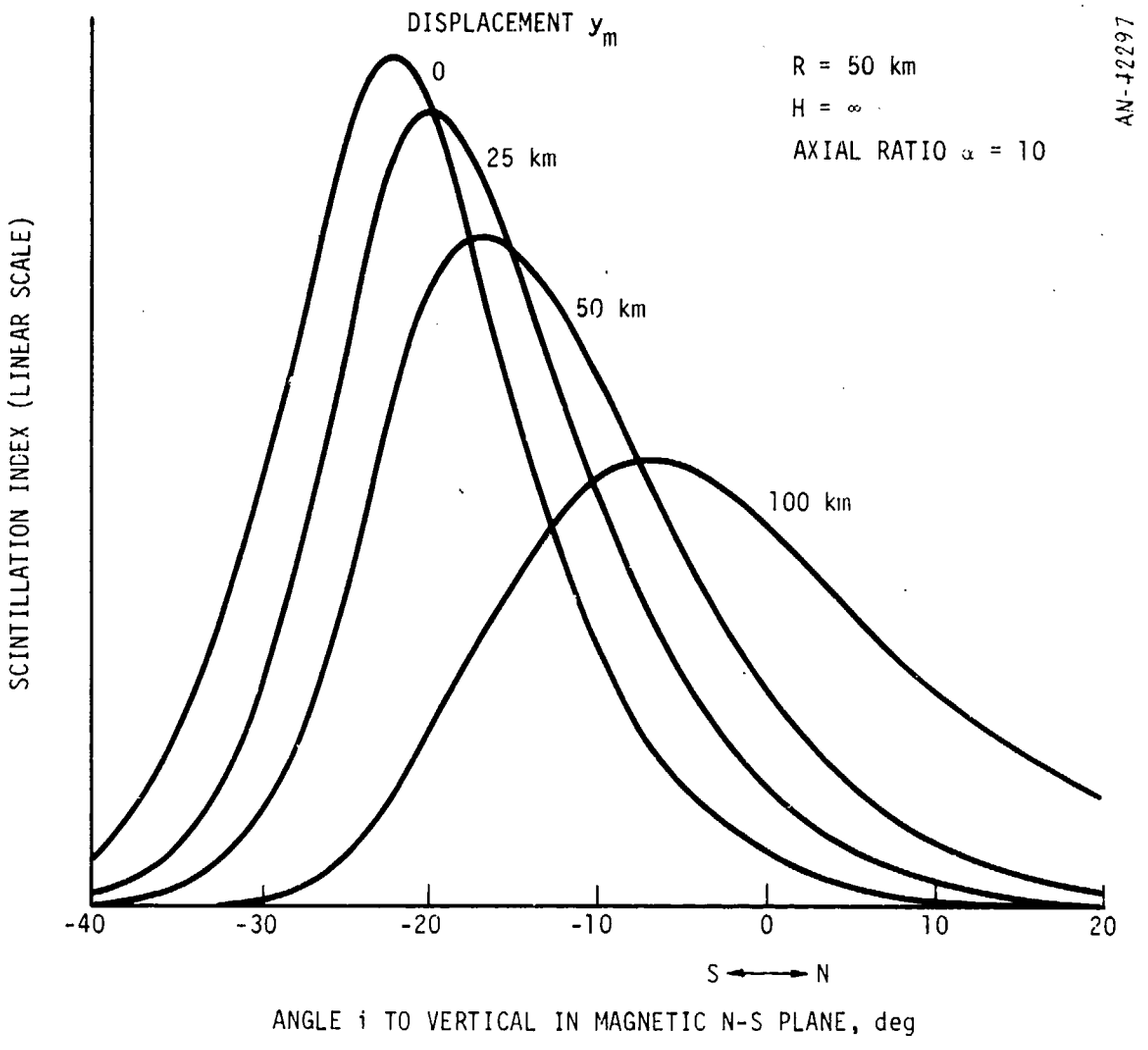

Figure 5.5. Effect of Northward Displacement y_m of Center of Heated Region

A simple model for predicting the dimensions and peak electron density deviation in the heated region was given by Pendyala and Thome[23] on the basis of their RF backscatter measurements. According to their model, the peak electron density variance occurs at the center of the heater beam at an interaction altitude z_m for which the heater frequency equals the local plasma frequency. (Typically this interaction altitude is of the order of 225 to 275 km.) The peak relative electron density variance $E\left(\Delta N_{max}^2/N_m^2\right)$ is given by

$$E\left(\Delta N_{max}^2/N_m^2\right) = 10^6 P^2/9 \tag{5.10}$$

where P is the peak power density (in W/m^2) in the heater beam at the interaction altitude. On the basis of their RF scattering measurements, Pendyala and Thome reported a saturation level of about 10^{-4} corresponding to $P = 3 \times 10^{-5} W/m^2$. No similar saturation effect was observed in the scintillation measurements. However, agreement with the square law power dependence of $E\left(\Delta N_{max}^2/N_m^2\right)$, or equivalently, linear variation of scintillation index with power, was reported by Aeronomy Corporation in PRAIRIE SMOKE IV.[20] For purposes of our model, we shall ignore the saturation effect, but values much larger than 10^{-4} will be viewed somewhat suspiciously.

The vertical extent of the heated region is assumed to be very small, with about 15 kilometers between vertical 1/e altitudes; this corresponds to $H = 7.5$ km in Eq. 5.3. With such rapid vertical variation, the exact values for z_{min} and z_{max} are not very important. We can assume values of 200 and 350 km, respectively; these values effectively correspond to $-\infty$ and $+\infty$, and these latter values could be used in the formulas with negligible difference.

If we assume a Gaussian shape for the heater main beam, we can compute the horizontal scale distance R for the heated region. Suppose

the relative power pattern for the heater beam is given by $P(\theta) \propto \exp\left(-\theta^2/\theta_e^2\right)$, where θ is the angle off vertical and θ_e is the angle at which the power is down to $1/e$ of the peak value ($\theta_e \approx 0.6 \times 3$ dB beamwidth). In the plane of the interaction altitude z_m, the angle off vertical is $\theta = \tan^{-1}\left(\sqrt{x^2 + y^2}/z_m\right) \approx \sqrt{x^2 + y^2}/z_m$ for small angles. Then in the interaction altitude plane we have

$$P \propto \exp\left[-\frac{(x^2 + y^2)}{z_m^2 \theta_e^2}\right]$$

Since the electron density variance is proportional to P^2, we find

$$E\left(\Delta N_{max}^2/N_m^2\right) \propto \exp\left(-\frac{2(x^2 + y^2)}{z_m^2 \theta_e^2}\right) \propto \exp\left(-(x^2 + y^2)/R^2\right)$$

so that

$$R = z_m \theta_e/\sqrt{2} \tag{5.11}$$

The two remaining parameters x_m and y_m define the horizontal shift of the center of the heated region from the geomagnetic field line passing through the observation point. The heated region lies above the heater transmitter, but the center may be shifted north or south slightly by the bending of the O- or X-mode transmissions. However, since we are generally interested in cases where the observer is directly downfield from the center of the heated region, we can assume $x_m = y_m = 0$ in most cases of interest.

5.4 COMPARISON OF THE MODIFIED THEORY WITH EXPERIMENTS

Let us now compare the computed results from the refined scintillation model with some of the measured scintillation data from the satellite

experiments in PRAIRIE SMOKE III. The measurements were taken on three satellite passes on 8 September 1972. The amplitude of the satellite's 150-MHz signal was recorded on each pass at the Pine Bluffs, Wyoming, receiver site operated by Aeronomy Corporation. Concurrent measurements on the last two passes were also made at the Hillsdale site a few miles away. The amplitude scintillation index S_2 was then computed at time steps of about 5 seconds. These values, reported in Ref. 18, are replotted here in Figs. 5.6, 5.7, and 5.8 for the three satellite passes.

The angle ψ between the line-of-sight to the satellite and the geomagnetic field ranged from a minimum of about 3 to 10 degrees up to angles exceeding 90 degrees. Only the values less than about 15 degrees correspond to significant scintillation levels.

The parameter values used for the calculations are summarized in Table 5.1. Some of the assumed values were chosen as discussed in the

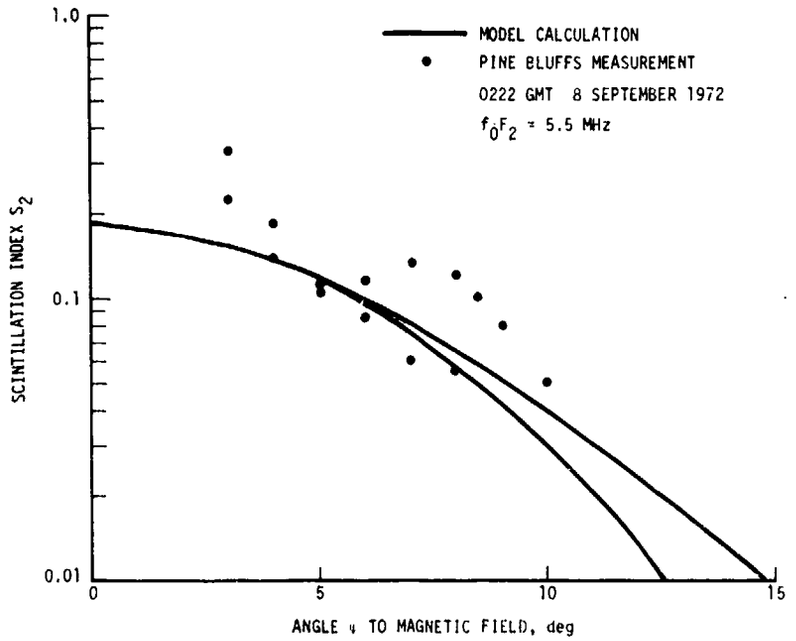

Figure 5.6. Comparison of Model with Experimental Data, Satellite Pass 1

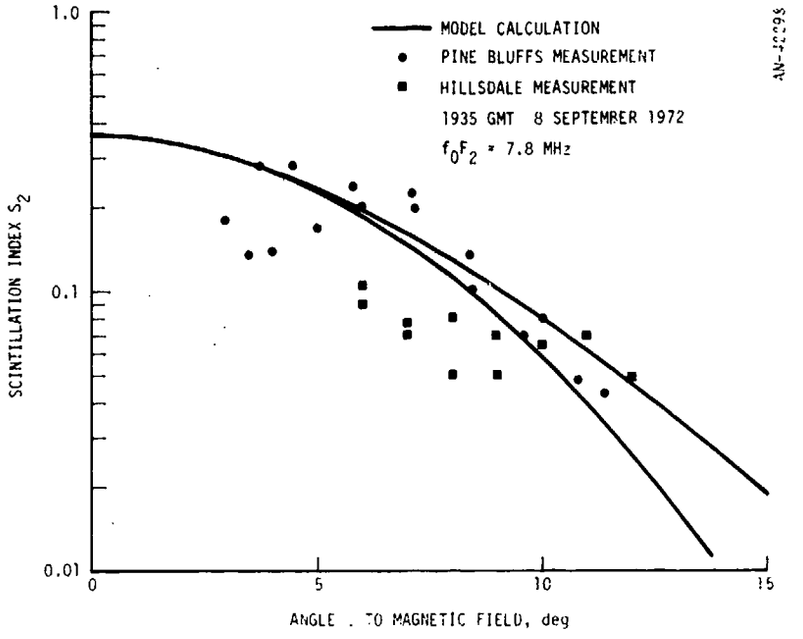

Figure 5.7. Comparison of Model with Experimental Data, Satellite Pass 2

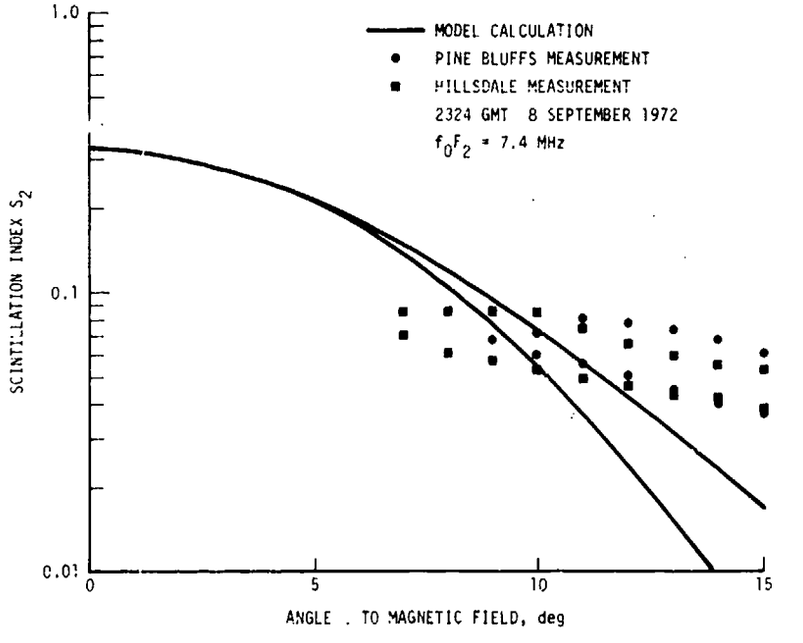

Figure 5.8. Comparison of Model with Experimental Data, Satellite Pass 3

TABLE 5.1

PARAMETER VALUES FOR MODEL CALCULATIONS
FOR PRAIRIE SMOKE III EXPERIMENTS

Parameter (Assumed or Calculated)	Value	Parameter	Value
r_o	100 m	y_m	0
α	10	Z_m	275 km
R	35 km	$E\left(\Delta N^2_{max}/N^2_m\right)$	4.8×10^{-4}
H	7.5 km	(Known or Measured)	
Z_{min}	200 km	f	150 MHz
Z_{max}	350 km	λ	2 m
x_m	0	$f_o F_2$	5.5 MHz--Pass 1 7.8 MHz--Pass 2 7.4 MHz--Pass 3

preceding section. R and $E\left(\Delta N^2_{max}/N^2_m\right)$ were computed from the known parameters of the heater transmitter--1.9 MW power, 15 dB gain, and a 16-degree half-power beamwidth--using Eqs. 5.10 and 5.11. The remaining parameters were either known beforehand or measured for each pass.

The calculations were made for lines-of-sight in the magnetic north-south vertical plane passing through the center of the heated region. The observer was assumed to lie directly downfield from the center of the region. For this case the field angle ψ goes to zero, in contrast to the actual measurements where the minimum was a few degrees. The calculations yield slightly different values for S_2 along lines-of-sight north and south of the field line because of the sec i variation in the phase variance (Eq. 5.8).

In addition to the idealized geometry, calculations were made which attempted to duplicate the actual geometry for the satellite pass. The calculations yielded minimum angles within about 1 degree of those reported for the measurements. (Actually, the field angles reported in Ref. 18 were computed, too, and not measured.) However, the scintillation indexes were negligibly different from the idealized geometry.

The agreement between the computed values and the measurements is good in Figs. 5.6 and 5.7, but rather poor in Fig. 5.8. The agreement is best for the cases where the scintillation is strong and the field angle ψ is small. These cases are clearly the ones of greatest interest in any possible systems applications. Because of the few cases available for validating the model, it should be used with some caution.

6 SCINTILLATION EFFECTS ON RADAR SYSTEMS

We have seen in the preceding sections that artificial heating of the ionosphere can produce modest levels of scintillation along lines-of-sight passing through the heated region. In addition to its use as an experimental mechanism in studying the ionosphere, artificial modification of the ionosphere could potentially be used to degrade the performance of RF systems requiring one-way or two-way lines of sight through the F-region. The two such systems that come immediately to mind are long-range radars for tracking missiles or satellites in space and satellite-to-ground (or vice versa) communication relays.

The objectives of this section, which treats the radar, and the next section, which treats satellite communication, are to identify the degradations produced by ionospheric scintillation and to relate that degradation parametrically to the scintillation index. By treating the scintillation level parametrically, we can extend many of the results to natural or nuclear-induced scintillation.

Two principal effects on radar operation are produced by scintillation. The first is a change in the detection statistics, generally a degradation of high detection probabilities and an enhancement of low detection probabilities. In Sec. 6.2 the detection probabilities for various signal-to-noise ratios are computed as a function of the scintillation index assuming a Rice distribution for the scintillation amplitude. The implications of that assumption are discussed in Sec. 6.1. The second effect is a degradation of angular tracking accuracy due to fluctuations in the angle of arrival of the radar signal. Tracking errors are evaluated using a Monte Carlo computer simulation for tracking. Some results from this simulation are presented in Sec. 6.3.

6.1 THE AMPLITUDE DISTRIBUTION FUNCTION

There is some dispute concerning the correct distribution function to use in describing the amplitude scintillations which occur in the presence of striations. Some of the alternatives are discussed in the appendix.

Mercier[11] has asserted, and other researchers (e.g., Briggs and Parkin,[2] Singleton[12]) have agreed, that the distribution in the limit of large distances from the phase screen is Rician. Mercier's result, although the derivation may not be mathematically rigorous, is intuitively satisfying as was pointed-out in Sec. 3.2. On the other hand, some later workers (see for example Rino and Fremouw[24]) have been dissatisfied with this assumption. They have found that the measured data for the normal ionosphere are not well fitted by a Rician distribution, but rather require a more complicated function based on two-dimensional Gaussian statistics in which the in-phase and quadrature components of the scattered power have unequal sigmas. See the appendix for a further discussion of this problem. Rino and Fremouw found that their data implied a transverse scale size $r_o \approx 600$ meters , and inferred that the far-field conditions under which the Rician amplitude distribution of Mercier was derived would rarely be appropriate at typical radar operating frequencies.

For the purposes of the present discussion, however, it is important to note that the artificially induced striations produced by ionospheric heating appear to have significantly smaller transverse scale sizes than those found in the natural ionosphere. A glance at Fig. 4.3 reveals that the distribution of transverse scale sizes measured in the PRAIRIF SMOKE II and IV experiments peaks at around $r_o = 100$ meters , that 50 percent of the time $r_o < 150$ meters , and that 90 percent of the time $r_o < 300$ meters . Now, Fig. 3.5 shows that far-field conditions may be assumed to apply whenever $\lambda Z_o / r_o^2 > 2$. Assuming that the phase screen is at least 300 km from the radar and that the target is far beyond the screen, it is easy to compute the maximum value of r_o for which the far-field approximations are generally valid, as a function of the radar frequency f . This has been plotted in Fig. 6.1, on the following page. It is obvious from this figure that Rino and Fremouw were correct in asserting that a ground-based receiver looking at a target near the zenith will generally not be in the far-field with respect to natural ionospheric striations with a mean transverse scale size of the order of

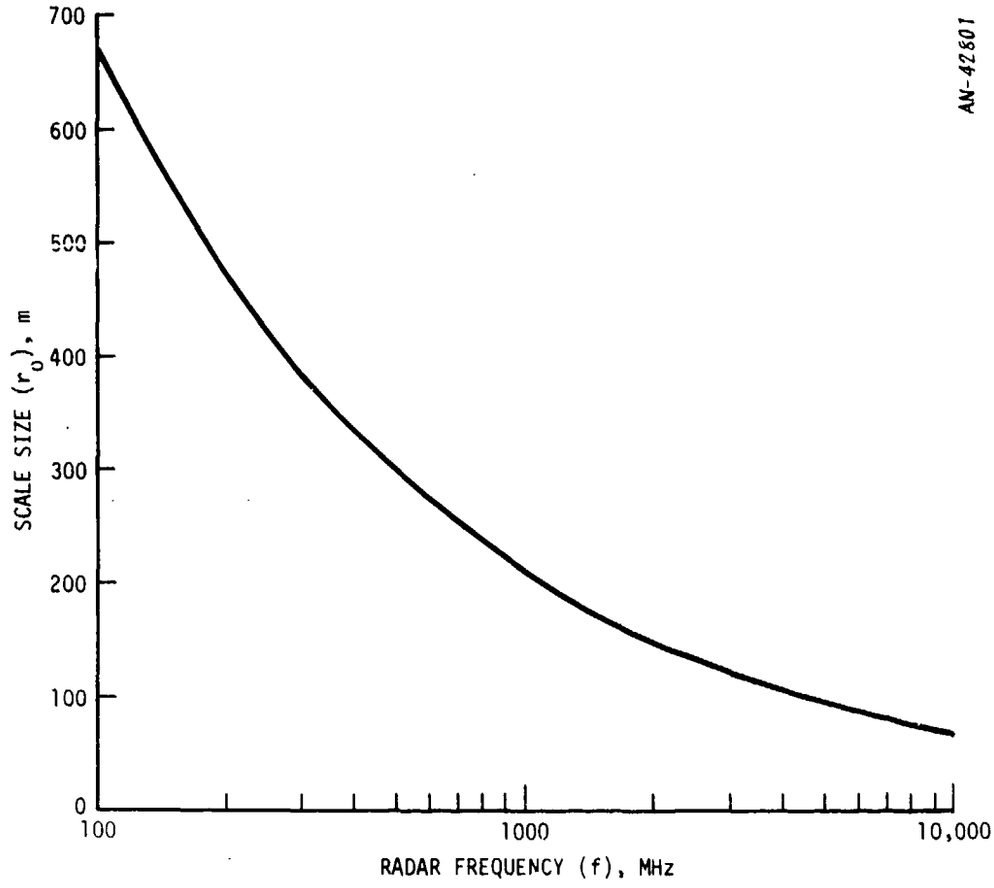

Figure 6.1. Maximum Striation Scale Size for Far-Field Approximations to be Valid

600 meters. On the other hand, it is equally obvious that a radar operating at VHF or UHF, and even at L-band or up to S-band, will generally be in the far-field with respect to the artificially induced striations.

Accordingly, for the present application it is not unreasonable to accept Mercier's hypothesis and use his Rician amplitude probability-density function. For a one-way propagation path through the phase-screen, the amplitude density function is

$$p_1(R;R_o,\beta) = \frac{2(1+\beta)}{R_o}\frac{R}{R_o}\exp\left[-(1+\beta)(R/R_o)^2 - \beta\right] I_o\left[2\sqrt{\beta(1+\beta)}\,R/R_o\right] \tag{6.1}$$

where R is the observed amplitude, R_o is the value which would have been observed in the absence of scintillations, and β is a parameter which is described below. The function $I_o(x)$ is the modified Bessel function of zero order.

The parameter β which appears in Eq. 6.1 is related to the fundamental properties of the phase screen. In Sec. 3.1 we defined the phase function $\phi(x,y)$ at the screen, and its RMS value

$$\phi_o \equiv \sqrt{E(\phi^2)}$$

We now define the parameter β to be

$$\beta \equiv \frac{e^{-\phi_o^2}}{1 - e^{-\phi_o^2}} \tag{6.2}$$

It can be shown (R.W. Hendrick[25]) that the power in the undiffracted ("specular") portion of the signal transmitted through the phase screen is proportional to $\exp\left(-\phi_o^2\right)$, and the power in the diffracted ("random") portion of the signal is proportional to $1 - \exp\left(-\phi_o^2\right)$. The parameter β therefore is equal to the ratio of the specular to random power in the received signal; it may be thought of as a kind of signal-to-noise ratio. Alternatively, it is a measure of the strength of the phase screen: a large value of β corresponds to weak diffraction and a small value of β corresponds to strong diffraction.

It is not surprising, therefore, that β is related to the scintillation indices defined in Sec. 3.2 and the appendix. From Eq. 3.6 it is easily seen that

$$S_4^2 = 1 - \left(\frac{\beta}{1+\beta}\right)^2 \tag{6.3}$$

Thereupon the known relationship between S_4 and S_2 for the Rice distribution (see Fig. A.1) can be used to compute β as a function of S_2. Figure 6.2 shows ϕ_o and β as functions of the scintillation index S_2.

For radar problems in which the signal is propagated <u>twice</u> through the phase screen, a slightly different amplitude distribution function, $p_2(R;R_o,\beta)$, must be used. This is found from p_1 by making use of the fact that the two-way distribution of R is equivalent to the one-way distribution of R^2. Standard techniques then permit derivation of the function p_2:

$$p_2(R;R_o,\beta) = \frac{1+\beta}{R_o} \exp\left[-(1+\beta)\frac{R}{R_o} - \beta\right] I_o\left[2\sqrt{\beta(1+\beta)R/R_o}\right] \tag{6.4}$$

Here again, R is the observed instantaneous value of the amplitude, and R_o is the value which would have been observed in the absence of striations. The parameter β, which characterizes the phase screen rather than the process, retains the same value whether for one-way or two-way propagation. It should be noted here that the amplitude R is related to the measured signal-to-noise ratio (S/N) in either case by the identity

$$R^2 \equiv 2(S/N) \tag{6.5}$$

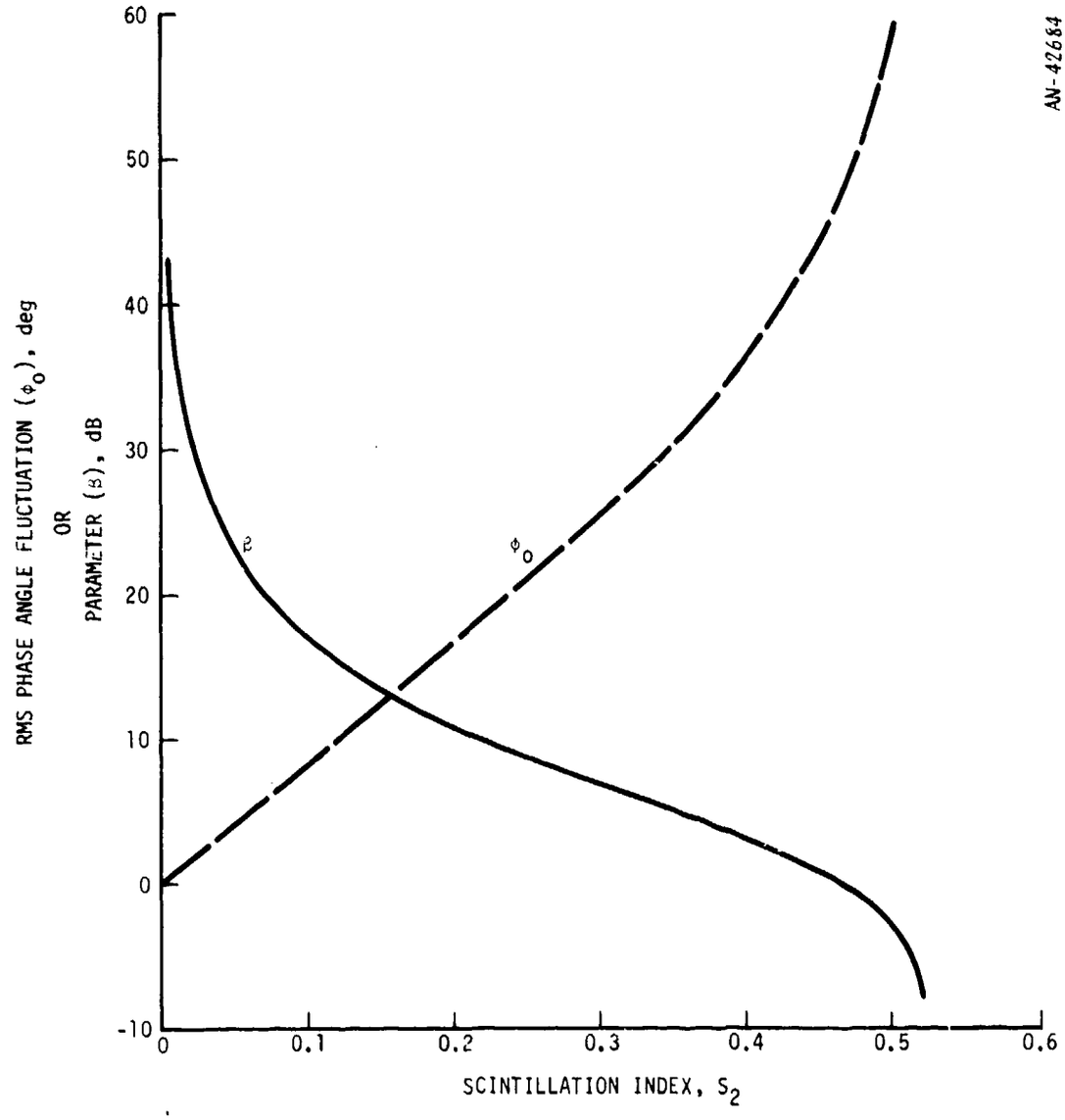

Figure 6.2. Scintillation Parameter β and RMS Phase Angle Fluctuation ϕ_o as Functions of Scintillation Index S_2

6.2 RADAR DETECTION PROBABILITY AND DETECTION RANGE

Standard radar detection theory (see for example DiFranco and Rubin,[26] especially Chapter 9) computes the detection probability for typical signal processing in the following manner. Assume a steady sinusoidal signal of known amplitude and unknown phase, added to zero-mean Gaussian noise of known power. The radar receiver performs an envelope detection and then determines the presence or absence of the signal by comparing the peak voltage of the video signal with a pre-selected threshold. The probability that the threshold will be exceeded when the signal is indeed present defines the detection probability, P_d.

The threshold level, r_b, is selected to provide a desired probability of false alarm, P_f; this is simply the probability that the random noise alone, in the absence of the signal, will produce a voltage peak which exceeds the threshold. It is of course desirable to minimize the false alarm probability, but the price that must be paid for a very low value of P_f is an increased possibility that even when the signal is present a threshold crossing will fail to occur: in other words, a reduced probability of detection. In practical radar systems a compromise must be made whereby an acceptable value of P_f is chosen; values between 10^{-4} and 10^{-8} are commonly used.

It can be shown that the probability density that the peak video amplitude will be R when the amplitude of the sinusoidal signal is R_o, is given by the Rician distribution

$$p(R,R_o) = R \exp\left[-\left(R^2 + R_o^2\right)/2\right] I_o(R_o R) \tag{6.6}$$

Here R and R_o are normalized to the noise voltage, so R is given by Eq. 6.5 and

$$R_o^2 \equiv 2(S/N)_o \tag{6.7}$$

where $(S/N)_o$ is the known signal-to-noise ratio for the steady input sinusoidal signal. This represents the case of a target whose cross section is intrinsically non-fluctuating.

For a given false alarm probability, the amplitude threshold level must be defined by requiring that

$$P_f = \int_{r_b}^{\infty} p(R,0)\ dR$$

which leads at once to the expression

$$r_b = \sqrt{-2\ \ell n P_f} \tag{6.8}$$

Having set the threshold accordingly, the detection probability then becomes

$$P_d = \int_{r_b}^{\infty} p(R,R_o)\ dR \tag{6.9}$$

If the sinusoidal signal amplitude is not constant, but fluctuates either because the target cross-section fluctuates or because the propagation medium induces scintillations (or both), then the detection probability must be computed by multiplying Eq. 6.9 by the amplitude probability density distribution $f(R_o)$ and integrating overall values of R_o, i.e.,

$$P_d = \int_{o}^{\infty}\int_{r_b}^{\infty} p(R,R_o')f(R_o')\ dR\ dR_o' \tag{6.10}$$

We consider the case of a non-fluctuating target but a propagation medium which contains a phase screen consisting of a layer of striations that causes amplitude scintillations. For a two-way path through this medium the amplitude scintillations have a distribution function of the form of p_2 as given by Eq. 6.4. Thus

$$P_d(R_o,\beta) = \int_o^\infty \int_{r_b}^\infty p(R,R_o')p_2(R_o';R_o,\beta)\, dR\, dR_o' \tag{6.11}$$

This expression has been evaluated as a function of scintillation index S_2 (through the parameter β) and vacuum signal-to-noise ratio $(S/N)_o$ (through the parameter R_o) for several typical values of the false alarm probability P_f. Some of these results are shown in Figs. 6.3 and 6.4: Fig. 6.3 for $P_f = 10^{-4}$ and Fig. 6.4 for $P_f = 10^{-8}$. Notice that the scintillations tend to <u>increase</u> the detection probability for targets of low signal-to-noise ratio but to <u>decrease</u> the detection probability when the signal-to-noise ratio is large. A similar effect has long been observed for cases of fluctuating targets in a neutral environment.

These results can be used to compute degradation factors which indicate how the scintillations reduce the range at which a radar can achieve a given detection probability on any target. The degradation factors can be expressed in a form which is independent of the target or its signal-to-noise ratio, but which depends only on S_2, P_d, and P_f.

We start with the standard radar equation in the form

$$S/N = (S/N)_1 (R_1/R)^4 \sigma/\sigma_1 \tag{6.12}$$

where here

S/N is the measured signal-to-noise ratio

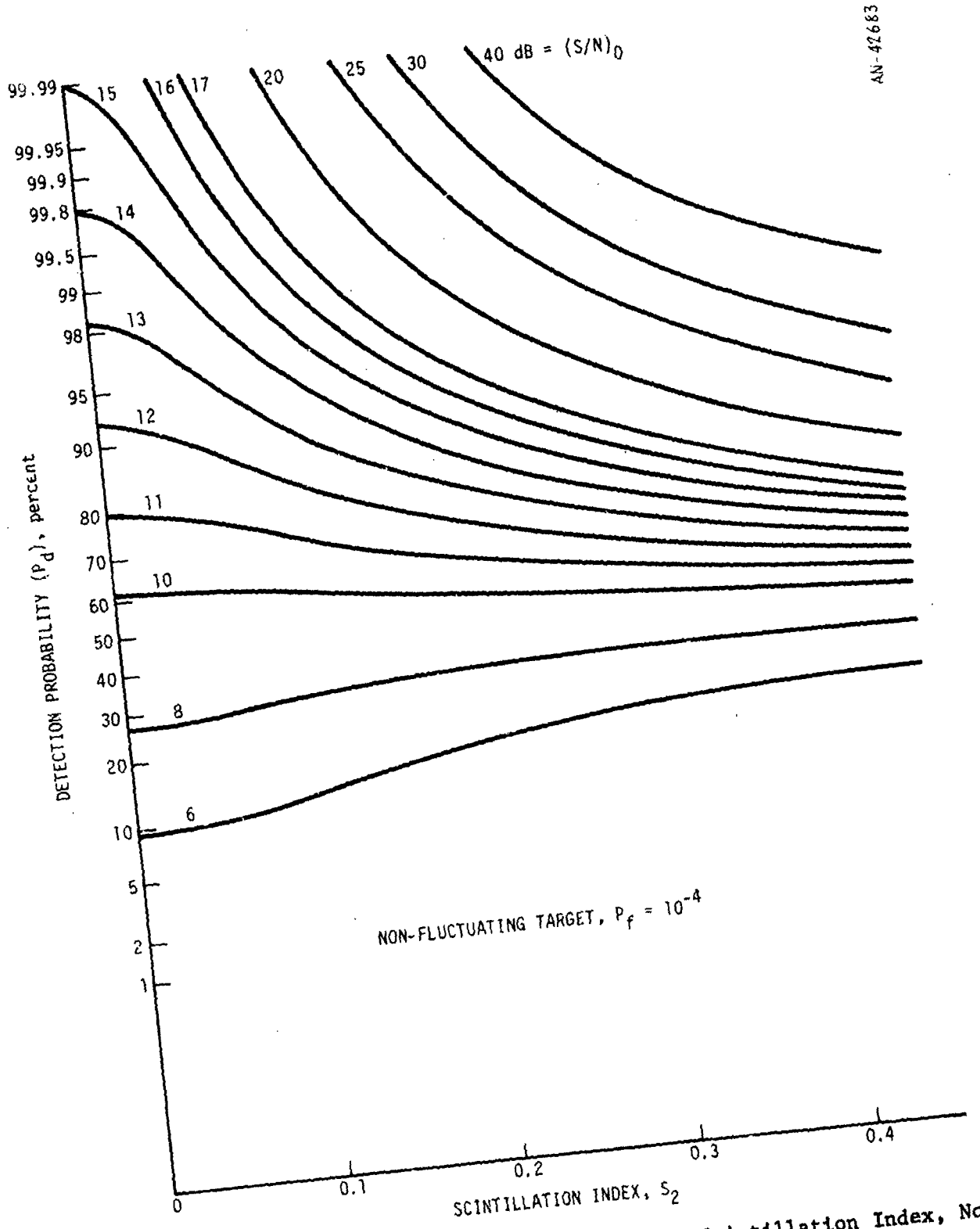

Figure 6.3. Radar Detection Probability Versus Scintillation Index, Non-Fluctuating Target, $P_f = 10^{-4}$

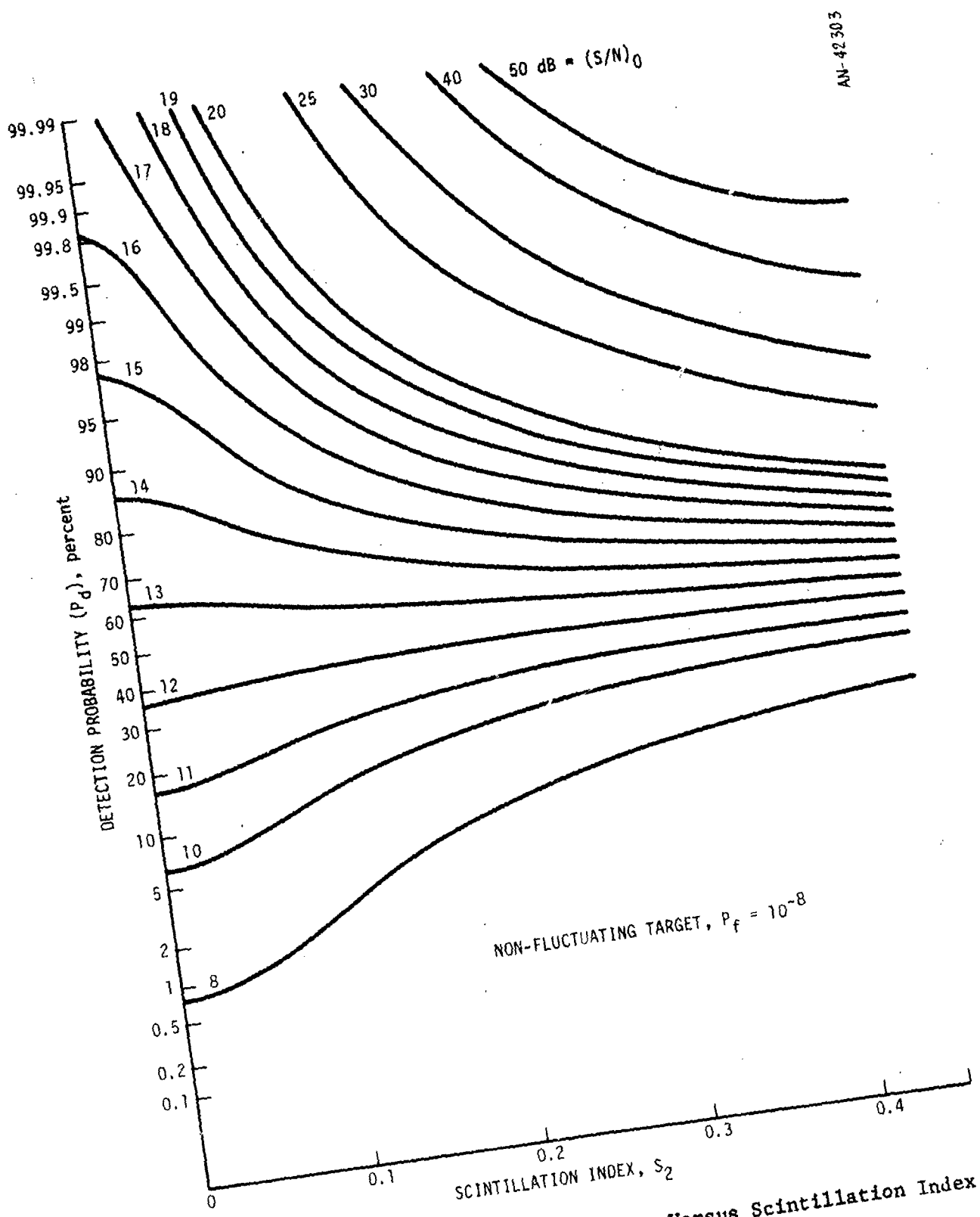

Figure 6.4. Radar Detection Probability Versus Scintillation Index, Non-Fluctuating Target, $P_f = 10^{-8}$

$(S/N)_1$ is the minimum signal-to-noise ratio required for detection by the given radar

R_1 is the range at which a target of cross-section σ_1 will just produce this minimum signal-to-noise ratio

R is the current range to the target,*

σ is the current cross-section of the target

The parameters $(S/N)_1$, R_1, and σ_1 are given or may be computed from other intrinsic parameters defining a specific radar.

Now, in the absence of striations ("vacuum") it is possible to compute the minimum signal-to-noise ratio, $(S/N)_o$, which is required to assure a specified detection probability, P_d, with a given false alarm probability P_f. Curves like those in Figs. 6.3 and 6.4 can be used to find $(S/N)_o$. Then, for a target of known cross section, the radar equation can be used to compute the maximum detection range,* $R_o(0)$, at which this target can be expected to be detected with probability P_d. It is given by

$$R_o(0) = \left[\frac{(S/N)_1}{(S/N)_o}\frac{\sigma}{\sigma_1}\right]^{1/4} R_1$$

When striations are present ($S_2 > 0$), the signal-to-noise ratio required to achieve the same detection probability will be changed to $(S/N)_o'$ which, as we have seen, may be larger or smaller than $(S/N)_o$. Similarly, the detection range will be changed to

$$R_o(S_2) = \left[\frac{(S/N)_1}{(S/N)_o'}\frac{\sigma}{\sigma_1}\right]^{1/4} R_1$$

*There should be no danger of confusing this R and R_o with the symbols R and R_o which represent signal amplitudes in other expressions.

Clearly, therefore, the ratio of the detection ranges with and without the scintillations is

$$\frac{R_o(S_2)}{R_o(0)} = \left[\frac{(S/N)_o}{(S/N)'_o}\right]^{1/4} \tag{6.13}$$

and is independent of the specific parameters which describe the radar or the target.

In this manner we have computed the degradation factor, the ratio $R_o(S_2)/R_o(0)$, as a function of S_2 for selected values of P_d and for three values of P_f : 10^{-4}, 10^{-6}, and 10^{-8}. The results are shown plotted in Figs. 6.5, 6.6, and 6.7, respectively.

It is clear from these results that a radar can suffer severe degradation of its single-pulse detection range on a non-fluctuating target when the intervening medium has a scintillation index S_2 greater than about 0.3. The results remain the same for multiple-pulse detection provided that the integration period is less than the scintillation correlation time. For fluctuating targets, or for multi-pulse detection when the integration period is greater than the scintillation correlation time, one would expect in general that the degradation would be less significant than that found above, but the specific results would depend on the statistics for the case of a fluctuating target.

6.3 RADAR TRACKING

When a radar tracks a target which passes behind a striated region, the scintillations cause tracking errors which increase the prediction error at the intercept point. Although the details are somewhat dependent on the specific scenario, it is possible to express the results in a form which is relatively scenario insensitive, and to parameterize some of the intrinsic variables. This is what we shall do in the following pages.

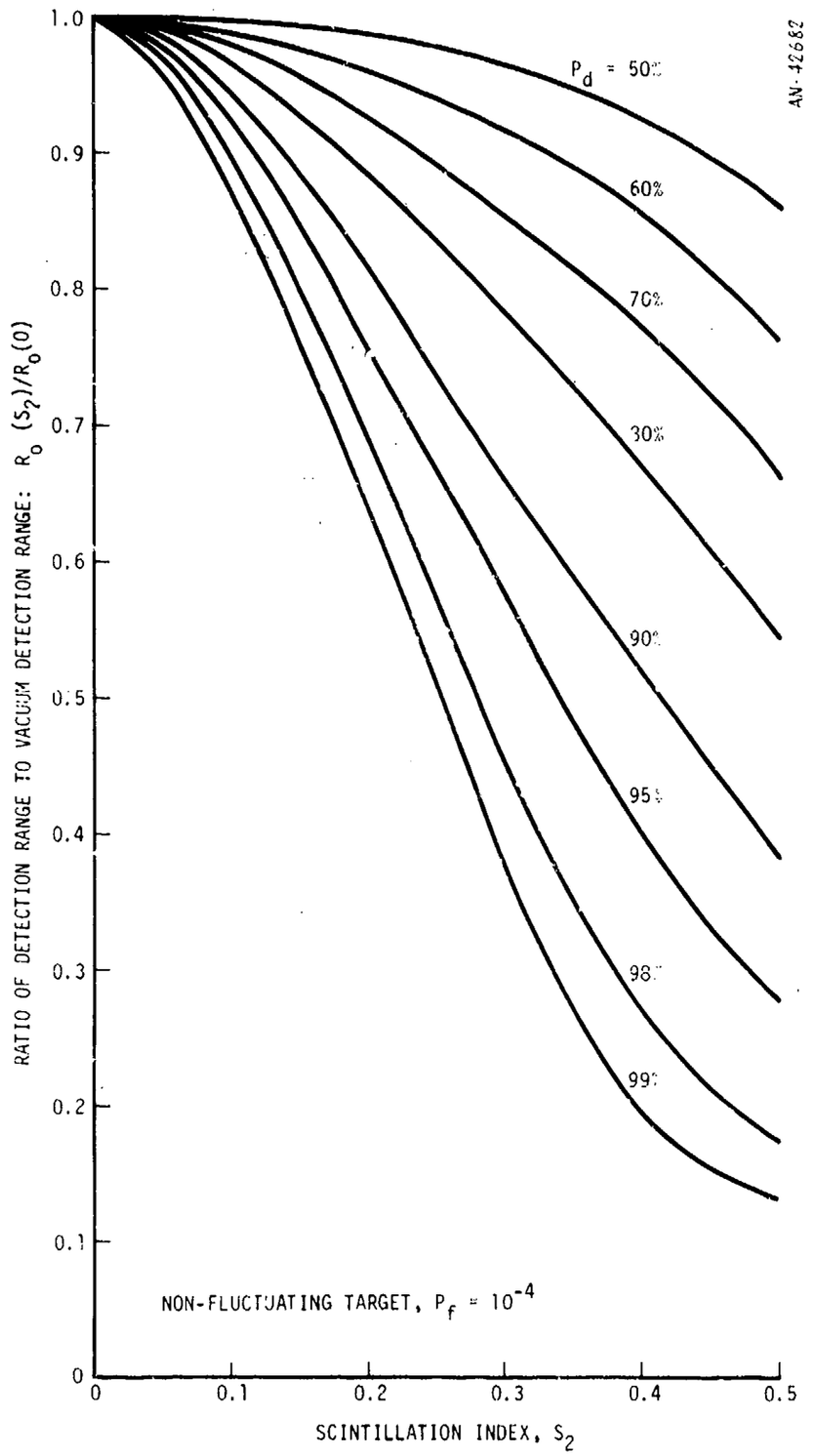

Figure 6.5. Ratio of Detection Range to Vacuum Detection Range as Function of Scintillation Index, for Non-Fluctuating Target and $P_f = 10^{-4}$.

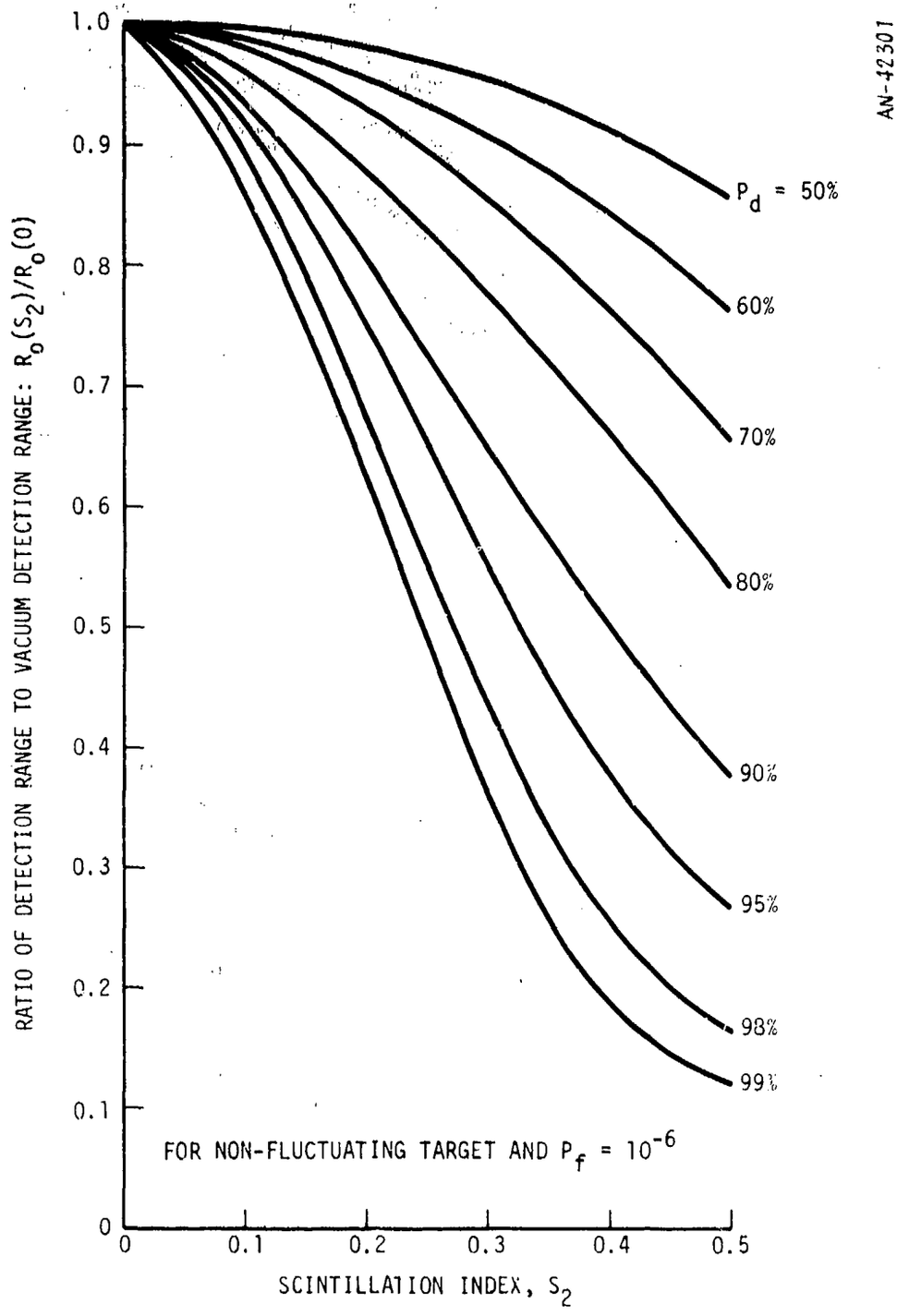

Figure 6.6. Ratio of Detection Range to Vacuum Detection Range as Function of Scintillation Index, for Non-Fluctuating Target and $P_f = 10^{-6}$.

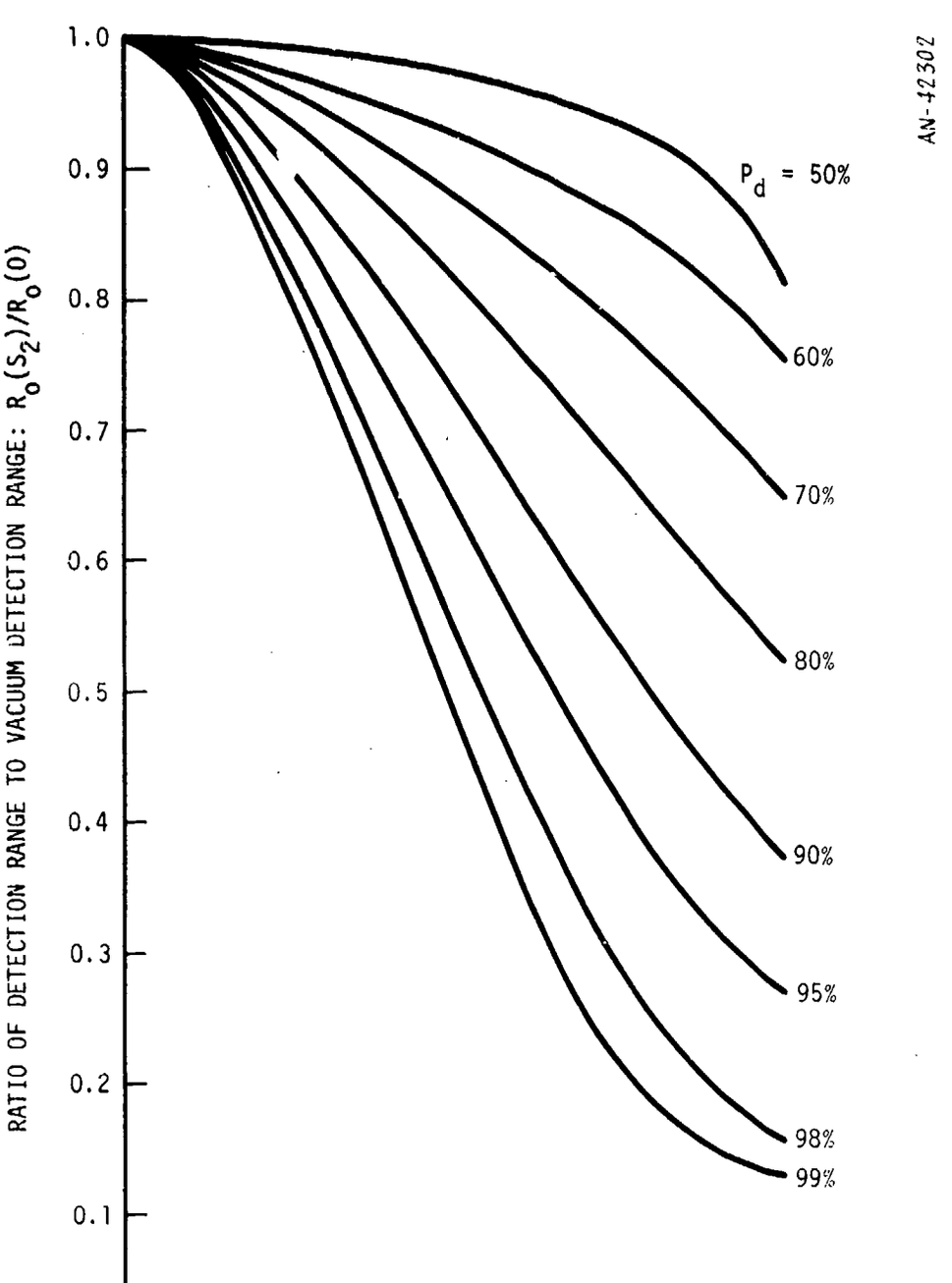

Figure 6.7. Ratio of Detection Range to Vacuum Detection Range as Function of Scintillation Index, for Non-Fluctuating Target and $P_f = 10^{-8}$

The scintillations which affect the tracking results are of two kinds: amplitude scintillations such as we have already discussed, and angle scintillations which will be described below. These cannot be separated in the analysis because the amplitude scintillations cause changes in the natural radar errors in range and angle in addition to their effect on detection range.

6.3.1 Radar Errors as Influenced by Amplitude Scintillations

A radar usually measures three coordinates of the target at each pulse: the range (R), and two angular coordinates, the azimuth (A) and the elevation (E), or sine-space coordinates (u,v). In any measurement of R,A,E , the radar will make unavoidable errors. In addition to bias errors, which by definition are constant and unknown during any given track, there are stochastic errors whose statistics at least are known. The statistical parameters can usually be expressed in a form which exhibits the fact that they have a part which is independent of the signal-to-noise ratio and another part which is signal-to-noise dependent. Thus, we write that any measurement of the parameter X (where X may be R, A, or E) has a zero-mean Gaussian error of standard deviation σ_x , where

$$\sigma_x^2 = A_x^2 + \frac{B_x^2}{(S/N)} \tag{6.14}$$

The six coefficients (A_x, B_x) are known from the calibration measurements performed on any given radar. Approximate but reasonably accurate values for (A_x, B_x) can also be computed from the known parameters of the radar antenna and waveform.

When tracking a target in "vacuum," the signal-to-noise ratio is given by the radar equation as a function of the target and radar parameters and the range to the target at any given time. Thus the variances σ_x^2 can be estimated and used in the tracking logic, but the random measurement errors for each pulse are not known; this leads to inescapable

tracking errors and an eventual target prediction error whose statistics are often estimated by performing a Monte-Carlo simulation of the tracking process.

When striations are present along the radar line-of-sight, the value of (S/N) is itself a random variable whose statistics are given by Eqs. 6.4 through 6.6. In this case the only way to ascertain the eventual target prediction error is to perform the Monte-Carlo calculation using samples drawn randomly from the appropriate distributions. The algorithm by which this has been done in the present investigation will be discussed in Sec. 6.3.3 below.

6.3.2 Angular Scintillations

In addition to the "normal" angular errors described by Eq. 6.14, the presence of an intervening striated region also induces fluctuations in the angle-of-arrival of the radar returns as measured at the receiver. Representing the striated region as a phase screen again, and assuming that far-field conditions are applicable, the angular scintillations may be described by a zero-mean Gaussian distribution about the "vacuum" angle, with variance

$$\sigma_\theta^2 = 2(\lambda/2\pi r_o)^2 \phi_o^2 \qquad (6.15)$$

By making use of Eq. 3.6 and the fact that $S_4 \simeq 2S_2$ (see the appendix), we can write

$$\phi_o^2 \simeq 2S_2^2[1 + 2S_2^2]$$

an approximation which upon comparison with Fig. 6.2 is seen to be very good on the range $0 \leq S_2 \lesssim 0.45$ and adequate out to $S_2 \simeq 0.5$. Substituting this into Eq. 6.15 leads to the expression

$$\sigma_\theta \simeq \frac{S_2\sqrt{1 + 2S_2^2}}{\pi(r_o/\lambda)} \qquad (6.16)$$

Since the striations are assumed to be elongated along the magnetic field lines, with a "longitudinal" scale size much greater than r_o, it must be recognized that the angular scintillations characterized by σ_θ occur only in the direction normal to both the radar line-of-sight and the magnetic field lines in the region of the phase screen. Any scintillations parallel to the field lines would be of negligible magnitude, and will be ignored in the present analysis. Accordingly, the angular scintillations are characterized by their standard deviation, σ_θ, and their direction, μ, in the radar viewing plane normal to the line-of-sight. (Numerical values of σ_θ are given later in Fig. 6.11.)

6.3.3 The Monte-Carlo Tracking Simulation

In order to evaluate the effects of both amplitude and angle scintillations on the radar tracking function, a Monte-Carlo tracking simulation program was written. This program accepted a given target trajectory and specified radar parameters. It placed a heated patch (striated region) of appropriate size, shape, and altitude at a specified location with respect to the trajectory, so as to interfere with part of the tracking; it was geometrically impossible to interfere with the entire track using only one patch.

The program simulated the tracking process by using a random number generator in conjunction with the known statistical properties where required to represent the noise, radar errors, and scintillation effects. In order to avoid extraneous issues, a perfect tracking filter was assumed. After making tracking measurements for a specified time period at a given tracking rate, using the data corrupted by the effects previously described, the program projected the calculated trajectory forward in time to a specified time or altitude (as desired) and estimated the target location.

This was compared with the true target position at this time to yield the prediction error, D. The above tracking and projection procedure was repeated a given number of times, using different random numbers at each iteration, and the results were accumulated to produce the mean error, $\bar{D}$, and its standard deviation, σ_D. The entire procedure could be carried out for a range of input values of the parameters S_2, r_o/λ, and μ.

A flow chart for this program is shown in Fig. 6.8.

6.3.4 The Baseline Parameters

In using the Monte-Carlo Tracking Simulation program, specific scenarios had to be used. There was no way to avoid choosing particular trajectories and radar parameters for each calculation. However, the results have been expressed in a relative form which is intended to reduce the specific scenario dependence; in addition several of the most significant parameters were separately varied over their natural range to evaluate their individual effects on the results. It is hoped that this form of analysis will provide a picture of the tracking effects due to the scintillations which is relatively independent of scenario. This subject will receive additional comment in the discussion to follow.

It was intended to run a series of different trajectories and radar types through the program. Unfortunately, the program turned out to have such a long running time that it was impractical to carry out this procedure. We were able to use only one of the planned trajectories and radar locations, although we were able to study the effects of changing the radar parameters by varying some of them in separate calculations.

The trajectory covered an 8,000-km ground range, with the radar location as its intended impact point. Figure 6.9 illustrates the nature of this trajectory relative to the radar by showing the target range, elevation angle, and altitude (above the ground) as functions of the time after launch in seconds.

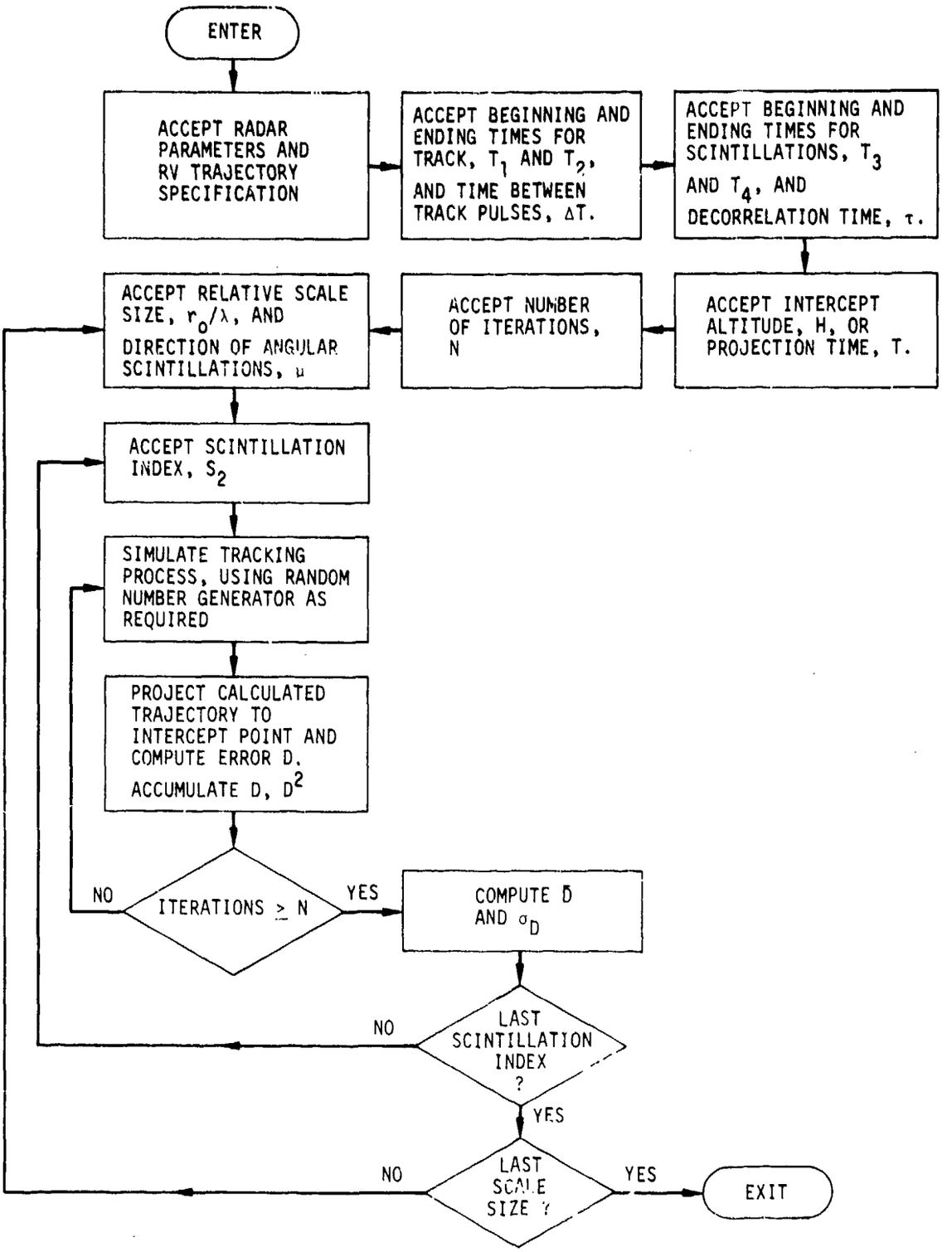

Figure 6.8. Flow Chart for Monte-Carlo Tracking Simulations

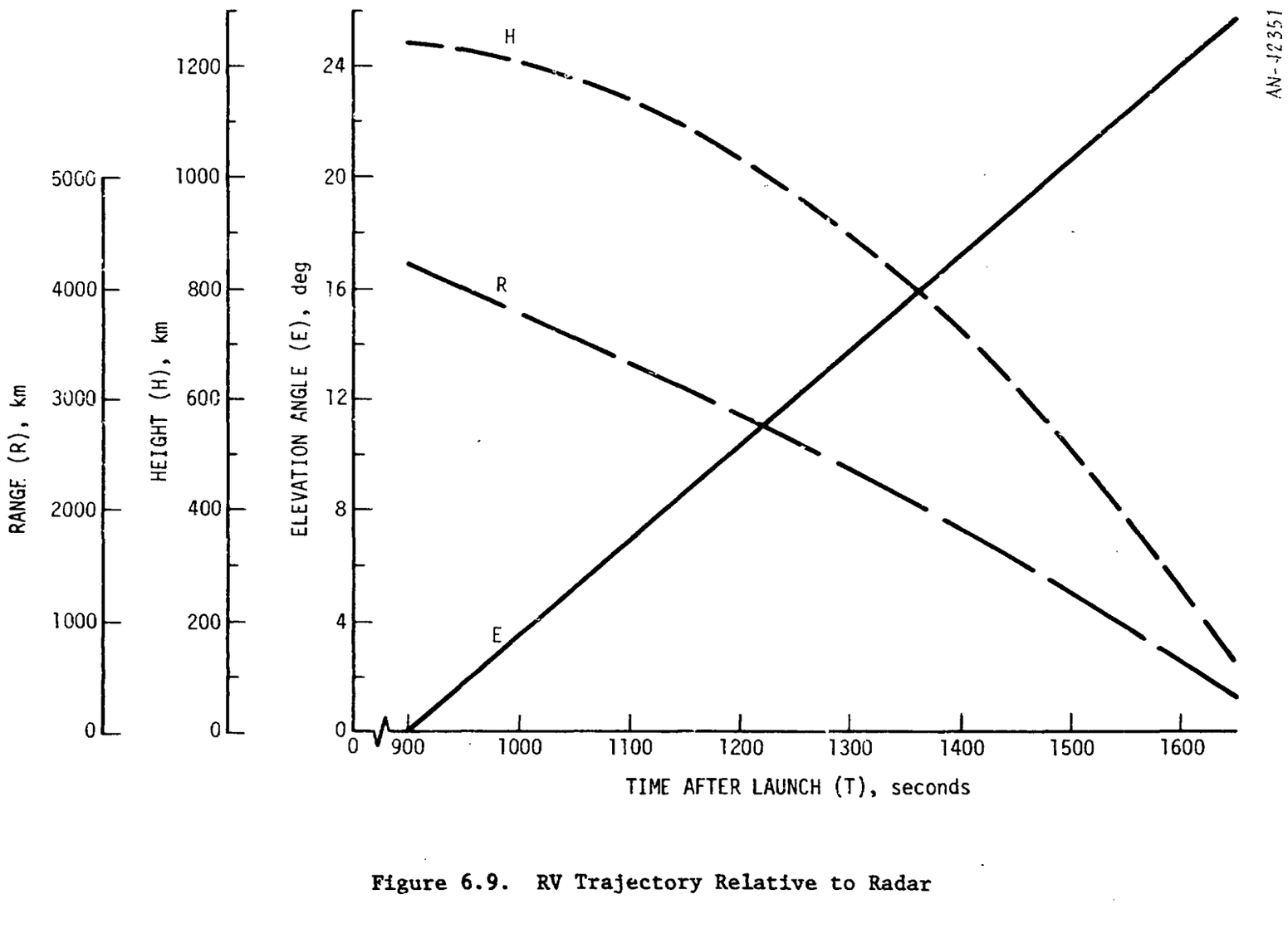

Figure 6.9. RV Trajectory Relative to Radar

The radar used in the baseline calculations was assumed to operate at 150 MHz, the frequency at which the measured scintillation data were obtained. As a practical matter, radars used to track targets in space typically operate at somewhat higher frequencies, often in the UHF band, but the parameters of the assumed radar are representative of this type of radar except for frequency. These parameters are given in Table 6.1.

This radar has a detection range (in vacuum) on a 1-square meter target of $R_1 = 7{,}900$ km . Its effective measurement error sigmas (see Sec. 6.3.1) are:

- Range: $A_R = 12$ m , $B_R = 150$ m
- Angle: $A_\theta = 0.6$ mrad , $B_\theta = 15.0$ mrad

TABLE 6.1

RADAR PARAMETERS

Frequency	f	150 MHz
Wavelength	λ	2 m
Peak Power	P_o	5 MW
Average Power	$\overline{P}$	250 kW
Pulse Length	τ	200 μs
Pulse Compression Ratio	F_{pc}	200
Effective Range Resolution	δR	300 m
Antenna Beam Width	$\delta\theta$	1.4 deg
Antenna Gain	G	44 dB
Detection Threshold	$(S/N)_o$	10 dB
System Noise Temperature	T_N	600K
System Losses	L	6 dB
Horizon Limit	E_o	2 deg

A heated patch (striated region) with typical dimensions was placed at the appropriate altitude in two different positions relative to the radar and target trajectory. These two cases, shown in Fig. 6.10, illustrate the two extreme conditions for artificially induced scintillations placed to interfere with radar tracking of a specific trajectory by a specific radar; they are:

- Case 1, Scintillations First. The patch is placed so as to obscure the beginning of track (at $E = E_o$), but the last portion of track will be in the clear.
- Case 2, Scintillations Last. The patch is placed so as to obscure the end of track, but the first portion will be in the clear.

In each case, the times (in seconds relative to launch time) at which scintillations would begin and end for the given trajectory and radar location were precomputed and used as entries in the simulation program.

In all calculations the tracking rate was held constant at 1 pulse per second, and the correlation time for the striations was quasi-arbitrarily set at 5 seconds.

Four different values of the relative scale size r_o/λ were used: $r_o/\lambda = 200, 100, 50, 25$. Since this is the only place where the radar wavelength actually enters the calculations, this parameterization has the effect of removing any significance from the fact that the baseline radar happened to be given an operating frequency of 150 MHz. This range of values of r_o/λ spans the region of practical interest. For $r_o/\lambda > 200$ (high frequency or large striations) the effect on radar tracking is, as we shall see, quite negligible. And $r_o/\lambda < 25$ (low frequency or small striations) will practically never be observed, given the distribution of striation scale sizes shown in Fig. 4.3. It should be noted that this entire range of relative scale sizes satisfies the far-field condition for a heated region at 300 km altitude.

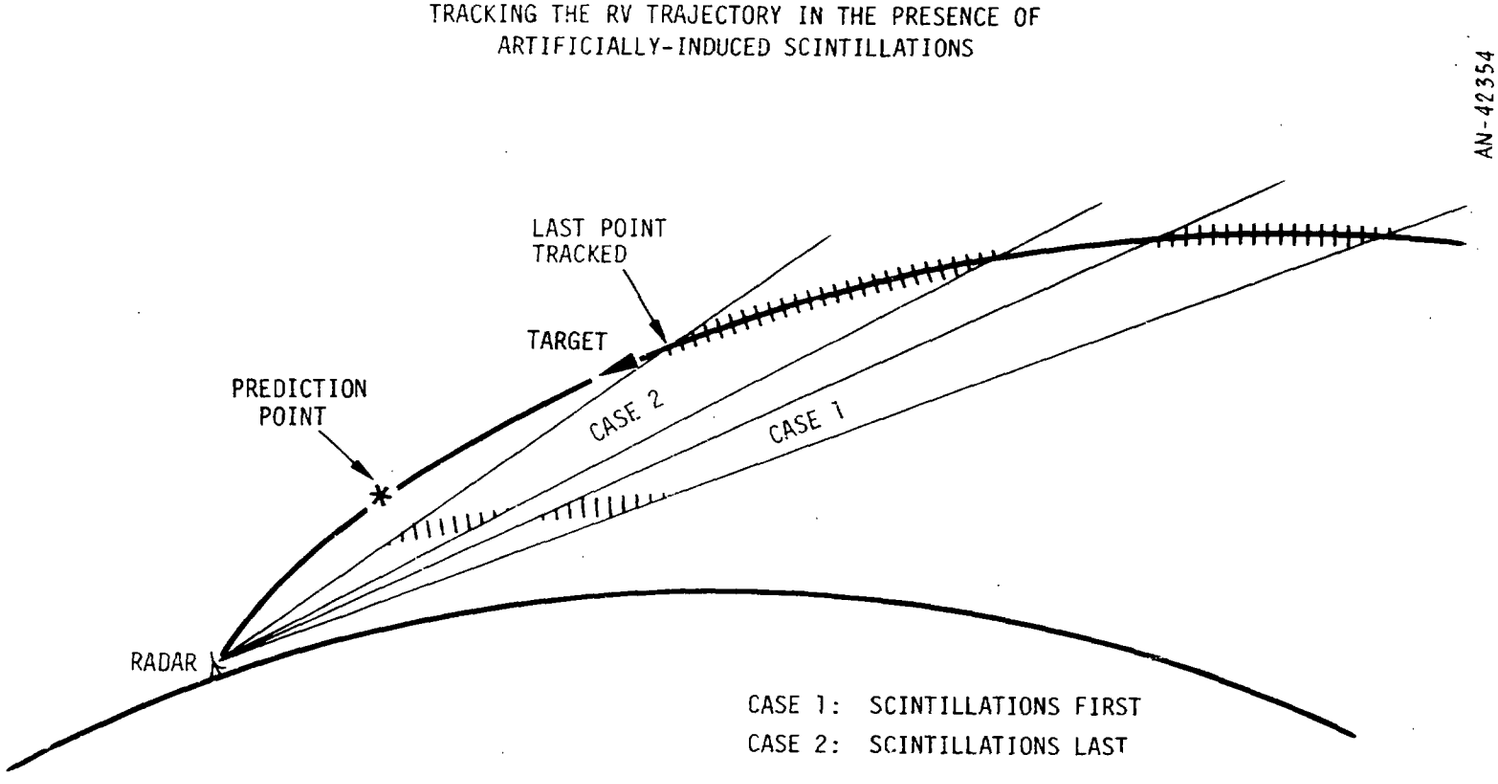

Figure 6.10. Tracking the RV Trajectory in the Presence of Artificially Induced Scintillations

To get an idea of the magnitudes of the angle scintillation errors, we have computed σ_o from Eq. 6.18 as a function of S_2 for the four selected values of relative scale size. These are shown plotted in Fig. 6.11. For comparison we have plotted on the same figure some values for the standard deviation of the natural ("vacuum") radar measurement angle error, σ_A from Eq. 6.14, for several values of S/N , using the parameters of the baseline radar. Among other things, this figure illustrates why the effects of angular scintillations with $r_o/\lambda > 200$ are so negligible.

In the baseline calculation, tracking was carried out at one pulse per second from T = 960 seconds (E = 2 degrees) to T = 1245 seconds (E = 11.8 degrees). This last track time was selected so that the trajectory could be projected ahead 300 seconds (untracked) to a point at about 400 km altitude. The results, when stated in the relative form to be described below, should be insensitive to the specific value of the last track time (projection time was one of the parameters which were later varied).

A pre-computation showed that the mean miss distance varied with the angle-error direction μ in a uniform manner over a factor of 2 as μ went from 0 to 90 degrees, with μ = 45 degrees representing the midway position. Accordingly, the baseline calculations were performed with μ = 45 degrees . This parameter was later varied.

All calculations were performed for values of the scintillation index on the range $0 \leq S_2 \leq 0.50$.

The minimum number of iterations necessary to provide consistent results was determined by pre-computation to be 80. All track simulations were iterated 80 times, and the mean prediction error $\bar{D}$ and its standard deviation σ_D were calculated for each run.

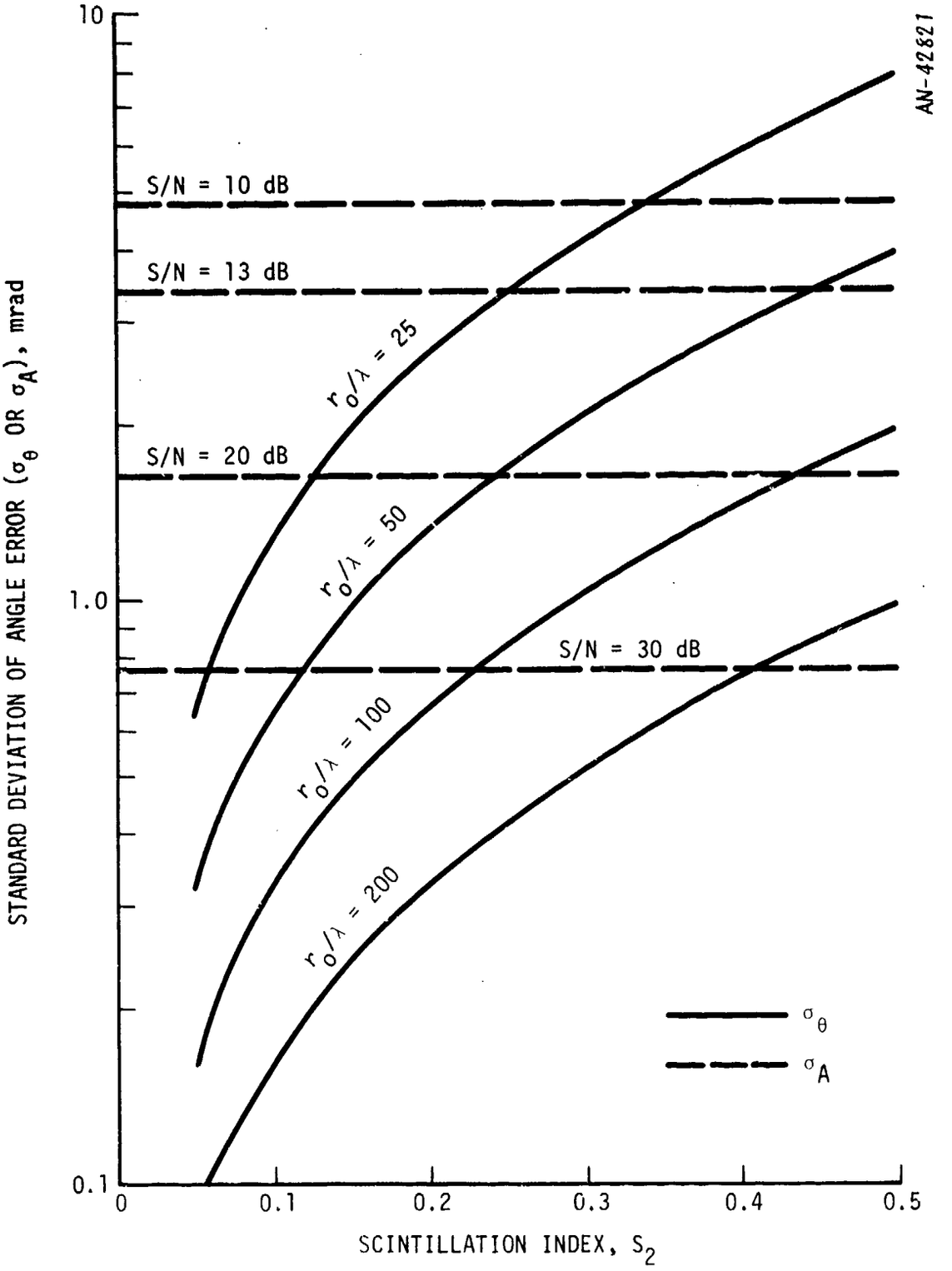

Figure 6.11. Angle Error Sigmas Due to Scintillations and Radar Measurement Errors

All results were normalized to the value of the mean prediction error, $\bar{D}_o$, for vacuum conditions (no scintillations). The relative mean prediction error $\bar{D}/\bar{D}_o$ is used to show the basic qualitative trends and approximate quantitative effects due to variation of the significant parameters. In this relative form the results should be insensitive to those elements of the specific scenario which do not directly affect the variation of $\bar{D}$ as a function of S_2 . Insofar as we were able to determine, only the location of the heated patch in relation to the beginning and end of track has a significant effect on this function, and this "parameter" was spanned by using Cases 1 and 2 separately in all calculations.

6.3.5 Results and Parameter Variations

The results of the baseline calculations for Cases 1 and 2 are shown in Figs. 6.12 and 6.13, as functions of scintillation index and relative scale size. Notice that there is practically no effect for $r_o/\lambda = 200$.

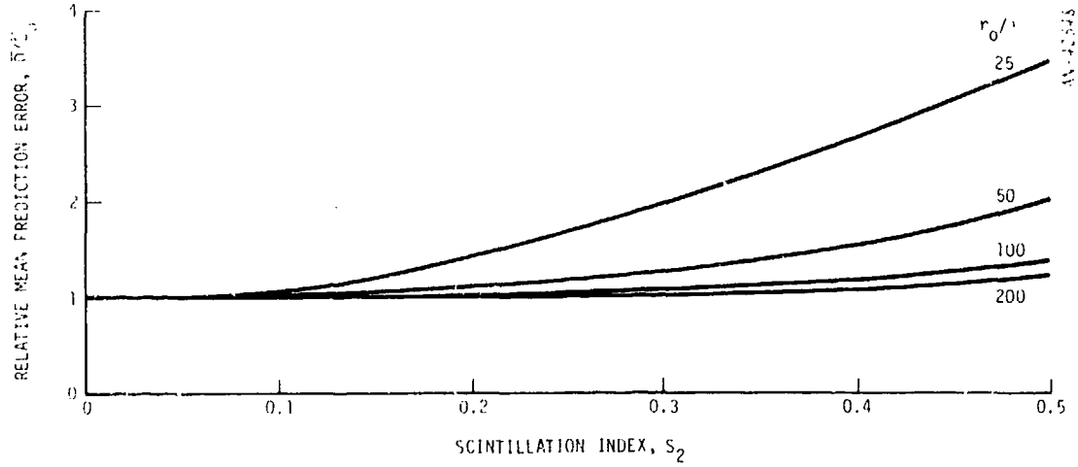

Figure 6.12. Relative Mean Prediction Error as Function of Scintillation Index for Several Values of Scale Size Over Wavelength, Case 1: Scintillations First

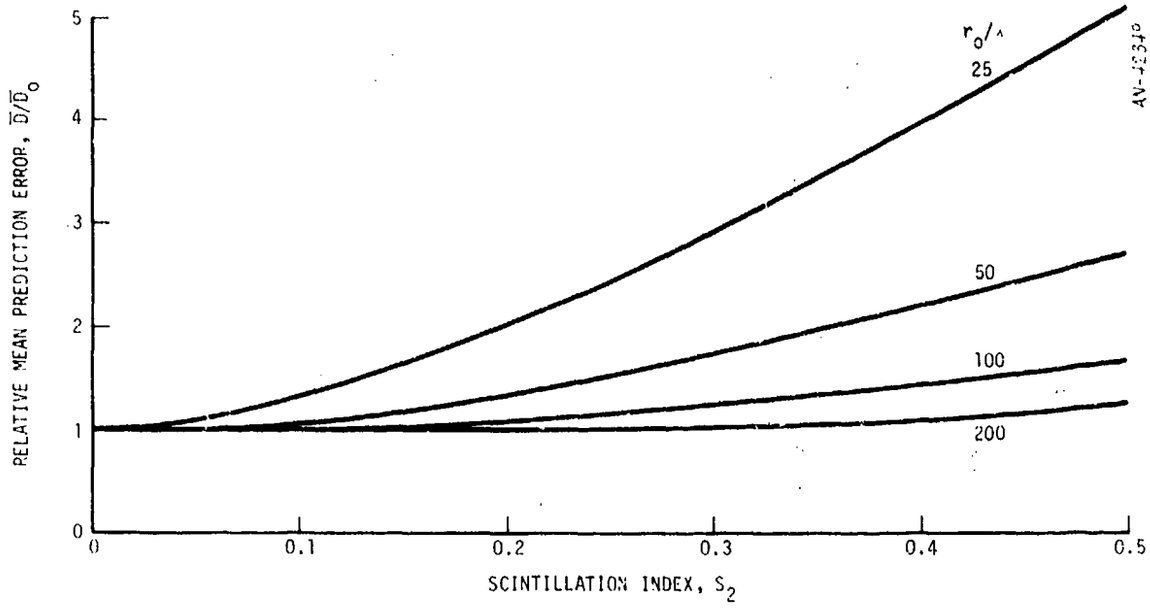

Figure 6.13. Relative Mean Prediction Error as Function of Scintillation Index for Several Values of Scale Size Over Wavelength, Case 2: Scintillations Last

---

In general, $\bar{D}/\bar{D}_o$ increased with S_2, the effect being negligible for $r_o/\lambda = 200$ and growing more significant as r_o/λ decreased. Case 2 (scintillations last) showed impressively greater increase in the relative mean prediction error with S_2 than was found for Case 1 (scintillation first). This should be expected, since in Case 1 the tracking filter has an opportunity to recover from the errors induced by the scintillations before making its projection, whereas in Case 2 it has no such opportunity.

As a matter of interest, the value of $\bar{D}_o$ for the baseline cases was approximately 2 km.

It should be pointed out that all tracking error simulations, however they are performed, show quite a lot of scatter. Even in vacuum, the standard deviation of the prediction error is usually a significant fraction of the mean value. As an illustration of this effect, Fig. 6.14

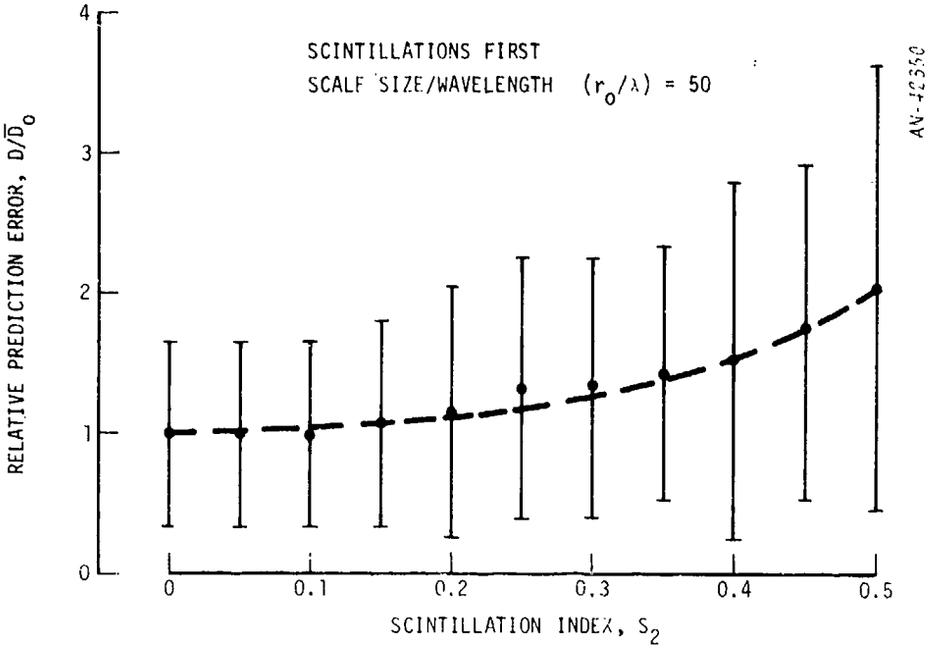

Figure 6.14. Relative Mean Prediction Error as Function of Scintillation Index

shows the one-sigma error bars on the relative prediction error for one particular pass through the tracking simulation. Note, however, that the basic trend is still clearly apparent. The reader should imagine error bars like these on all of the curves of $\bar{D}/\bar{D}_o$ plotted in this section; they were omitted only because they would have cluttered the figures into incomprehensibility.

As a separate calculation, the prediction time after track was varied over the range $1 \text{ s} \leq T \leq 400 \text{ s}$ for one particular set of the other basic parameters to ascertain the effect of this parameter on the baseline results. Although the calculation was only performed for this one case, the qualitative trend should apply to all of the baseline results, and there is no reason to suppose that the relative quantitative values should be much different for other cases. Figure 6.15 shows the mean prediction error, relative to the baseline value for $T = 300$ seconds as a function of projection time. It is quite obvious that the mean error varies linearly with the projection time.

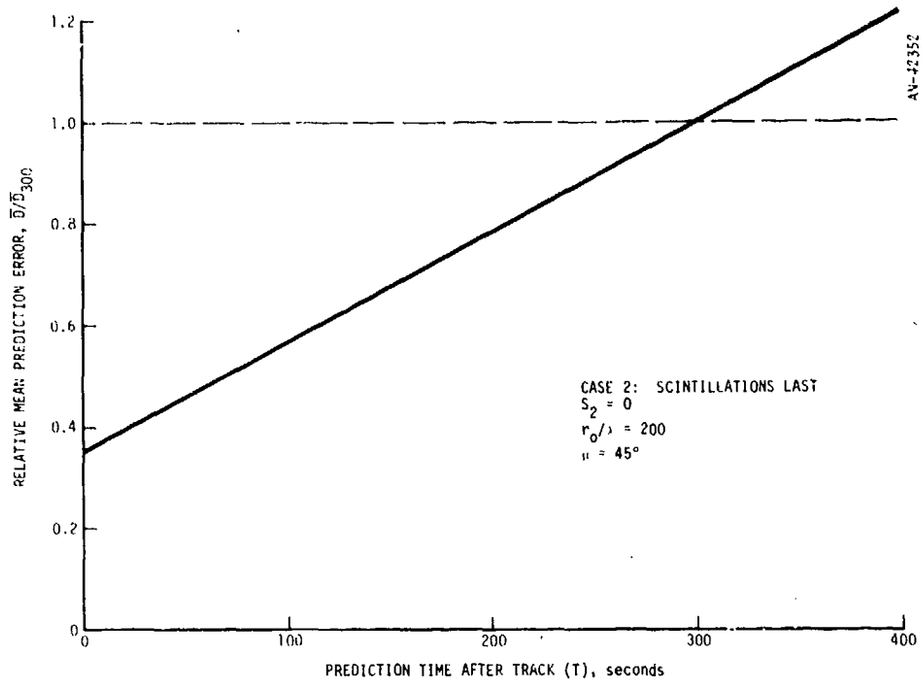

Figure 6.15. Relative Mean Prediction Error as Function of Prediction Time After Track

---

In another separate calculation, the angle-error direction μ was varied over the range $0° \leq \mu \leq 90°$ for one particular set of the other basic parameters to examine the effect of this parameter on the baseline results. In "real life," the parameter μ is determined by the direction of a vector transverse to the magnetic-field lines in the heated patch, projected onto the plane normal to the radar line-of-sight. Figure 6.16 shows the mean prediction error, relative to the baseline value for $\mu = 45$ degrees , as a function of angle μ . The effect of this geometrical factor is readily apparent.

Finally, we must take note of the fact that the radar parameters might be quite different than those given in Table 6.1, or the target cross section might be different from the value $\sigma = 0.4\ m^2$ used in the baseline calculation, either because the target itself is different or because the same target is being observed at a different radar frequency. Many of the radar parameters appear lumped into the constant R_1 which

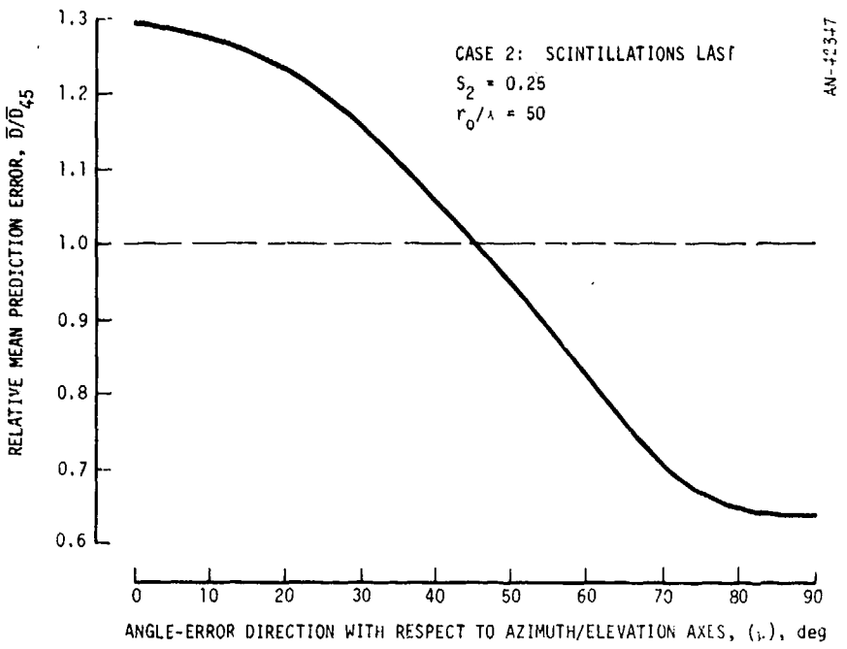

Figure 6.16. Relative Mean Prediction Error as Function of Angle Error Direction

---

is used in the condensed form of the radar equation given in Eq. 6.12. Using $\sigma_1 \equiv 1\ m^2$, we can rewrite that equation in the form

$$S/N = KR^{-4} \tag{6.17}$$

where

$$K \equiv (S/N)_1 R_1^4 \frac{\sigma}{\sigma_1} \tag{6.18}$$

Now, by varying K over an appropriate range of values we can account for variations in the target cross section and/or many of the radar parameters.

Accordingly, in another separate calculation K was varied over the range $10^{15}\ km^4 \leq K \leq 10^{18}\ km^4$ for one particular set of the other basic parameters. (The baseline value of K is $K_o = 1.56 \times 10^{16}\ km^4$.)

The effect on the baseline results of varying this lumped parameter is shown in Fig. 6.17, where we have plotted the relative mean prediction error, normalized to its value for $K = K_o$, as a function of K. Note that the curve becomes effectively flat for $K \geq 5 \times 10^{17}$, which is a good reason why there is no point in extending the calculation beyond $K = 10^{18}$. The reason for this behavior is easy to find: for the powerful radars or strong targets represented by these large values of K, the radar measurement error sigmas (which are the primary beneficiaries of the increased signal-to-noise ratio) are approaching their limiting values for $S/N >> 1$. In the other direction, the dashed portion of the curve for $K < 2 \times 10^{15}$ indicates the region where the returns are so weak that for at least part of the tracking range they failed to cross the receiver threshold. If the figure were extended much below $K = 10^{15}$ it would be found that few or no successful track pulses would be received during the time interval over which we are trying to track, so that the prediction error rapidly approaches infinity.

It is obvious that the radar tracking error is more serious when the heated region obscures the terminal portions of the track than when it occurs toward the beginning. In principle, significant increases in prediction error can occur for such "scintillations last" cases even when the scintillation index is only moderately severe ($0.2 \lesssim S_2 \leq 0.3$). In practice, however, geographical considerations would generally make it difficult or impossible to place the striated patch close enough to the radar to ensure that no good track returns can be obtained after the scintillation interval, and without such placement the effect approaches a less critical "scintillations first" situation.

Since the angle μ is not usually subject to control, the results illustrated by Fig. 6.16 are of primarily theoretical interest.

The radar power vis-a-vis target cross section, on the other hand, can clearly be of great significance in evaluating the effects of

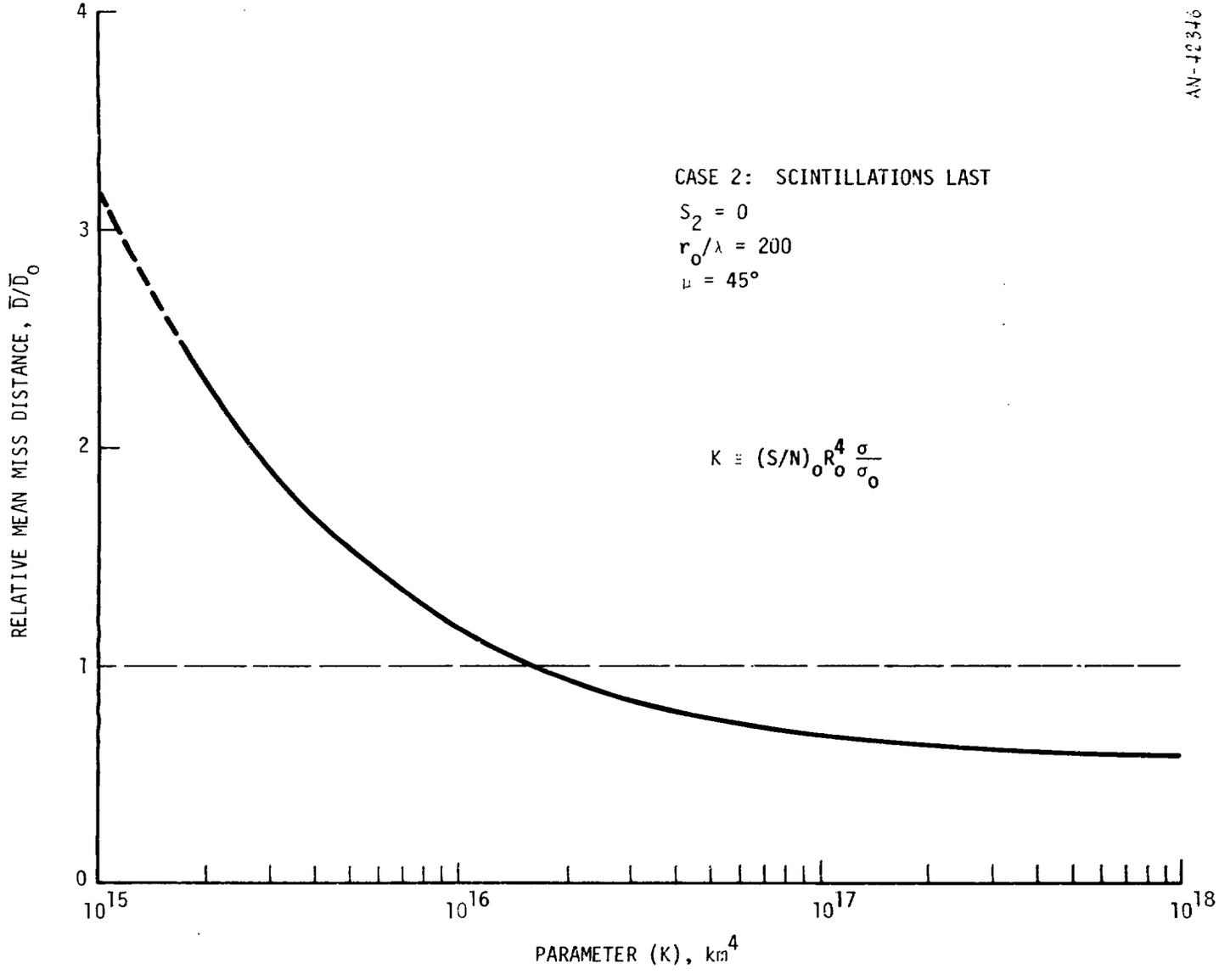

Figure 6.17. Relative Mean Prediction Error as a Function of Radar Parameter K

scintillations on track performance. We have seen that it is of diminishing usefulness to increase the power beyond a certain point, but that tracking can be seriously degraded by the heated patch if the radar is marginal in power to begin with.

7 SATELLITE COMMUNICATION SYSTEMS

The basic elements of a satellite communication system consist of a ground terminal transmitter, a satellite-borne repeater, and a ground terminal receiver. One or both of the "ground" terminals may in fact be in an aircraft, but the principle is the same. The satellite equipment usually provides only the functions of frequency translation and amplification; signal processing and demodulation generally occur only at the ground terminals.

The uplink and downlink each provide a one-way path which might intersect a heated patch and suffer some degradation. It is geometrically unlikely, though not impossible, that both links should be affected by a single patch. In this section we will compute the degradation for a single one-way link; extension to account for striation effects on both links is obvious.

Each link is usually required to handle multiple simultaneous communication channels. Some types of channels handle voice messages, others deal with digital information. The common method used by satellite systems for multi-channel voice communications is frequency division multiplex frequency modulation (FDM-FM). To transmit digital information over satellite communication links there are basically two commonly used modulation methods: frequency-shift-keying (FSK) and phase-shift-keying (PSK). Each of these in turn may be classified according to the method of detection used. For FSK the detection may be coherent (CFSK) or non-coherent (NFSK). For PSK, one may again find coherent detection (CPSK) or non-coherent detection used, though in the latter case what is usually employed is the co-called differentially coherent system (DPSK). For details concerning the theory and operation of these (as well as other) systems, a textbook on communication theory should be consulted (see for example Schwartz, Bennett, and Stein[27]).

The source of system degradation which we shall consider here is the "signal fading" caused by relative motion of the satellite and the striations which lie across the propagation path. Even in the absence of artificially induced striations, satellite communication links are subject to natural fading, and they are designed with the capacity to perform adequately under given expected levels of fading. Depending on geographical location and local time-of-day, natural fading of 1 to 10 seconds duration and a depth of 4 to 6 dB occurs quite frequently, with longer and/or much deeper fading occurring correspondingly less often. Paulson and Hopkins[28] report fading at 250 MHz of the order of 10 dB or greater peak-to-peak occurring 5 to 10 percent of the time--mainly at night--over a 3-year period at receiving sites located near the equator.

Some discussion of the fading phenomena associated with the artificially induced striations may be found in the appendix. There it is pointed out that with the Rice or Nakagami[29] distributions for signal amplitude almost any fading depth is possible with some small probability. However, the fading depth at any particular level of probability can be related to the scintillation index by comparing the amplitudes at two specified percentile levels of the distribution function. This was done for the Nakagami distribution and index S_4 in Fig. A.2 of the appendix. Since it can be seen from Fig. A.1 how close the Nakagami distribution is to the Rice distribution on the one hand and to the approximation $S_4 = 2S_2$ on the other, Fig. A.2 can be interpreted in terms of index S_2, if desired, by dividing the given index in half. The meaning of these curves is that for a given value of the scintillation index the indicated fading depth (in dB) will be observed 5 percent of the time for the bottom curve, 1 percent of the time for the middle curve, or 0.1 percent of the time for the upper curve.

A perhaps more direct measure of system degradation may be found by considering the effect of the fading on a digital communication system. A digital information signal is composed of a sequence of symbols, and

each symbol is transmitted as a sequence of elements. The Probability of Element Error, P_e, is defined as the probability that the receiver assumes any element other than the one transmitted. In Chapter 7 of Schwartz, Bennett & Stein,[27] it is shown that P_e is a function only of the signal-to-noise ratio on the link, and expressions for these functions are derived in the cases of the four types of digital communication systems discussed above. For DPSK and NFSK systems the expressions are particularly simple:

$$\text{For DPSK:} \quad P_e = \frac{1}{2} \exp[-(S/N)] \tag{7.1}$$

$$\text{For NFSK:} \quad P_e = \frac{1}{2} \exp\left[-\frac{1}{2}(S/N)\right] \tag{7.2}$$

Suppose that the signal-to-noise ratio at a given instant would have been S/N_o in the absence of striations, but that because of fading it has the received value S/N. Using symbols previously introduced, we can write

$$(S/N)_o \equiv R_o^2/2 \tag{6.7}$$

and

$$(S/N) \equiv R^2/2 \tag{6.5}$$

The fading due to the striations has the amplitude distribution

$$p_1(R;R_o,\beta)$$

given in Eq. 6.1.

Accordingly, the probability of element error in the presence of fading can be computed by integrating:

$$P_e(R_o,\beta) = \int_0^\infty P_e(R)p_1(R;R_o,\beta)\,dR \tag{7.3}$$

For DPSK and NFSK systems this integral can be done analytically and the results expressed in simple closed form. We find that

$$\text{For DPSK:}\quad P_e = \frac{1}{2}\frac{1+\beta}{1+\beta+\gamma_o}\exp\left[-\frac{\beta\gamma_o}{1+\beta+\gamma_o}\right] \tag{7.4}$$

$$\text{For NFSK:}\quad P_e = \frac{1}{2}\frac{1+\beta}{1+\beta+\frac{1}{2}\gamma_o}\exp\left[-\frac{\beta\gamma_o/2}{1+\beta+\frac{1}{2}\gamma_o}\right] \tag{7.5}$$

where $\gamma_o \equiv (S/N)_o$

Notice that these two expressions are identical except for a factor of 2 in signal-to-noise ratio.

Since the DPSK method is extremely common in use, let us now focus onto Eq. 7.4. In Fig. 7.1 we show P_e as a function of scintillation index S_2 for selected values of the "vacuum" signal-to-noise ratio γ_o, and in Fig. 7.2 we show P_e as a function of γ for selected values of S_2. Finally, we can calculate a link degradation loss factor which sums up the entire situation in the following manner. For many practical communication systems, a value of $P_e = 10^{-5}$ is barely acceptable; anything larger than this produces undesirably high error rates. Consider the "vacuum" case, $S_2 = 0$: Fig. 7.2 tells us that in order to assure $P_e \leq 10^{-5}$ it is necessary that $\gamma_o \geq 10.3$ dB. Still using this figure, let us find the required value of γ_o to produce $P_e = 10^{-5}$ for each

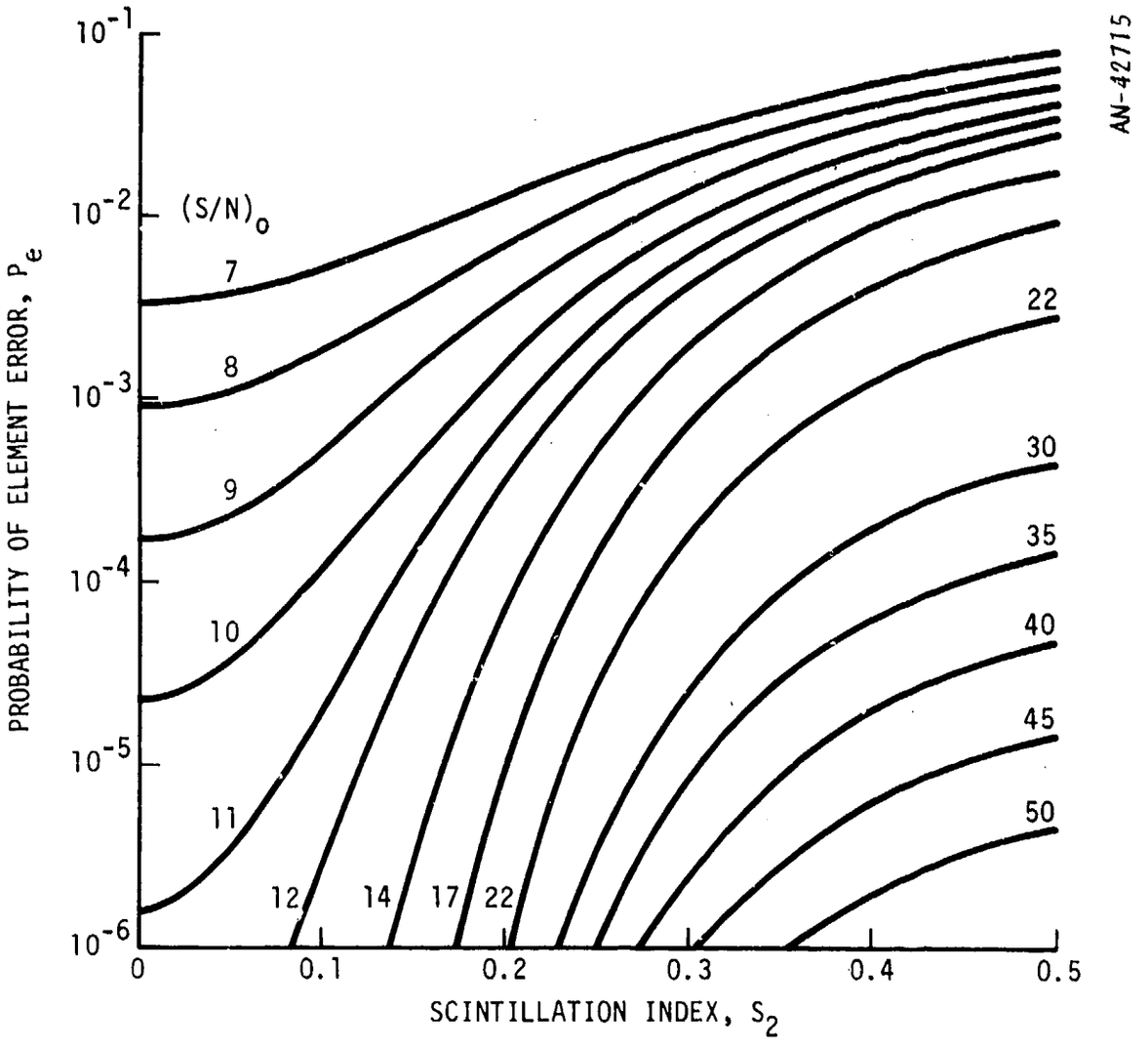

Figure 7.1. Probability of Element Error on One Link of a Binary DPSK Communication System

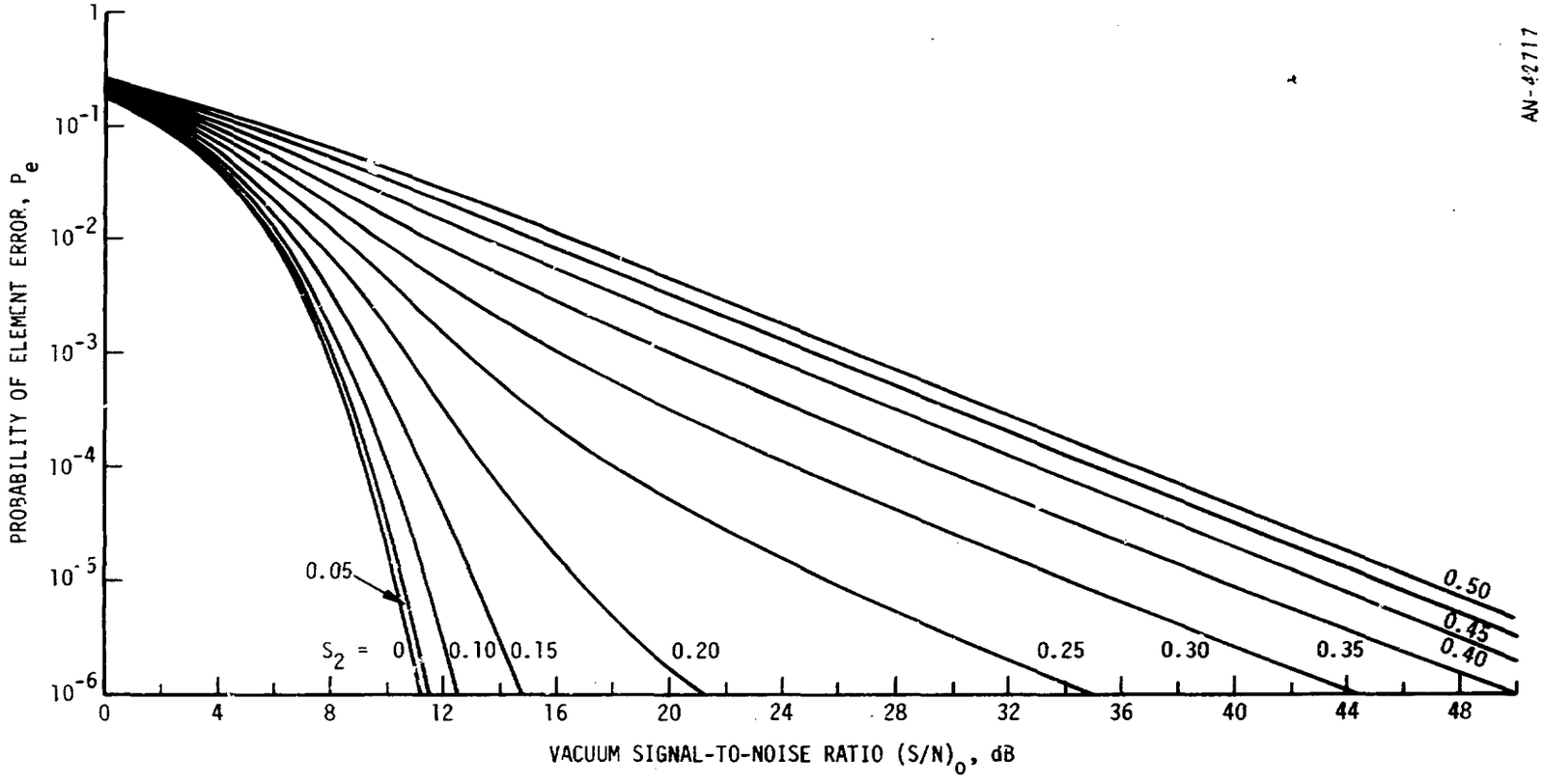

Figure 7.2. Probability of Element Error on One Link of a Binary DPSK Communication System

other value of S_2 ; the difference between this γ_o and 10.3 dB represents the additional "vacuum" signal-to-noise ratio necessary in order to overcome the effects of fading at that particular level of scintillation. This we shall call the link degradation loss factor L , which is plotted as a function of S_2 in Fig. 7.3.

Notice the appearance of a threshold effect in this figure, represented by the very steep rise in the curve beyond a certain point. If we arbitrarily set 10 or 15 dB as the maximum acceptable loss factor (the exact value is not very critical), it is clear that for S_2 less than about 0.25 the system can operate, but for $S_2 > 0.25$ it will be in considerable difficulty.

These calculations were made, of course, only for two of the many different kinds of communication systems, but the results may be considered as typical of the effects to be expected. We see that fading due to scintillations causes an increase in the probability of element error which may reach unacceptable levels if the link signal-to-noise ratio is too small and/or the scintillation index is too large. Because the natural environment is also subject to slow fading whose magnitudes may, with appropriately small probabilities, cause undesired increases in P_e , satellite communication systems are usually designed to have a sufficiently large $(S/N)_o$ to assure satisfactory performance under normal fading of given probabilities of occurrence. Figure 7.3 suggests that such conservatively designed communication systems may be expected to survive artificial scintillations with indices up to approximately $S_2 \simeq 0.25$, but it is unlikely that a nominal system will have been designed to endure link degradation losses in excess of 25 dB, such as will be encountered when $S_2 > 0.3$. Accordingly, we can say that scintillations with such high indices will have considerable disruptive effects on normal communication systems. It should be remarked, however, that artificial scintillations rarely attain these high values of S_2 .

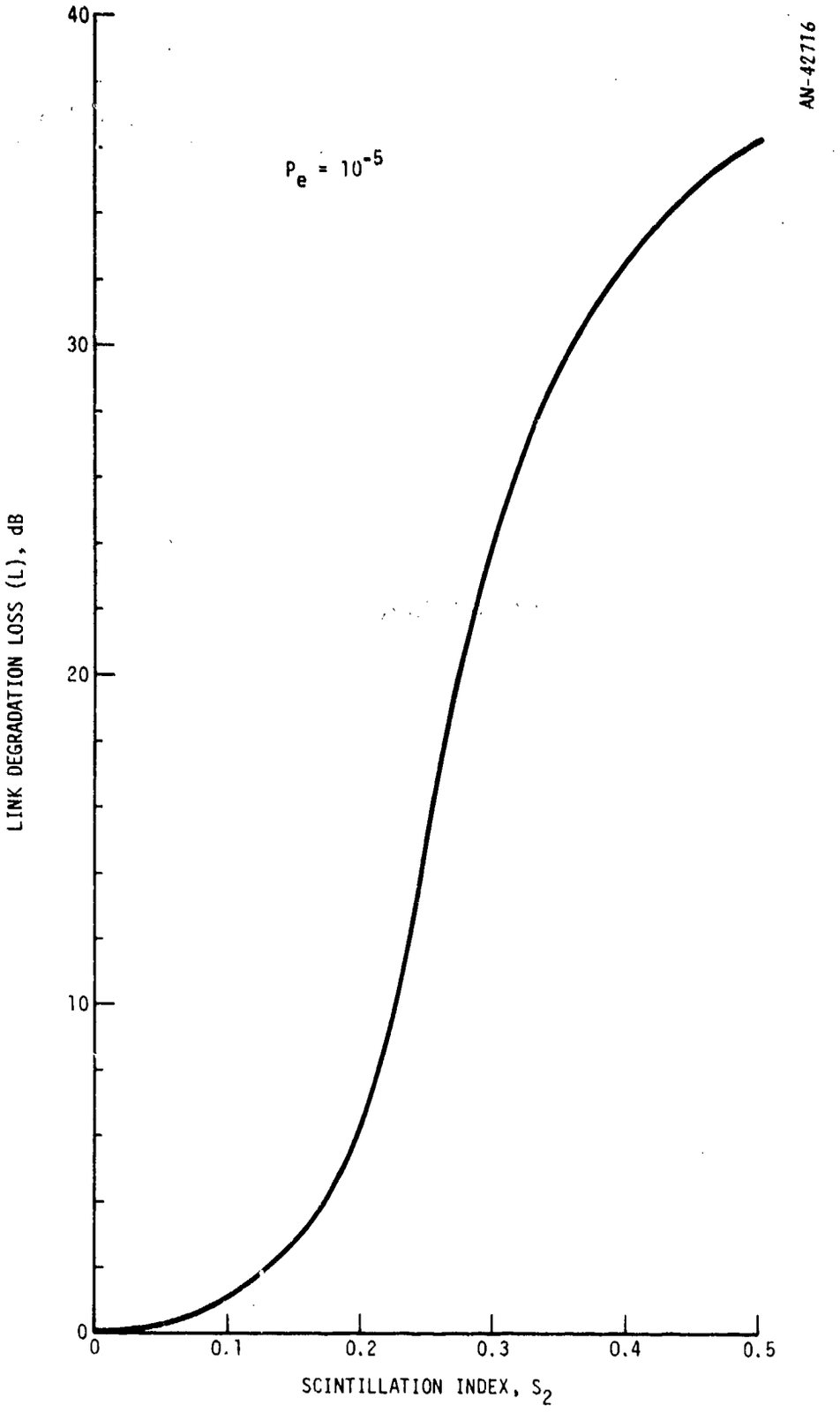

Figure 7.3. Degradation of Binary DPSK Communication Link as Function of Scintillation Index S_2

APPENDIX

SCINTILLATION INDEXES AND STATISTICAL DISTRIBUTIONS

Several quantitative measures for the scintillation depth of signals from radio stars and satellites are in common use. In this appendix we describe the most common indexes and illustrate some of the interrelations among them for some models of the scintillation statistics.

In measurements of satellite signals the amplitude $R = (AA^*)^{1/2}$ is frequently measured, while in radio star measurements the power, or a quantity proportional to R^2, is commonly measured. Briggs and Parkin have defined four scintillation indexes based on the mean or root-mean-square deviations of R or R^2. These are:

$$S_1 = \frac{E[|R - E(R)|]}{E(R)}$$

$$S_2 = \frac{\left\{E(R^2) - [E(R)]^2\right\}^{1/2}}{E(R)}$$

$$S_3 = \frac{E(|R^2 - [E(R)]^2|)}{E(R^2)}$$

$$S_4 = \frac{\left\{E(R^4) - [E(R^2)]^2\right\}^{1/2}}{E(R^2)}$$

The scintillation index measured and reported by Bowhill and others at Aeronomy Corporation is S_2 (at least in PRAIRIE SMOKE II-V). Here S_4 is equivalent to the measure S used throughout the Briggs and Parkin paper[2] and is equal to the square root of the variance of R^2 considered by Mercier.[11]

Given the probability distribution of R, it is possible to find relations among S_1, S_2, S_3, and S_4. However, the exact distribution of R is not generally known. Mercier asserts that far from a random phase screen, R assumes a Rice distribution with density function

$$\frac{R}{\Psi} \exp\left[-(R^2 + P^2)/2\Psi\right] I_o(RP/\Psi)$$

in Rice's original notation, where I_o is the modified Bessel function of zero order. The parameter Ψ is proportional to the amount of power in the signal fluctuation; $P^2/2\Psi$ is a kind of "signal-to-noise" ratio exactly analogous to random thermal in-phase and quadrature noise added to a signal of known amplitude. For very large Ψ, the fluctuations are large and the distribution approaches Rayleigh; for small Ψ, the fluctuations are small and the distribution approaches a shifted Gaussian. Over the range of values of the parameter Ψ, the scintillation index S_2 as a function of S_4 varies, but is usually about 0.5. (The ratio is about 0.52 in the Rayleigh limit.)

An alternative distribution is the Nakagami m-distribution[29] whose density function is given by

$$\frac{2m^m}{\Gamma(m)\Omega^m} R^{2m-1} \exp(-mR^2/\Omega)$$

where $\Omega = E(R^2)$. This distribution approximates the amplitude of the vector sum of many waves with random amplitudes and phases. For large m the distribution approximates the Rice distribution, while for $m = 1$ it becomes exactly Rayleigh. The index $S_4 = m^{-1/2}$; the expression for S_2 is moderately complex, but $S_2 \simeq 0.5S_4$ as before.

Figure A.1 shows S_4 as a function of S_2 for several assumed distributions of R : Gaussian, Rayleigh, Rice, and Nakagami. Except

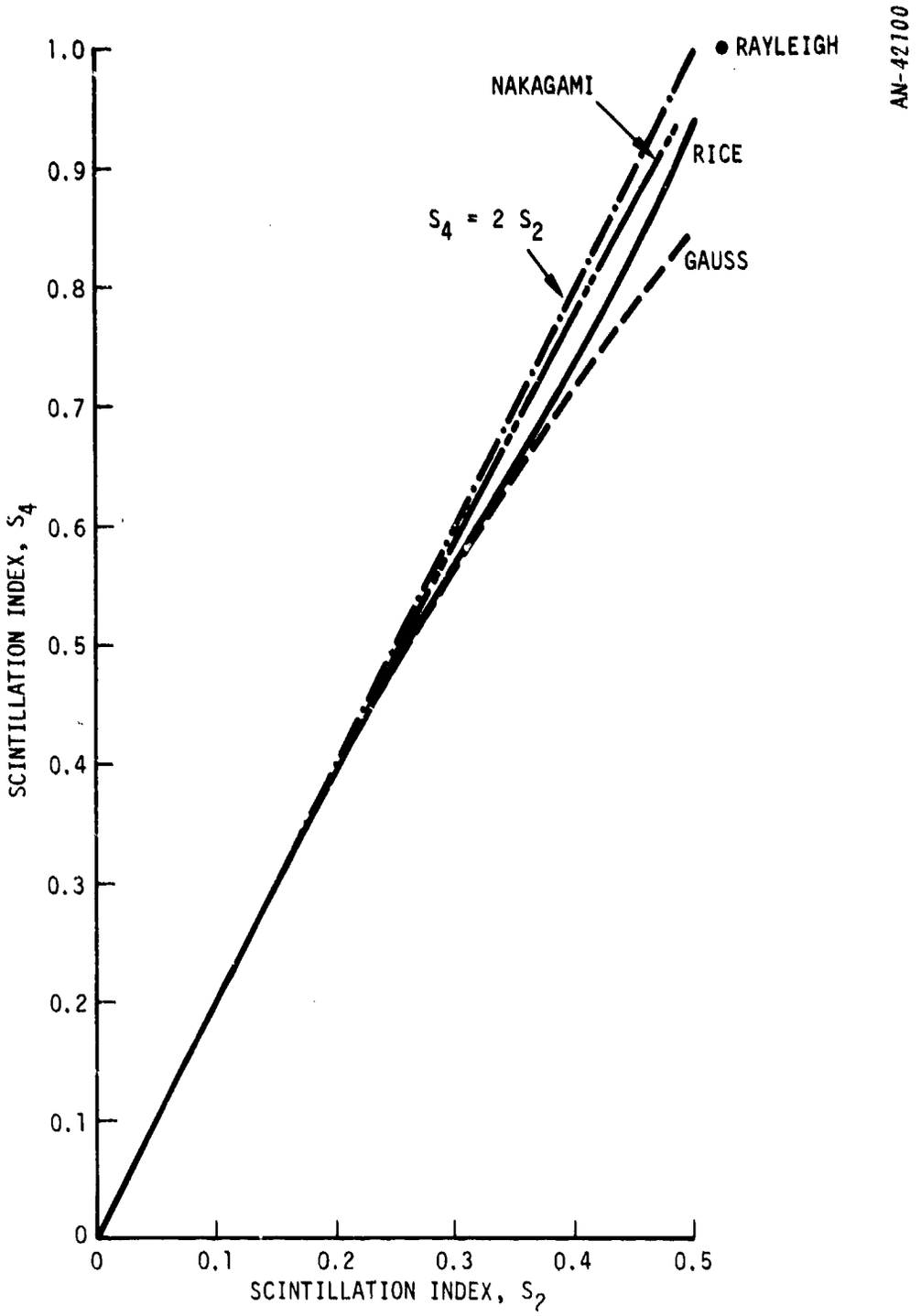

Figure A.1. Scintillation Index S_4 as a Function of S_2 for Several Assumed Distributions of Amplitude

in the case of the Rayleigh distribution, which reduces to a single point on this figure, all of these distributions produce curves which are substantially similar to $S_4 = 2S_2$ over the range of meaningful values of these parameters.

There is considerable uncertainty as to which distribution best fits the measured data from natural scintillation. Nakagami[29] showed good agreement of the m-distribution to long-range HF (9.67 to 20.02 MHz) communication channels. Whitney, et al.[30] showed fair agreement between the Nakagami distribution and the distribution of fading of ATS-3 signals at 136 MHz. On the other hand, Rino and Fremouw[24] showed that the Nakagami distribution yields only a poor approximation to ATS-3 fading distribution measured in Peru. They indicate good agreement to a more complicated two-dimensional Gaussian (or Hoyt) distribution for which the in-phase and quadrature scattered components have a joint elliptical one-sigma contour. (The Rice distribution is a special case for which that ellipse is a circle.) This distribution can yield values of $S_4 > 1$.

The apparent inconsistency between these two views seems to stem from different sets of measurements. Whitney used ATS-3 fading data measured in Massachusetts, Greenland, and Peru. The best fit to Nakagami statistics was observed in the Massachusetts data for which the fading was less severe than observed in Greenland and Peru. Rino and Fremouw used ATS-3 data from Peru only, with stronger fading. The Gaussian model approaches the Rice or Nakagami for the case of shallow fading. Consequently, the apparent inconsistency seems to stem from the different range of data. We should note, however, from the results of Rino and Fremouw that the Nakagami statistics provides a poor fit for deep fading.

While the S-indices and the m-index can be computed readily from digitized samples of the signal amplitude or power, signal levels are frequently recorded only on paper charts so that these exact indexes are difficult to determine. Some approximate indexes which are easy to determine from these charts are in common usage. One form is to compute

$(R_2 - R_1)/(R_2 + R_1)$, where R_2 and R_1 are signal levels picked from the chart in some way. For example, R_2 and R_1 can be the maximum and minimum signal levels over the interval; another frequent selection is the "third peak down" from the maximum and "third peak up" from the minimum. Bischoff and Chytil[31] illustrate the relations between two approximate scintillation indexes and the m-index.

The logarithm of the signal is frequently recorded, especially in conjunction with communication satellites, so that the fading can be expressed in dB. The dB level of scintillations is commonly the difference in dB between selected peak and null signal levels during a recording interval. With the Rice or Nakagami distributions for signal amplitude, almost any fading depth is possible with some small probability. However, one can relate S_4 (or m) to the fading depth by comparing the amplitudes at two specified percentile levels of the distribution function. Figure A.2 shows the range in dB between R_{95} and R_{05}, R_{99} and R_{01} , and $R_{99.9}$ and $R_{0.1}$ where the subscript denotes the percentile values for the Nakagami distribution of amplitude.

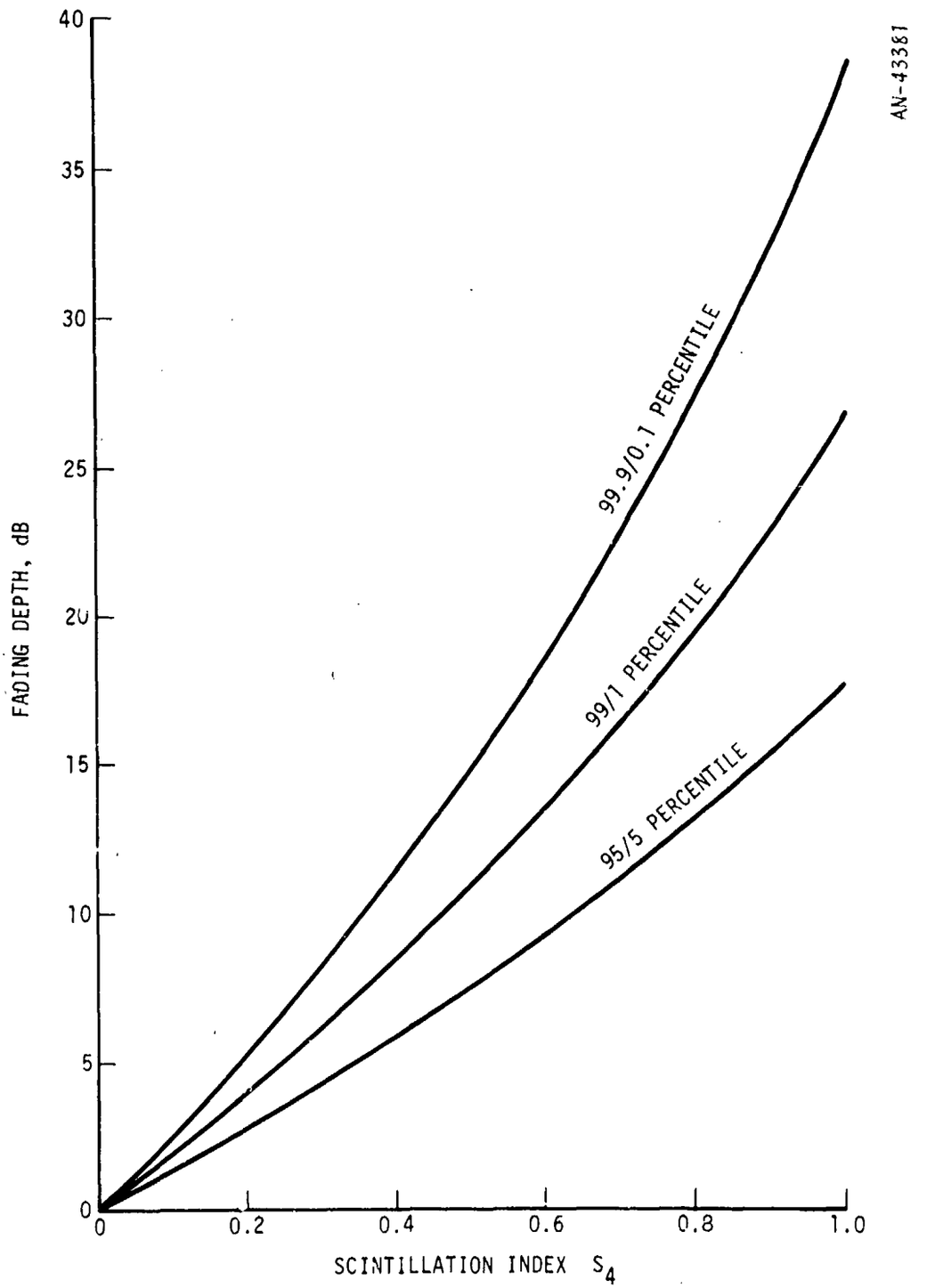

Figure A.2. Fading Depth in dB.

REFERENCES

1. W.F. Utlaut, "Radio-Wave Modification of the Ionosphere," Journal of Geophysical Research, Vol. 75, No. 31, November 1, 1970, pp. 6402-6405.

2. B.H. Briggs and I.A. Parkin, "On the Variation of Radio Star and Satellite Scintillations with Zenith Angle," Journal of Atmospheric and Terrestrial Physics, Vol. 25, pp. 339-365, 1963.

3. G. Meltz and R.E. LeLevier, "Heating the F Region by Deviative Absorption of Radio Waves," Journal of Geophysical Research, Vol. 75, No. 31, November 1, 1970, pp. 6406-6416.

4. W.F. Utlaut, E.J. Violette, and A.K. Paul, "Some Ionosonde Observations of Ionosphere Modification by Very High Power, High Frequency Ground-Based Transmission," Journal of Geophysical Research, Vol. 75, No. 31, November 1, 1970, pp. 6429-6435.

5. A.A. Biondi, D.P. Sipler, and R.D. Hake, Jr., "Optical (λ6300) Detection of Radio Frequency Heating of Electrons in the F Region," Journal of Geophysical Research, Vol. 75, No. 31, November 1, 1970, pp. 6241-6424.

6. W.F.J. Evans, E.J. Llewellyn, J.C. Haslett, and L.R. Megill, "Preliminary Results from the 1.27-Micron Measurements in the Boulder Ionospheric Modification Experiment," Journal of Geophysical Research, Vol. 75, No. 31, November 1, 1970, pp. 6425-6428.

7. H.G. Booker, J.A. Ratcliffe, and D.H. Shinn, "Diffraction from an Irregular Screen with Applications to Ionospheric Problems," Transactions of the Royal Society, Vol. 242, 1950, pp. 579-607.

8. A. Hewish, "The Diffraction of Radio Waves in Passing Through a Phase-Changing Ionosphere," Proc. Roy. Soc. (London) A, Vol. 209, October 8, 1951, pp. 81-96.

9. H.G. Booker, "The Use of Radio Stars to Study Irregular Refraction of Radio Waves in the Ionosphere," Proceedings of the IRE, January 1958, pp. 298-314.

10. S.A. Bowhill, "Statistics of a Radio Wave Diffracted by a Random Ionosphere," Journal of Research of the National Bureau of Standards--D. Radio Propagation, Vol. 65D, No. 3, May-June, 1961.

REFERENCES (Cont.)

11. R.P. Mercier, "Diffraction by a Screen Causing Large Random Phase Fluctuations," Proc. Camb. Phil. Soc., 58, pp. 382-400, 1962.

12. D.G. Singleton, "Saturation and Focusing Effects in Radio-Star and Satellite Scintillations," Journal of Atmospheric and Terrestrial Physics, 1970, Vol. 32, pp. 187-208.

13. E.J. Fremouw and C.L. Rino, "An Empirical Model for Average F-Layer Scintillation at VHF/UHF," Radio Science, Vol. 8, No. 3, pp. 213-222, March 1973.

14. H.D. Craft, Jr., and L.H. Westlund, "Scintillations at 4 and 6 GHz Caused by the Ionosphere," AIAA 10th Aerospace Sciences Meeting, San Diego, CA, January 17-19, 1972.

15. R.R. Taur, "Ionospheric Scintillation at 4 and 6 GHz," COMSAT Technical Review, Vol. 3, No. 1, Spring 1973, pp. 145-163.

16. S.A. Bowhill and E.E. Mendenhall, "Transmission Experiments in PRAIRIE SMOKE I," Proceedings of PRAIRIE SMOKE I RF Measurements Data Workshop, Stanford Research Institute, January 1972.

17. S.A. Bowhill, E.E. Mendenhall, and D.R. Ward, "Transmission Experiments in PRARIE SMOKE Ib and II," Proceedings of the PRAIRIE SMOKE II RF Measurements Data Workshop, Stanford Research Institute, June 1972.

18. S.A. Bowhill, E.E. Mendenhall, and D.R. Ward, "Transmission Experiments in PRAIRIE SMOKE III," Proceedings of the PRAIRIE SMOKE III RF Measurements Data Workshop, Stanford Research Institute, October 1972.

19. S.A. Bowhill and D.R. Ward, "Correlation Analysis of PRAIRIE SMOKE Transmission Results," Proceedings of the PRAIRIE SMOKE IV RF Measurements Data Workshop, Stanford Research Institute, March 1973.

20. S.A. Bowhill and D.R. Ward, "Geostationary Transmission Experiments in PRAIRIE SMOKE IV RF," Proceedings of the PRAIRIE SMOKE IV RF Measurements Data Workshop, Stanford Research Institute, March 1973.

21. E.K. Walton, D.R. Ward, J.L. Long, and S.A. Bowhill, "Orbital Experiments in PRAIRIE SMOKE V," Aeronomy Corporation, December 1973.

22. E.K. Walton, D.R. Ward, and S.A. Bowhill, "The Geostationary Yield Experiment," Aeronomy Corporation, December 1973.

REFERENCES (Concl.)

23. B.R. Pendyala and G.D. Thome, "A Model for 'On-Frequency' Field-Aligned Scattering," Proceedings of the PRAIRIE SMOKE Yield Model Workshop, Stanford Research Institute, July 1973.

24. C.L. Rino and E.J. Fremouw, "Statistics for Ionospherically Diffracted VHF/UHF Signals," Radio Science, Vol. 8, No. 3, March 1973, pp. 223-233.

25. R.W. Hendrick, "Propagation in a Striated Medium," presented at the DNA Striation-Propagation Meeting, 18 June 1974 (meeting SECRET, paper UNCLASSIFIED).

26. J.V. DiFranco and W.L. Rubin, Radar Detection, Prentice-Hall, 1968.

27. M. Schwartz, W.R. Bennett, S. Stein, Communication Systems and Techniques, McGraw-Hill, 1966.

28. M.R. Paulson and R.U.F. Hopkins, "Effects of Equatorial Scintillation Fading on SATCOM Signals," Naval Electronics Laboratory Center NELC/TR-1875, San Diego, CA, 8 May 1973.

29. M. Nakagami, "The m-Distribution--A General Formula of Intensity Distribution of Rapid Fading," in Statistical Methods of Radio Wave Propagation, W.C. Hoffman, ed., Pergamon Press, 1960.

30. H.E. Whitney, J. Aarons, R.S. Allen, and D.R. Seemann, "Estimation of the Cumulative Amplitude Probability Distribution Function of Ionospheric Scintillations," Radio Science, Vol. 7, No. 12, December 1972, pp. 1095-1104.

31. K. Bischoff and B. Chytil, "A Note on Scintillation Indices," Planet. Space Sci., Vol. 17, pp. 1059-1066 (1969).